Energetic ion losses in high-beta rippled tokamaks

Michinao Bunno

Abstract

The energetic ion losses in the rippled tokamaks are studied in this thesis. Since the orbits of the energetic ions depend on the magnetic field structure, the field component generated by the equilibrium plasma current also alters the energetic ion losses. These effects are called finite beta effects. The physical mechanism of the finite beta effects should be clarified especially in the high-beta rippled tokamaks.

This research can be separated by two parts: the magnetohydrodynamics (MHD) equilibrium calculation and the orbit calculation. Firstly, the MHD equilibrium should be calculated to clarify the finite beta effects on the field structure. Secondly, the orbit calculation should be performed using the MHD equilibrium field. Since there are a wide variety of the calculation codes and they all have their distinctive characteristics, the conditions and situations should be treated carefully. This thesis consists of seven chapters.

In Chapter 1, the introduction is described. The energetic alpha-particles are produced in the Deuterium-Tritium (DT) fusion reaction and they induce a lot of phenomena and problems. Especially, the confinement of the alpha particles is one of the most important issues to achieve the fusion reactor. The energetic ion losses are increased in the rippled tokamaks, when it is compared to the axisymmetric tokamaks. Not only the energetic ion confinement, but also other physics such as the plasma instability and the alpha heating are shown in this chapter.

In Chapter 2 and Chapter 3, the basic theories are described. The MHD equilibrium equation is finally derived from the Kilmontovich equations in Chapter 2. The MHD equilibrium calculation codes are introduced in Appendix A such as the VMEC code, the HINT code and the Grad-Shafranov equation. The orbit equations of the energetic ions in the rippled tokamaks are described in Chapter 3. Due to the non-axisymmetric field component, the new kinds of the orbits should be taken into account such as the banana drift, the ripple resonance and the deeply ripple-trapped particles. These trapped particles are easily affected by the magnetic field contour line. Since the diamagnetic effect strongly alters the field contour in the high-beta plasmas, the finite beta effects are quite important for the confinement of the energetic ion losses.

In Chapter 4, the finite beta effects on the magnetic field structure and the orbits of the energetic ions are clarified. To investigate these issues, the MHD equilibrium is calculated using the VMEC code in an ITER-like plasma and the orbit of the energetic ions are calculated using the GCB code. The finite beta effects on the ripple ratio are categorized by two parts: the axisymmetric and the non-axisymmetric finite beta effects. In the center of a plasma, both effects increase the ripple ratio. While, the axisymmetric finite beta effect decreases the ripple ratio at the outer torus. The decrease of the ripple ratio by the axisymmetric finite beta effect is strongly larger than the increase of it because

of the non-axisymmetric finite beta effect. Therefore, the finite beta effects increase the ripple ratio in the center of a plasma and decrease it at the outer torus. The diamagnetic effect reduces the field strength and alter the field contour structure. It significantly bends the field contour line in a high-beta plasma and produces two opposing effects: 1) the reduction of the energetic ion losses due to the closed field line contour and 2) increase of these losses due to the field contour line bending effect.

In Chapter 5, the problem of the VMEC code about the calculation region is resolved. The full three-dimensional (3D) MHD equilibria can be easily obtained by the VMEC code, while the calculation region is limited to the inside plasma region because the flux coordinates are used in this code. However, the equilibrium magnetic field between the plasma boundary and the first wall is required to quantitatively evaluate the energetic ion losses. In this study, the field calculation code, which is based on the Biot-Savart law using the VMEC results, is developed. The computation accuracy of the field component obtained by this method is sufficiently high; it is less than 0.3 % in the plasma boundary.

In Chapter 6, the finite beta effects on the energetic ion losses are quantitatively evaluated. The MHD equilibrium is calculated using the VMEC code and the orbits of fusion alpha particles are followed by using the fully three-dimensional magnetic field orbit-following Monte Carlo code. In the relatively low-beta plasmas, the changes in the magnetic field component due to the plasma current negligibly affect the confinement of the alpha particles except for the Shafranov shift effect. However for the high-beta plasmas, the diamagnetic effect reduces the magnetic field strength and significantly increases the alpha particle losses. In these high-beta cases, the non-axisymmetric field component generated by the equilibrium current also increases these losses, but not as effectively as compared to the diamagnetic effect.

In Chapter 7, the conclusions are shown. Finally, the summary of the important results are briefly shown by a run of the item.

Contents

Chapter 1

Introduction

1.1 History of the research

Nuclear fusion power is a fascinating energy to resolve the energy problems because there are huge amount of resources in the world. In addition to that, the fusion energy is assumed as a clean energy since the carbon dioxide (CO_2) is not emitted in the fusion reaction.

There are several kinds of nuclear fusion reactions such as Deuterium-Deuterium (DD) reaction, Deuterium-Helium reaction and Deuterium-Tritium (DT) reaction. Because the DT reactions have the most efficient rate in a relatively low temperature plasma, it is expected to use for the nuclear fusion reactor. The energetic alpha particles are produced in the DT reactions:

$$\mathrm{D} + \mathrm{T} \rightarrow \alpha\ (3.5\mathrm{MeV}) + \mathrm{n}\ (14.1\mathrm{MeV}). \tag{1.1}$$

The fusion alpha particles heat the plasma and alter the magnetrohydrodynamics (MHD) equilibrium. Moreover, these particles might damage the reactor wall if they hit the wall. Since the alpha particle physics is quite important to achieve the fusion reactor, a lot of researches have been performed until now.

To generate the fusion reaction, the DT plasmas should be heated. Due to the external heating, the fusion reaction can be occurred over 10keV plasma and the energetic alpha particles are produced in this reaction. There are mainly two methods to heat the plasma externally: the radio-frequency (RF) heating which supplies energy by the electromagnetic wave and the neutral beam injection (NBI) heating which gives energy by the Coulomb collision of the energetic ions. Fusion energy gain factor Q which is the ratio between the total fusion energy (e.g., 17.6MeV for the DT reaction) and the external heating energy. Because the power-generating plant is not meaningful when the Q is not less than unity, $Q = 1$ is one of the criterion conditions for the power plant. According to the experimental data of the Joint European Torus (JET) in the European Union (EU), $Q = 1$ can be achieved in the DT plasma which consists of 50% Deuterium and 50% Tritium. While,

the high Q is needed to increase the economical efficiency in the fusion reactors. Since the neutrons have the high penetrating power and do not interact with the DT plasma, they could not give energy to the plasma. Whereas, the energy of the fusion alpha particles can be used to heat the DT plasma. This heating process is called alpha heating. By using the alpha heating instead of the external heating, Q value can be increased. Although the external heating should be zero to ultimately achieve the self-ignition condition (i.e., $Q \to \infty$), it is not always necessary for the realistic fusion reactor. It is said that Q should exceed 20 to keep the economical efficiency comparing to other power plants [1]. In the future experimental reactor International Thermonuclear Experimental Reactor (ITER), Q is expected to exceed 10 for 15MA scenario and 5 for 9MA scenario. ITER is a tokamak fusion reactor which is conducted by seven member entities: the EU, India, Japan, China, Russia, South Korea and the United States. ITER is constructed in Cadarache, France, but Japan also intend to support with the investment, the procurement of experimental instruments and the dispatch of a lot of researchers. The past experimental devices could not continuously generate the fusion energy and the maximum momentary value was only 16MW in the JET in 1997. While ITER is expected to generate 500MW output and it will become the first fusion reactor around the world. This experiment is also expected to clarify high energetic alpha particles physics. Not only the experimental research, but also the theoretical study and the numerical analysis can help to understand the alpha particles physics. In this section, the three kinds of theoretical research about the alpha particles can be introduced: (1) the instability of plasma due to the alpha particles, (2) the alpha heating and (3) the fusion alpha particle losses.

Since the fusion alpha particles have high energy (3.5MeV), they can easily exceed the Alfven velocity (i.e., $v_{\mathrm{A}} = B(2\mu_0\rho_{\mathrm{m}})^{-1/2}$). Therefore, the instability with respect to the Alfven wave can be emerged. As can be seen in the example of NBI ions, the fish-bone instability can be observed when the energetic ion losses keep in phase with the MHD wave oscillation. When the fusion reactions resonate with the oscillation of the magnetic field, the fish-bone instability can be also happened by the fusion alpha particles.

The toroidicity-induced Alfven eigen-mode (TAE) is also important as a new kind of the long-wavelength instability. This instability can be found when the untrapped alpha particles have the same order of the velocity with the Alfven velocity. Although, the shear Alfven wave usually has the continuous spectrum, the hole of the wave-frequency spectrum exists in the torus-system. If the resonant frequency correspond with the spectrum gap, the Alfven wave could not be decayed by the continuum damping and the TAE instability appears. Since the TAE instability depends on the shear Alfven velocity, the growth rate depends on the safety-factor value and the plasma current. Therefore, the plasma instability can be controlling by the plasma current.

Since the alpha particles have the electric charge, they transfer their energy to the plasma through the Coulomb collisions. This energy affects on the fusion energy gain factor Q which determines the performance of the fusion reactor. Unless the particles do not hit the reactor wall, they give the kinetic energy to the plasma until they reach to

the thermal energy. The slowing down time is the characteristic lost time for the target ions. It is proportional to $T_{\rm i}^{3/2}$ and inversely proportional to $n_{\rm e}$, where $T_{\rm i}$ is the energy of ions and $n_{\rm e}$ is the density of electrons, respectively. If $n_{\rm e} = 1.0^{20}$ m^3 and the energy of alpha particles $T_{\rm i} = 3.5$ MeV, the slowing down time $\tau_{\rm s}$ for fusion alpha particles becomes approximately 0.1 s. Therefore, the fusion alpha particles should be confine for 0.1 s to successfully obtain the energy from them.

The physics of alpha particle losses can be categorized whether the Coulomb collisions and the non-axisymmetric field component are included or not. In the axisymmetric tokamaks, since the toroidal component of the angular momentum can be conserved during the collisionless process, the projections of the trapped particles are completely closed on the poloidal cross-section. Therefore, most of energetic particles can be successfully confined in the axisymmetric tokamaks. However, the alpha particles, which are generated near the plasma surface, may lose their energy during the one-bounce time because of the large width of the banana orbit. This loss process is called first-orbit loss. Since the birth rate of the fusion alpha particles depends on the plasma pressure, only a few particles are generated around the plasma surfaces. Although the number of the first-orbit loss particles is not so many, the lost energy of one particle is high and it can damage the first wall significantly. Figure 1.1 shows the loss region of the first-orbit losses of the alpha particles in a circular tokamak [2]. The particles are deeply ripple-trapped by the TF ripples around $v_{\parallel} \sim 0$ and other region is caused by the first-orbit loss. The loss region spreads over a wide area especially in Fig. 1.1 (a). However the alpha particles are generated near the plasma core and the banana-width for a D-shaped tokamak is smaller than that for a circular tokamak. Therefore, the effect of the first-orbit losses is not so significant for the fusion alpha particles.

If the TF ripples are taken into account in the tokamaks, other loss process can be found. In the non-axisymmetric systems, the toroidal component of the angular momentum is not conserved and the sum of ∇B drift between the up-path and the down-path is not canceled. As the result, the orbit of a banana particle is not closed in the one-bounce time and the orbit may become ergotic even if the Coulomb collisions are ignored. The idea of the ergotic banana particles in the TF ripples was proposed by R. J. Goldsone in 1981 [3]. They experientially found the conditions that the banana orbits become ergotic in the circular tokamak. If the ripple ratio is larger than the GWB critical ripple ratio $\delta_{\rm GWB}$;

$$\delta > \delta_{\rm GWB} \approx \frac{1}{(N\pi q/\epsilon)^{3/2}\rho {\rm d}q/{\rm d}r}, \tag{1.2}$$

these particles become ergotic and lose their energy. Where N is the number of TFCs, q is the safety-factor value and ρ is the Larmor radius. Figure 1.2 shows the collisionless ergotic region in the circular tokamak. The dotted line shows the analytical solution obtained by the GWB condition and the solid line shows the numerical solution [2]. Especially at the outside of the torus, the numerical solution does not correspond with the GWB

analytical solution. Therefore, the GWB condition is only rough estimation. When the banana orbit becomes chaotic, the loss process can be treated as the diffusion phenomena by averaging with a lot of test particles. The diffusion efficiency of the ergotic banana orbit can be described as,

$$\begin{aligned} D &\sim \frac{\Delta r^2}{\tau_{\mathrm{b}}} \\ &\sim \frac{1}{16\sqrt{2}} \frac{N\pi}{\sin\theta_{\mathrm{b}}} \frac{v_{\perp}\rho^2 q^2 \delta^2}{R\epsilon^{5/2} K(\xi)} \end{aligned} \tag{1.3}$$

where Δr is the displacement of the orbit during the one-bounce motion, τ_{b} is the bounce time, θ_{b} is the poloidal angle on the reflection point, ξ is $\sin\frac{\theta_{\mathrm{b}}}{2}$ and K is the elliptic integral of the first kind. Moreover, the parallel velocity is approximately zero on the ripple well, these particles may be trapped by the TF ripples. In this case, the energetic particles may be lost for a quite short time due to the ∇B drift. Since these deeply ripple-trapped particles have high energy and they collide on the specific part of the reactor, it is the significant issue to design the fusion reactor.

If the Coulomb collisions are taken into account, the loss process can be treated as the diffusion phenomena. In the axisymmetric tokamaks, the neoclassical diffusion is dominant and it can be categorized by the collisional frequency. For the low collisional frequency, the particles can describe the banana orbit. Since the step width is correspond with the banana width, the diffusion coefficient is

$$D_{\mathrm{b}} = \epsilon^{1/2} \Delta_{\mathrm{bw}}^2 \nu \tag{1.4}$$

where Δ_{bw} is the banana width and ν is the collisional frequency. For the high collisional frequency, the particles could not describe the banana orbit because of the Coulomb collisions. In this Pfirsch-Schlüter region, the step size is not the Larmor radius but the displacement between the flux surface and the drift surface. Therefore, the diffusion coefficient is

$$D_{\mathrm{P.S}} = q^2 \rho^2 \nu. \tag{1.5}$$

The collisional frequency region between the banana region and the Pfirsch-Schlüter region is called plateau region. In this case, the diffusion coefficient can be obtained by the Vlasov equation,

$$D_{\mathrm{p}} = q^2 \rho^2 \nu_{\mathrm{P.S}} \tag{1.6}$$

where $\nu_{\mathrm{P.S}}$ is the minimum value of the collisional frequency for the Pfirsch-Schlüter region. The diffusion coefficient does not depend on the collisional frequency in the plateau region.

When the Coulomb collision and the TF ripples are taken into account, the diffusion becomes even more complex. If the energy of alpha particles is high and the collision

frequency is low, the ripple resonance region is dominant. Since the particles can describe the periodic banana orbit in this case, the collisionless orbit is important. The banana orbit is displaced in the radial direction during the one-bounce time by the TF ripples. The displacement depends on the toroidal angle at the banana tip. If the difference of the toroidal angle between adjacent banana tips always corresponds with the toroidal period, the particle drifts in the same radial direction. As the result, the radial displacement of the banana orbit is resonantly enhanced. This diffusion process is called ripple resonant diffusion. Because the alpha particles are not always trapped with the same toroidal angle, the ripple resonance does not significantly affect on the energetic ion losses. If the velocity of alpha particles is decreased and the mean collision time becomes shorter than the bounce time of the banana orbit, the ripple-plateau region is dominant. In this case, the particles could not describe the banana orbits due to the Coulomb collisions. The step size is the radial displacement of the banana orbit and the step time is the bounce time of the banana orbit. Therefore, the diffusion coefficient is

$$D_{\mathrm{rp}} = \frac{N\delta^2\rho_\theta^2 \upsilon}{R} \tag{1.7}$$

where, ρ_θ is the poloidal Larmor radius. In this region, the diffusion coefficient does not depend on the collisional frequency but depends on the kinetic energy. Figure 1.3 shows the energy E and ellipticity κ dependence of the diffusion coefficient D in the rippled tokamaks [2].

Whereas for the actual tokamaks, the energetic ion losses have to be calculated numerically. In these days, the orbits of large number of test particles are followed with consideration of the Coulomb collisions by the Monte Carlo method [4]. The numerical calculation results are highly consistent with the experimental results [5]. However, since the numerical analysis needs enormous computation time, there are not enough researches in this field. One of the most important research purposes is to estimate the distribution of the heat loads due to the fusion alpha particles. When the TF ripples are partially small, the damage on the reactor wall is more capital issue than the decrease of Q value. It affects on the safety and the economic efficiency of the fusion reactor. The deeply ripple-trapped particles tend to collide with a part of wall between TFCs. By inserting the Ferritic Inserts (FIs) under the TFCs, the TF ripples become smaller and the energetic ion losses are reduced. Shinohara et. al. clarified how FIs can reduce the energetic ion losses in an ITER plasma using the F3D-OFMC code [6]. The confinement of the alpha particles is significantly improved by decreasing ripple ratio especially on the reflection points. However, the FIs can produce the harmonic component of the TF ripples. Due to the harmonic component, N in Eq. (1.3) becomes larger and the ripple diffusion coefficient also becomes larger. To prevent from this issue, the FIs should be located well away from the plasma [7].

The equilibrium current flows in a plasma to keep the MHD equilibria and alters the magnetic field structure. This effects are called finite beta effects and the changes of the

field structure also affect the energetic ion losses. For the analysis of the energetic ion losses in the tokamak plasmas, the Grad-Shafranov (GS) equation has been usually used to obtain the MHD equilibrium field. Since the GS equation is 2D MHD equilibrium equation, the non-axisymmetry of the plasma could not be taken into account. Moreover, the finite beta effects on the toroidal field are ignored for the low-beta plasmas. In this case, the 3D magnetic field structure can be approximately obtained by superimposing the poloidal component of the equilibrium field on the vacuum TF ripples. Most of researchers targeted $\langle\beta\rangle \leq 2\%$ plasma like an ITER plasma in which the equilibrium current does not significantly alter the non-axisymmetric component and the toroidal component of the magnetic field. However, the plasma beta should be increased to improve the economical efficiency of the fusion reactor. A lot of researchers recently try to clarify the finite beta effects on the energetic ion losses in the high-beta plasmas. The 3D MHD equilibrium calculation code is required to consider the non-axisymmetry of plasmas. Strumberger et. al. and Suzuki et. al. analyzed these issues using the VMEC code [8][9]. As the results, several kinds of the finite beta effects are clarified, however, the effect of the field strength vending effect due to the diamagnetic effect is not sufficiently discussed. Moreover, most of these researches did not calculate the alpha particles orbits and did not quantitatively evaluate the finite beta effects on these losses. Therefore, both 3D MHD equilibrium equation and alpha particles orbits should be calculated.

Analysis using the HINT code, which can calculate the 3D MHD equilibria, is also important for the research of the energetic ion losses. Especially in the high-beta plasmas, the flux surfaces are disturbed around the plasma boundary. Moreover, if the edge localized modes (ELM) mitigation coils and the test blanket modules (TBMs) in an ITER operation are installed, the eigen toroidal mode is produced and the magnetic island structure can appear. The VMEC code could not be used in such situations because the nested flux surfaces are assumed to exit [10][11]. Whereas, the HINT code can calculate the 3D MHD equilibria in the real coordinates and consider the stochasticity of the flux surfaces and the magnetic island structure. Although HINT needs a lot of calculation time comparing to VMEC, it is one of the most important tool for the alpha particle losses.

Since the high Q value is expected in an ITER operation, the alpha particles confinement is quite important issue. A lot of researchers evaluated alpha particle losses in an ITER plasma. In an ITER operation, the volume-averaged beta $\langle\beta\rangle$ is about 2%, the aspect ratio is approximately 2.8, the number of TFCs is 18, and the maximum ripple ratio in a plasma is approximately 1.0%. Therefore, the ITER is conservative design and the alpha particle losses are not so effective. The troyon beta limit is described as below [12];

$$\langle\beta\rangle \leq \beta_{\mathrm{N}} \frac{I_{\mathrm{pl}}}{aB_0} \sim \frac{5\kappa}{q_{\mathrm{a}}} \beta_{\mathrm{N}} \epsilon, \tag{1.8}$$

where β_{N} is the troyon coefficient, ϵ is the inverse aspect ratio, I_{pl} is the plasma current, κ

is ellipticity, and q_a is the safety-factor at the plasma surface. When the troyon coefficient is assumed to be 5, the plasma beta limit is approximately 3% in 9MA ITER operation. $\langle\beta\rangle = 3\%$ plasma in an ITER configuration is not realistic actually. Therefore, it is also important for the analysis in other realistic tokamaks such as the low aspect ratio tokamaks and spherical tokamaks (STs), if the physics of the high-beta plasma is focused on.

1.2 Research model

The research model is shown in this section. The calculation model is a realistic D-shaped tokamak consisting of 18 TFCs [8][13]. It is referred by the 9MA scenario of an ITER operation. The parameters are shown in Tab. 1.1. The non-axisymmetric field component is generated only by the TFCs in this study and any ferrite materials are ignored. The TFC positions have toroidal angles ϕ given by

$$\phi = \frac{2\pi}{18}\mathrm{k} \quad (\mathrm{k} = 0, 1, ..., 17).$$

Figures 1.4(a) and (b), respectively, show the plasma pressure P profile which is normalized by the peak pressure P_{axis} and the safety-factor q profile as a function of the normalized toroidal magnetic flux s. Considering the P/P_{axis} profile, q profile and the shape of plasma boundary, the MHD equilibrium is calculated using VMEC by changing the plasma beta. The peak pressure P_{axis} and the volume-averaged beta value $\langle\beta\rangle$ is changed depending on the calculation. Figure 1.4(c) shows the ripple ratio δ for the vacuum field on the poloidal cross-section. The ripple ratio δ along the toroidal angle ϕ is defined by

$$\delta = \frac{B_{\mathrm{max}} - B_{\mathrm{min}}}{B_{\mathrm{max}} + B_{\mathrm{min}}}, \tag{1.9}$$

where B_{max} and B_{min} are respectively the maximum and minimum field strengths $|B|$ along the toroidal angle. In this study, δ_{vac} is less than 0.01 in a plasma region and it is same for all calculations.

1.3 Compositions of thesis

The remainder of the paper is organized as follows. In Chapter 2 and Chapter 3, the detailed MHD equilibrium equations and the typical orbit of the energetic ions in the rippled tokamaks are introduced, respectively. The calculation method of the equilibrium field in the vacuum region using the VMEC results is introduced in Chapter 4. The mechanism of the finite beta effects of lost particles are discussed in Chapter 5. The loss power fraction of the alpha particles are quantitatively evaluated in Chapter 6. Finally, the summary and conclusions are shown in Chapter 7.

Table 1.1: The parameters of an ITER operation

Major radius	R_{maj} = 6.1 m
Minor radius	r_{minor} = 2.5 m
Aspect ratio	A = 3.1
Plasma current	I_p = 9 MA
Vacuum toroidal field at R = 6.1 m	B_{tor} = 5.4 T
Maximum toroidal field	B_{tor} = 11.5 T
Number of TFCs	N_{coil} = 18
Maximum ripple ratio	δ = 1%

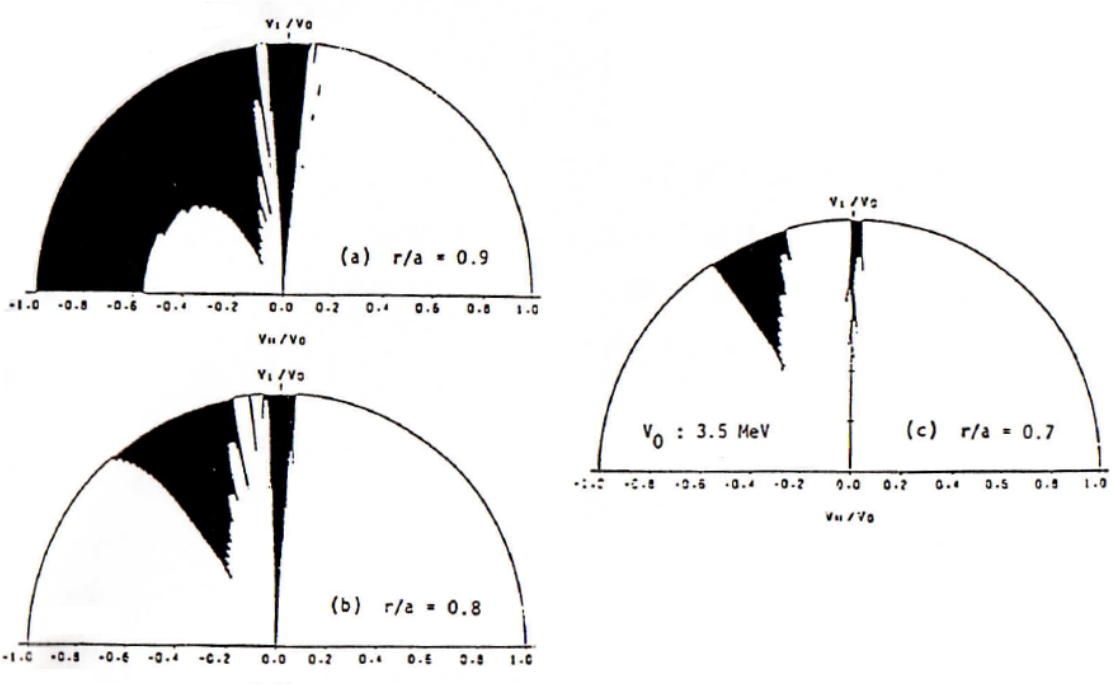

Figure 1.1: The loss region of the first-orbit losses of the alpha particle losses in a circular tokamak. (a) $r/a = 0.9$, (b) 0.8, (c) 0.7 [2].

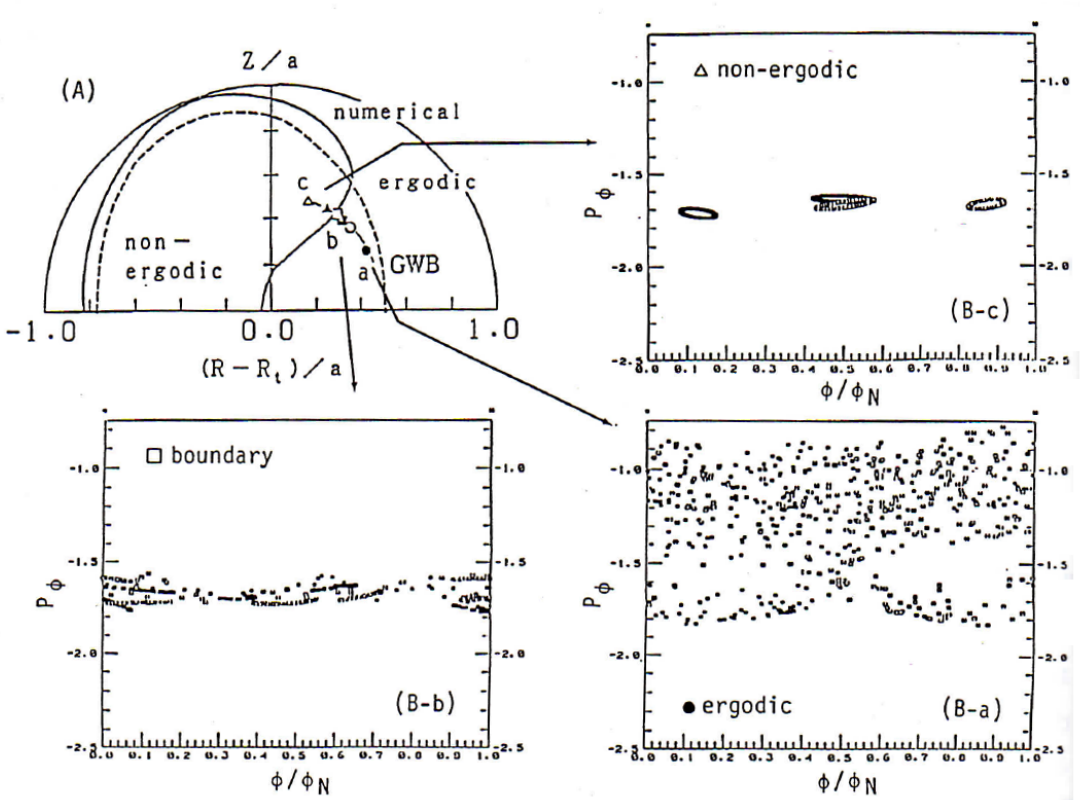

Figure 1.2: The collisionless ergotic region in a circular tokamak. The dotted line shows the analytical solution obtained by the GWB condition and the solid line shows the numerical solution [2].

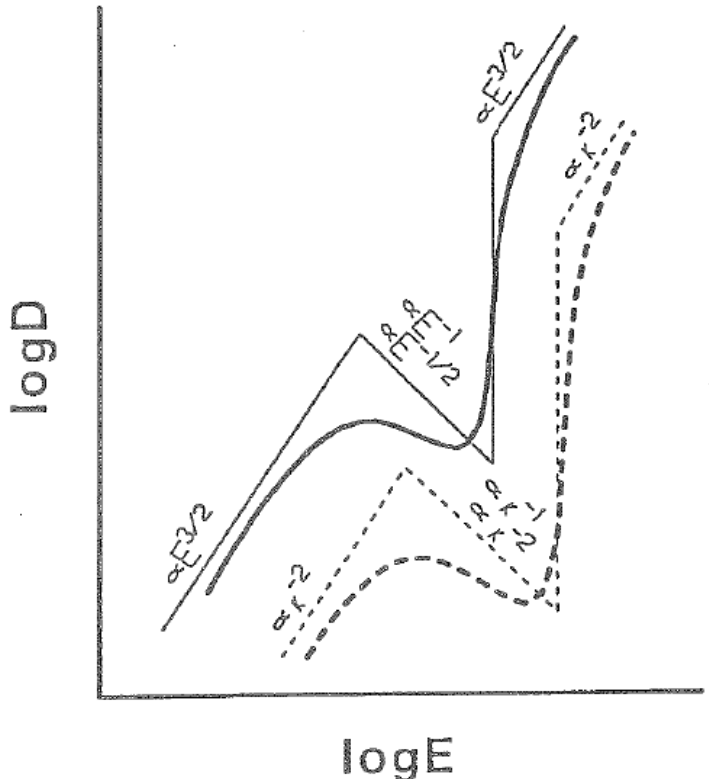

Figure 1.3: The energy E and the ellipticity κ dependence of the diffusion coefficient D in the rippled tokamaks [2].

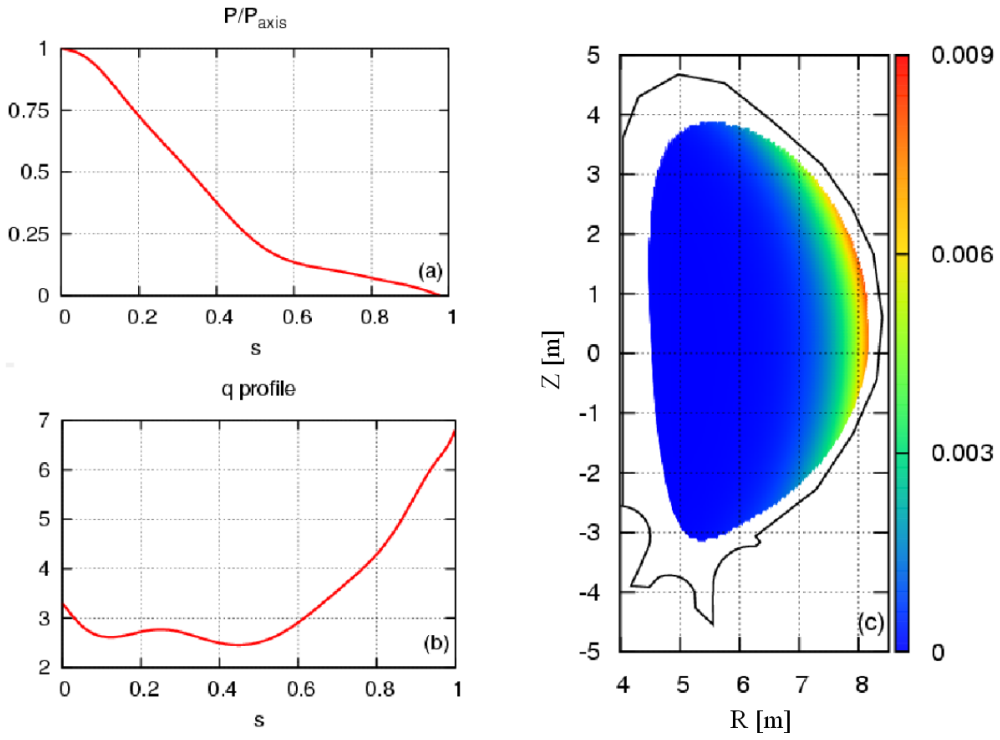

Figure 1.4: (a) The pressure $P/P_{\rm axis}$ profile and (b) the safety-factor q profile as a function of the normalized toroidal magnetic flux s, and (c) $\delta_{\rm vac}$ on the poloidal cross-section.

Chapter 2

MHD equilibrium equation

2.1 Fusion plasma

If the gas molecules and the atoms are heated, these particles can be ionized. These particles are called plasmas. In the fusion reactors, the Deuterium and the Tritium atoms are heated and they can turn into plasmas. If the magnetic field is used to confine these charged particles, the effect of plasmas on the field structure should be clarified. For this purpose, the magnetrohydrodynamics (MHD) is commonly used by assuming the plasma to be one kind of electrically-charged fluid. In this section, the MHD equation is introduced [14].

2.2 Klimontovich equation

Firstly, the Klimontovich equation for the discrete distribution functions is derived. The discrete distribution functions for a certain particle σ is defined as below,

$$F_\sigma(\boldsymbol{r}, \boldsymbol{v}, t)) = \sum_j \delta[\boldsymbol{r} - \boldsymbol{r}_j(t)]\delta[\boldsymbol{v} - \boldsymbol{v}_j(t)]. \tag{2.1}$$

If the collisions can be ignored, the number of the particles in a volume element $\mathrm{d}\boldsymbol{r}\mathrm{d}\boldsymbol{v}$ remains constant. Therefore, the distribution functions can be written as below,

$$\frac{\mathrm{d}F_\sigma}{\mathrm{d}t} = \frac{\partial F_\sigma}{\partial t} + \boldsymbol{v} \cdot \frac{\partial F_\sigma}{\partial \boldsymbol{r}} + \dot{\boldsymbol{v}} \cdot \frac{\partial F_\sigma}{\partial \boldsymbol{v}} = 0. \tag{2.2}$$

The motion equations for plasma are written as,

$$m_j \frac{\mathrm{d}\boldsymbol{v}_\mathrm{i}}{\mathrm{d}t} = q_j \left(\boldsymbol{E} + \boldsymbol{v}_\mathrm{i} \times \boldsymbol{B}\right). \tag{2.3}$$

By substituting Eq. (2.3) into Eq. (2.2),

$$\frac{\partial F_\sigma}{\partial t} + \boldsymbol{v} \cdot \frac{\partial F_\sigma}{\partial \boldsymbol{r}} + \frac{q_\sigma}{m_\sigma} \left(\boldsymbol{E} + \boldsymbol{v} \times \boldsymbol{B}\right) \cdot \frac{\partial F_\sigma}{\partial \boldsymbol{v}} = 0. \tag{2.4}$$

This equation is called Klimontovich equation for the discrete distribution functions with respect to position, velocity and time.

2.3 Boltzmann equation

To solve the Klimontovich equation, the accurate initial conditions with respect to positions and velocities are required for all particles. However, it is difficult to know these informations, so the smooth motion equation is introduced by statistically averaging the distribution functions. In this section, $\langle * \rangle$ shows statistical average and δ shows the statistical error. The distribution function, the electric filed and the magnetic field can be written as below,

$$\begin{aligned} F_\sigma(\boldsymbol{r},\boldsymbol{v},t) &= f_\sigma(\boldsymbol{r},\boldsymbol{v},t) + \delta F_\sigma(\boldsymbol{r},\boldsymbol{v},t) \\ \boldsymbol{E}(\boldsymbol{r},\boldsymbol{v},t) &= \langle \boldsymbol{E}(\boldsymbol{r},\boldsymbol{v},t) \rangle + \delta \boldsymbol{E}(\boldsymbol{r},\boldsymbol{v},t) = \boldsymbol{E}(\boldsymbol{r},\boldsymbol{v},t) + \delta \boldsymbol{E}(\boldsymbol{r},\boldsymbol{v},t) \\ \boldsymbol{B}(\boldsymbol{r},\boldsymbol{v},t) &= \langle \boldsymbol{B}(\boldsymbol{r},\boldsymbol{v},t) \rangle + \delta \boldsymbol{B}(\boldsymbol{r},\boldsymbol{v},t) = \boldsymbol{B}(\boldsymbol{r},\boldsymbol{v},t) + \delta \boldsymbol{B}(\boldsymbol{r},\boldsymbol{v},t). \end{aligned} \tag{2.5}$$

By substituting these equations into the Klimontovich equation, Eq. (2.4) can be written as below,

$$\begin{gathered} \frac{\partial f_\sigma}{\partial t} + \boldsymbol{v} \cdot \frac{\partial f_\sigma}{\partial \boldsymbol{r}} + \frac{q_\sigma}{m_\sigma} (\boldsymbol{E} + \boldsymbol{v} \times \boldsymbol{B}) \cdot \frac{\partial f_\sigma}{\partial \boldsymbol{v}} = C_k \\ \left(C_k = -\frac{q_\sigma}{m_\sigma} \langle (\delta \boldsymbol{E} + \boldsymbol{v} \times \delta \boldsymbol{B}) \cdot \frac{\partial \delta F_\sigma}{\partial \boldsymbol{v}} \rangle \right), \end{gathered} \tag{2.6}$$

where, C_k shows the collision term. This equation is called the Boltzmann equation.

2.4 Moment equation

If the Boltzmann equation is multiplied by the weighting function about $\boldsymbol{v}$ and integrated it over the velocity space, the moment equations can be obtained. The continuity equation, the motion equation and the energy balance equation can be derived from the zeroth, the first and the second order moment equation, respectively. In this section, the zeroth and the first moment equation are derived.

Firstly, the Boltzmann equation is integrated over the velocity space,

$$\int \left(\frac{\partial f_\sigma}{\partial t} + \boldsymbol{v} \cdot \frac{\partial f_\sigma}{\partial \boldsymbol{r}} + \frac{q_\sigma}{m_\sigma} (\boldsymbol{E} + \boldsymbol{v} \times \boldsymbol{B}) \cdot \frac{\partial f_\sigma}{\partial \boldsymbol{v}} \right) \mathrm{d}\boldsymbol{v} = \int C_k \mathrm{d}\boldsymbol{v}.$$

If the creation and the annihilation of the particles are ignored, the above equations can be written as below,

$$\frac{\partial n_\sigma}{\partial t} + \int \left[\nabla \cdot (\boldsymbol{v} f_\sigma) + \frac{q_\sigma}{m_\sigma} \nabla_v \cdot \{ (\boldsymbol{E} + \boldsymbol{v} \times \boldsymbol{B}) f_\sigma \} \right] \mathrm{d}\boldsymbol{v} = 0.$$

By using the Gauss's divergence theorem, it can be written as below,

$$\frac{\partial n_\sigma}{\partial t} + \nabla \cdot (n \boldsymbol{u}_\sigma(\boldsymbol{r}, t)) + \frac{q_\sigma}{m_\sigma} \int (\boldsymbol{E} + \boldsymbol{v} \times \boldsymbol{B}) f_\sigma \cdot \mathrm{d}\mathbf{S}_v = 0, \tag{2.7}$$

where n_σ is the particle number density and $\boldsymbol{u}_\sigma$ is the fluid velocity, which are respectively defined as below,

$$\begin{aligned} n_\sigma &= \int f_\sigma \mathrm{d}\boldsymbol{v} \\ \boldsymbol{u}_\sigma &= \int \boldsymbol{v} f_\sigma \mathrm{d}\boldsymbol{v}. \end{aligned}$$

Moreover, f_σ becomes zero in the case of $v \to \infty$, therefore the third term in Eq. (2.7) becomes zero. Therefore, the zeroth order momentum equation can be written as below,

$$\frac{\partial n_\sigma}{\partial t} + \nabla \cdot (n_\sigma \boldsymbol{u}_\sigma(\boldsymbol{r}, t)) = 0. \tag{2.8}$$

This equation is called the equation of continuity.

Secondly, the Boltzmann equation is multiplied by $m_\sigma \boldsymbol{v}$ and integrated it over the velocity space.

$$\begin{aligned} \int m_\sigma \boldsymbol{v} \left(\frac{\partial f_\sigma}{\partial t} + \boldsymbol{v} \cdot \frac{\partial f_\sigma}{\partial \boldsymbol{r}} + \frac{q_\sigma}{m_\sigma} (\boldsymbol{E} + \boldsymbol{v} \times \boldsymbol{B}) \cdot \frac{\partial f_\sigma}{\partial \boldsymbol{v}} \right) \mathrm{d}\boldsymbol{v} &= \int m_\sigma \boldsymbol{v} C_k \mathrm{d}\boldsymbol{v} \\ m_\sigma \frac{\partial (n_\sigma \boldsymbol{u}_\sigma)}{\partial t} + \int \left[m_\sigma \nabla \cdot (\boldsymbol{v}\boldsymbol{v} f_\sigma) + q_\sigma \boldsymbol{v} (\boldsymbol{E} + \boldsymbol{v} \times \boldsymbol{B}) \cdot \nabla_v f_\sigma \right] \mathrm{d}\boldsymbol{v} &= \boldsymbol{F}_\sigma \end{aligned} \tag{2.9}$$

The second term in Eq. (2.9) is the divergence of the stress tensor and it is written as below,

$$\begin{aligned} \mathbf{M}_\sigma &= m_\sigma \int \boldsymbol{v}\boldsymbol{v} f_\sigma \mathrm{d}\boldsymbol{v} \\ &= m_\sigma \int (\boldsymbol{v} - \boldsymbol{u}_\sigma + \boldsymbol{u}_\sigma)(\boldsymbol{v} - \boldsymbol{u}_\sigma + \boldsymbol{u}_\sigma) f_\sigma \mathrm{d}\boldsymbol{v} \\ \therefore \ \mathbf{M}_\sigma &= n_\sigma m_\sigma \boldsymbol{u}_\sigma \boldsymbol{u}_\sigma + \mathbf{P}_\sigma \\ \mathbf{P}_\sigma &= m_\sigma \int (\boldsymbol{v} - \boldsymbol{u}_\sigma)(\boldsymbol{v} - \boldsymbol{u}_\sigma) f_\sigma \mathrm{d}\boldsymbol{v}. \end{aligned}$$

Where $\mathbf{P}_\sigma$ is the pressure tensor. It is defined as below,

$$\begin{aligned} \mathbf{P}_\sigma &= p_\sigma \boldsymbol{I} + \boldsymbol{\Pi}_\sigma \\ p_\sigma &= \frac{1}{3} \mathrm{tr}\ \mathbf{P}_\sigma = \frac{1}{3} m_\sigma \int (\boldsymbol{v} - \boldsymbol{u}_\sigma)^2 f_\sigma \mathrm{d}\boldsymbol{v} \\ \therefore \ p_\sigma &= n_\sigma T_\sigma. \end{aligned}$$

where, p_σ is the isotropic component and $\mathbf{\Pi}_\sigma$ is the anisotropic component of the pressure tensor. The third term in Eq. (2.9) is written as below,

$$\begin{aligned}
\int \left[q_\sigma \boldsymbol{v}\left(\boldsymbol{E}+\boldsymbol{v}\times\boldsymbol{B}\right)\cdot\nabla_v f_\sigma\right]\mathrm{d}\boldsymbol{v} &= -q_\sigma\int f_\sigma\nabla_v\cdot\left(\boldsymbol{v}\left(\boldsymbol{E}+\boldsymbol{v}\times\boldsymbol{B}\right)\right)\mathrm{d}\boldsymbol{v}\\
&= -q_\sigma n_\sigma\boldsymbol{E}+q_\sigma\int f_\sigma\nabla_v\cdot\left(\boldsymbol{v}\left(\boldsymbol{v}\times\boldsymbol{B}\right)\right)\mathrm{d}\boldsymbol{v}\\
&= -q_\sigma n_\sigma\boldsymbol{E}+q_\sigma\int f_\sigma\left(\boldsymbol{v}\times\boldsymbol{B}\right)\mathrm{d}\boldsymbol{v}\\
&= -q_\sigma n_\sigma\left(\boldsymbol{E}+\boldsymbol{u}_\sigma\times\boldsymbol{B}\right).
\end{aligned}$$

As described above, the first order moment equation can be written as below,

$$m_\sigma\frac{\partial\left(n_\sigma\boldsymbol{u}_\sigma\right)}{\partial t}+\nabla\cdot\mathbf{M}_\sigma=n_\sigma q_\sigma\left(\boldsymbol{E}+\boldsymbol{u}_\sigma\times\boldsymbol{B}\right)+\boldsymbol{F}_\sigma. \tag{2.10}$$

This equation is called the motion equation.

The energy balance equation can be obtained from the second momentum equation.

$$\frac{\partial W_\sigma}{\partial t}+\nabla\cdot\mathbf{Q}_\sigma=n_\sigma q_\sigma\boldsymbol{u}_\sigma\cdot\boldsymbol{E}+R_\sigma, \tag{2.11}$$

where W_σ is the energy density, $\mathbf{Q}_\sigma$ is the energy flux and R_σ is the energy exchange due to the collisions. They are respectively defined as below,

$$\begin{aligned}
W_\sigma &= \frac{m_\sigma}{2}\int v^2 f_\sigma\mathrm{d}\boldsymbol{v}\\
\mathbf{Q}_\sigma &= \frac{m_\sigma}{2}\int v^2\boldsymbol{v} f_\sigma\mathrm{d}\boldsymbol{v}\\
R_\sigma &= \frac{m_\sigma}{2}\int C_\sigma v^2\mathrm{d}\boldsymbol{v}.
\end{aligned}$$

2.5 Two-fluids equation

The moment equations are satisfied for each kind of particles. For example, if the plasma consists of the electron and the plus charged ion with the electric charge Z, they can be described by the two-fluids equation. The zeroth, the first and the second equations for

the electrons and ions are respectively written as,

$$\frac{\partial n_{\mathrm{e}}}{\partial t} + \nabla \cdot (n_{\mathrm{e}} \boldsymbol{u}_{\mathrm{e}}(\boldsymbol{r}, t)) = 0 \tag{2.12}$$

$$\frac{\partial n_{\mathrm{i}}}{\partial t} + \nabla \cdot (n_{\mathrm{i}} \boldsymbol{u}_{\mathrm{i}}(\boldsymbol{r}, t)) = 0 \tag{2.13}$$

$$m_{\mathrm{e}} \frac{\partial (n_{\mathrm{e}} \boldsymbol{u}_{\mathrm{e}})}{\partial t} + \nabla \cdot \mathbf{M}_{\mathrm{e}} = -e n_{\mathrm{e}} (\boldsymbol{E} + \boldsymbol{u}_{\mathrm{e}} \times \boldsymbol{B}) + \boldsymbol{F} \tag{2.14}$$

$$m_{\mathrm{i}} \frac{\partial (n_{\mathrm{i}} \boldsymbol{u}_{\mathrm{i}})}{\partial t} + \nabla \cdot \mathbf{M}_{\mathrm{i}} = Z e n_{\mathrm{i}} (\boldsymbol{E} + \boldsymbol{u}_{\mathrm{i}} \times \boldsymbol{B}) - \boldsymbol{F} \tag{2.15}$$

$$\frac{\partial W_{\mathrm{e}}}{\partial t} + \nabla \cdot \mathbf{Q}_{\mathrm{e}} = -e n_{\mathrm{e}} \boldsymbol{u}_{\mathrm{e}} \cdot \boldsymbol{E} + R \tag{2.16}$$

$$\frac{\partial W_{\mathrm{i}}}{\partial t} + \nabla \cdot \mathbf{Q}_{\mathrm{i}} = Z e n_{\mathrm{i}} \boldsymbol{u}_{\mathrm{i}} \cdot \boldsymbol{E} - R. \tag{2.17}$$

The sum of the momentum and the energy are constant for all particles, the following conditions can be used,

$$\boldsymbol{F} = \boldsymbol{F}_{\mathrm{e}} = -\boldsymbol{F}_{\mathrm{i}} \tag{2.18}$$

$$R = R_{\mathrm{e}} = -R_{\mathrm{i}}. \tag{2.19}$$

2.6 Single-fluid equation

In the single-fluid equation, the plasma consists of the electrons and the monovalent plus ions. In this equation, the mass density $\rho \equiv \Sigma n_\sigma m_\sigma$, the mass velocity $\boldsymbol{u} \equiv \Sigma n_\sigma m_\sigma \boldsymbol{u}_\sigma / \rho$, the charge density $\sigma \equiv \Sigma n_\sigma q_\sigma$ and the current density $\boldsymbol{j} \equiv \Sigma q_\sigma m_\sigma \boldsymbol{u}_\sigma$ are used. By summing the moment equations for electrons and ions,

The equation of continuity:

$$\frac{\partial \rho}{\partial t} + \nabla \cdot (\rho \boldsymbol{u}) = 0 \tag{2.20}$$

The motion equation:

$$\frac{\partial (\rho \boldsymbol{u})}{\partial t} + \nabla \cdot (\rho \boldsymbol{u}\boldsymbol{u} + \mathbf{P}) = \sigma \boldsymbol{E} + \boldsymbol{j} \times \boldsymbol{B} \tag{2.21}$$

The energy balance equation:

$$\frac{\partial}{\partial t} \left(\frac{1}{2} \rho u^2 + \frac{3}{2} p \right) + \nabla \cdot \left(\frac{1}{2} \rho u^2 \boldsymbol{u} + \frac{3}{2} p \boldsymbol{u} + \mathbf{P} \cdot \boldsymbol{u} + \mathbf{q} \right) = \boldsymbol{j} \cdot \boldsymbol{E} \tag{2.22}$$

In this section, the equation of continuity and the motion equation are derived.

If the equation of continuity for each particle are multiplied by each mass and two equations are summed, the equation of continuity for the single-fluid equation can be obtained.

$$\frac{\partial(n_\mathrm{e}m_\mathrm{e}+n_\mathrm{i}m_\mathrm{i})}{\partial t}+\nabla\cdot(n_\mathrm{e}m_\mathrm{e}\boldsymbol{u}_\mathrm{e}+n_\mathrm{i}m_\mathrm{i}\boldsymbol{u}_\mathrm{i})=0$$
$$\frac{\partial\rho}{\partial t}+\nabla\cdot(\rho\boldsymbol{u})=0 \tag{2.23}$$

If the motion equation for each particle are summed,

$$\frac{\partial(\rho\boldsymbol{u})}{\partial t}+\nabla\cdot(n_\mathrm{e}m_\mathrm{e}\boldsymbol{u}_\mathrm{e}\boldsymbol{u}_\mathrm{e}+n_\mathrm{i}m_\mathrm{i}\boldsymbol{u}_\mathrm{i}\boldsymbol{u}_\mathrm{i}+\mathbf{P}_\mathrm{e}+\mathbf{P}_\mathrm{i})=\sigma\boldsymbol{E}+\boldsymbol{j}\times\boldsymbol{B}$$
$$\frac{\partial(\rho\boldsymbol{u})}{\partial t}+\nabla\cdot\{n_\mathrm{e}m_\mathrm{e}\boldsymbol{u}_\mathrm{e}(\boldsymbol{u}+\delta\boldsymbol{u}_\mathrm{e})+n_\mathrm{i}m_\mathrm{i}\boldsymbol{u}_\mathrm{i}(\boldsymbol{u}+\delta\boldsymbol{u}_\mathrm{i})+\mathbf{P}\}=\sigma\boldsymbol{E}+\boldsymbol{j}\times\boldsymbol{B}$$
$$\frac{\partial(\rho\boldsymbol{u})}{\partial t}+\nabla\cdot(\rho\boldsymbol{u}\boldsymbol{u})+\nabla\cdot(\mathbf{P}+n_\mathrm{e}m_\mathrm{e}\boldsymbol{u}_\mathrm{e}\delta\boldsymbol{u}_\mathrm{e}+n_\mathrm{i}m_\mathrm{i}\boldsymbol{u}_\mathrm{i}\delta\boldsymbol{u}_\mathrm{i})=\sigma\boldsymbol{E}+\boldsymbol{j}\times\boldsymbol{B}.$$

Where,

$$\begin{aligned}\rho\boldsymbol{u}\boldsymbol{u}=n_\mathrm{e}m_\mathrm{e}\boldsymbol{u}\boldsymbol{u}+n_\mathrm{i}m_\mathrm{i}\boldsymbol{u}\boldsymbol{u} &= n_\mathrm{e}m_\mathrm{e}\boldsymbol{u}_\mathrm{e}\boldsymbol{u}+n_\mathrm{i}m_\mathrm{i}\boldsymbol{u}_\mathrm{i}\boldsymbol{u}\\ n_\mathrm{e}m_\mathrm{e}\delta\boldsymbol{u}_\mathrm{e}\boldsymbol{u}+n_\mathrm{i}m_\mathrm{i}\delta\boldsymbol{u}_\mathrm{i}\boldsymbol{u} &= 0\\ n_\mathrm{e}m_\mathrm{e}\boldsymbol{u}_\mathrm{e}\delta\boldsymbol{u}_\mathrm{e}+n_\mathrm{i}m_\mathrm{i}\boldsymbol{u}_\mathrm{i}\delta\boldsymbol{u}_\mathrm{i} &= n_\mathrm{e}m_\mathrm{e}\delta\boldsymbol{u}_\mathrm{e}\delta\boldsymbol{u}_\mathrm{e}+n_\mathrm{i}m_\mathrm{i}\delta\boldsymbol{u}_\mathrm{i}\delta\boldsymbol{u}_\mathrm{i}\end{aligned}$$

Therefore,

$$\frac{\partial(\rho\boldsymbol{u})}{\partial t}+\nabla\cdot(\rho\boldsymbol{u}\boldsymbol{u})+\nabla\cdot(\mathbf{P}+n_\mathrm{e}m_\mathrm{e}\delta\boldsymbol{u}_\mathrm{e}\delta\boldsymbol{u}_\mathrm{e}+n_\mathrm{i}m_\mathrm{i}\delta\boldsymbol{u}_\mathrm{i}\delta\boldsymbol{u}_\mathrm{i})=\sigma\boldsymbol{E}+\boldsymbol{j}\times\boldsymbol{B}$$

The pressure tensor for each particle in a single-fluid model is defined as,

$$\begin{aligned}\mathbf{P}^*_\sigma &= m_\sigma\int(\boldsymbol{v}-\boldsymbol{u})(\boldsymbol{v}-\boldsymbol{u})f_\sigma\mathrm{d}\boldsymbol{v}\\ &= m_\sigma\int(\boldsymbol{v}-\boldsymbol{u}_\sigma+\boldsymbol{u}_\sigma-\boldsymbol{u})(\boldsymbol{v}-\boldsymbol{u}_\sigma+\boldsymbol{u}_\sigma-\boldsymbol{u})f_\sigma\mathrm{d}\boldsymbol{v}\\ &= m_\sigma\int(\boldsymbol{v}-\boldsymbol{u}_\sigma+\delta\boldsymbol{u}_\sigma)(\boldsymbol{v}-\boldsymbol{u}_\sigma+\delta\boldsymbol{u}_\sigma)f_\sigma\mathrm{d}\boldsymbol{v}\\ &= \mathbf{P}_\sigma+m_\sigma\int(2\delta\boldsymbol{u}_\sigma(\boldsymbol{v}-\boldsymbol{u}_\sigma)+\delta\boldsymbol{u}_\sigma\delta\boldsymbol{u}_\sigma)\,f_\sigma\mathrm{d}\boldsymbol{v}\\ \therefore\ \mathbf{P}^*_\sigma &= \mathbf{P}_\sigma+m_\sigma n_\sigma\delta\boldsymbol{u}_\sigma\delta\boldsymbol{u}_\sigma.\end{aligned}$$

Therefore,

$$\frac{\partial(\rho\boldsymbol{u})}{\partial t}+\nabla\cdot(\rho\boldsymbol{u}\boldsymbol{u})+\nabla\cdot\mathbf{P}^*=\sigma\boldsymbol{E}+\boldsymbol{j}\times\boldsymbol{B}.$$

Moreover,

$$\begin{aligned}
\frac{\partial(\rho \boldsymbol{u})}{\partial t} + \boldsymbol{u} \cdot \nabla(\rho \boldsymbol{u}) + 0 + \nabla \cdot \mathbf{P}^* &= \sigma \boldsymbol{E} + \boldsymbol{j} \times \boldsymbol{B} \\
\left(\frac{\partial}{\partial t} + \boldsymbol{u} \cdot \nabla \right)(\rho \boldsymbol{u}) + \nabla \cdot \mathbf{P}^* &= \sigma \boldsymbol{E} + \boldsymbol{j} \times \boldsymbol{B} \\
\frac{\mathrm{d}}{\mathrm{d}t}(\rho \boldsymbol{u}) + \nabla \cdot \mathbf{P}^* &= \sigma \boldsymbol{E} + \boldsymbol{j} \times \boldsymbol{B}. \qquad (2.24)
\end{aligned}$$

Where,

$$\frac{\mathrm{d}}{\mathrm{d}t} = \frac{\partial}{\partial t} + \boldsymbol{u} \cdot \nabla \qquad (2.25)$$

is called convective derivative which is the temporal differentiation for the moving coordinate system.

2.7 MHD equation

Since the single-fluid equation is not closed-form equation, the several orderings and assumptions are required. In this section, the MHD model and ordering are introduced.

Firstly, the vertical fluid velocity is assumed to be same order as the drift velocity $\boldsymbol{E} \times \boldsymbol{B}$. Since this drift velocity is determined by the electric field and the magnetic field, it does not depend on mass and electric charge. Therefore, the ions and the electrons have same fluid velocity. Moreover, if the parallel fluid velocity is assumed to be also same order for the ions and electrons, they are locally at thermal equilibrium with each other. In this case, the viscosity and the thermal conductivity of plasmas become zero. Secondly, the positive charges are assumed to be same as the negative charges in the plasma. This assumption is called quasi-neutral condition. In the single-fluid model, the quasi-neutral condition means that the number density for the electrons is same as that for ions. In addition to that, since ion's mass is much larger than electron's mass, the inertial term of the electrons can be ignored and the mass velocity $\boldsymbol{u}$ equals to the ion's mass velocity $\boldsymbol{u}_\mathrm{i}$.

The motion equation for the electrons can be written as below,

$$\begin{aligned}
\boldsymbol{E} + \boldsymbol{u}_\mathrm{e} \times \boldsymbol{B} &= \frac{1}{ne}(-\nabla p_\mathrm{e} + \boldsymbol{F}_\sigma) \\
\boldsymbol{E} + \boldsymbol{u}_\mathrm{i} \times \boldsymbol{B} - \boldsymbol{j} \times \boldsymbol{B} &= \frac{1}{ne}(-\nabla p_\mathrm{e} + \boldsymbol{F}_\sigma) \\
\boldsymbol{E} + \boldsymbol{u} \times \boldsymbol{B} &= \frac{1}{ne}(\boldsymbol{j} \times \boldsymbol{B} - \nabla p_\mathrm{e} + \boldsymbol{F}_\sigma). \qquad (2.26)
\end{aligned}$$

Equation (2.26) is the generalized Ohm's law. The first and second term in the right hand side of Eq. (2.26) respectively show the Hall effect and the drift term. These values are

negligibly small when it is compared to the left hand side of Eq. (2.26). The third term in right hand side of Eq. (2.26) is the frictional force for the electrons. Since this force mainly depends on the electric residence, it can be written as below,

$$\mathbf{F_e} \sim en\eta \boldsymbol{j}.$$

By using these assumptions, the MHD equations can be written as below,

$$\left(\frac{\partial}{\partial t} + \boldsymbol{u}\cdot\nabla\right)\rho = -\rho\nabla\cdot\boldsymbol{u} \tag{2.27}$$

$$\rho\left(\frac{\partial}{\partial t} + \boldsymbol{u}\cdot\nabla\right)\boldsymbol{u} = -\nabla p + \boldsymbol{j}\times\boldsymbol{B} \tag{2.28}$$

$$\left(\frac{\partial}{\partial t} + \boldsymbol{u}\cdot\nabla\right)p + \gamma p\nabla\dot{\boldsymbol{u}} = (\gamma-1)\eta|\boldsymbol{j}|^2 \tag{2.29}$$

$$\frac{\partial \boldsymbol{B}}{\partial t} = -\nabla\times\boldsymbol{E} \tag{2.30}$$

$$\boldsymbol{E} + \boldsymbol{u}\times\boldsymbol{B} = \eta\boldsymbol{j} \tag{2.31}$$

$$\mu_0\boldsymbol{j} = \nabla\times\boldsymbol{B}. \tag{2.32}$$

If Eq. (2.31) and Eq. (2.32) are substituted into Eq. (2.30), the magnetic diffusive equation can be obtained,

$$\frac{\partial \boldsymbol{B}}{\partial t} = -\nabla\times(\boldsymbol{u}\times\boldsymbol{B}) + \frac{\eta}{\mu_0}\nabla^2\boldsymbol{B}. \tag{2.33}$$

The ratio between the first and the second term in the left hand side of Eq. (2.23) can be written as below,

$$\mathrm{Re} = \frac{\mu_0 UL}{\eta} \tag{2.34}$$

where L is the characteristic length, U is the characteristic velocity and Re is the magnetic Reynolds number. In the case of $\mathrm{Re} \gg 1$, the plasma resistance η can be ignored. In this case, the MHD model is called ideal MHD model.

2.8 MHD equilibrium equation

In the fusion reactors, the plasma should be confined successfully under the high pressure and high temperature. For this purpose, the force from the gradient of the plasma pressure and the Lorentz force must be in an equilibrium state for a long time. Therefore, the behavior of plasmas should be clarified in the MHD equilibrium state. If the plasma is

under the equilibrium state and the fluid velocity is negligibly small as compared to the thermal velocity, the MHD equilibrium equations can be written as below,

$$\nabla p = \boldsymbol{j} \times \boldsymbol{B} \tag{2.35}$$

$$\mu_0 \boldsymbol{j} = \nabla \times \boldsymbol{B} \tag{2.36}$$

$$\nabla \cdot \boldsymbol{B} = 0. \tag{2.37}$$

Chapter 3

Orbit of energetic ions

3.1 Guiding center motion

The ion orbits can be separated by the Larmor motion which quickly circles with the radius ρ and the guiding center motion which drifts slowly. If ρ is sufficiently smaller than the characteristic device length L, the motion of the charged particles can be approximated by the guiding center motion.

For example, the ratio of ρ for the alpha particles and L in an ITER plasma is approximately

$$\frac{\rho}{L} \sim 1.0 \times 10^{-2}.$$

In this case, the finite Larmor effect is negligibly small.

While, the guiding center orbit consists of the several kinds of the drift velocity, such as the $\boldsymbol{E} \times \boldsymbol{B}$ drift, the ∇B drift and the curvature drift. In the next section, these kinds of drift velocity are derived.

3.1.1 $\boldsymbol{E} \times \boldsymbol{B}$ drift

If the electric field $\boldsymbol{E}$ and the magnetic field $\boldsymbol{B}$ exist, the charged particles drifts across the magnetic field line. The motion equation of a charged particle is written as below,

$$m\frac{\mathrm{d}\boldsymbol{v}}{\mathrm{d}t} = e(\boldsymbol{E} + \boldsymbol{v} \times \boldsymbol{B}), \tag{3.1}$$

where m and e are the mass and electric charge, respectively. In the case of $\boldsymbol{v} \equiv \boldsymbol{u} + \boldsymbol{E} \times \boldsymbol{B}/B^2$, the motion equation can be written as below,

$$\begin{aligned} m\frac{\mathrm{d}\boldsymbol{u}}{\mathrm{d}t} &= e(\boldsymbol{E}_{\parallel} + \boldsymbol{u} \times \boldsymbol{B}) \\ \boldsymbol{u} &\equiv \boldsymbol{v} - \boldsymbol{u}_E \\ \boldsymbol{u}_E &= \frac{\boldsymbol{E} \times \boldsymbol{B}}{B^2}. \end{aligned}$$

Since $\boldsymbol{E} \times \boldsymbol{B}$ drift only depends on the electromagnetic field, it is same for all particles.

3.1.2 ∇B drift

If the magnetic field has gradient, the charged particles drift in the vertical direction of ∇B since the Larmor radius is large on the strong $|B|$ area and small on the weak $|B|$ area. If there is no electric field and the magnetic field satisfies $\boldsymbol{B} = B(x)\boldsymbol{e}_z$, the orbit of a particle can be written as below,

$$\boldsymbol{r} \equiv \boldsymbol{x}_{\mathrm{g}} + \boldsymbol{\rho} \tag{3.2}$$

where $\boldsymbol{\rho}$ is the orbit of Larmaor motion and $\boldsymbol{x}_{\mathrm{g}}$ is the guiding center orbit. If the Larmor radius is sufficiently smaller than the characteristic length of the guiding center orbit, the magnetic field can be written as below,

$$B \simeq B\left[1 + \frac{\partial B(\boldsymbol{x}_{\mathrm{g}})}{\partial \boldsymbol{x}_{\mathrm{g}}}(\boldsymbol{x} - \boldsymbol{x}_{\mathrm{g}})\right]. \tag{3.3}$$

Therefore, the motion equation of an electron can be written as below,

$$\begin{aligned} \frac{\mathrm{d}v_x}{\mathrm{d}t} &\simeq w_c(x_{\mathrm{g}})\left[1 + \frac{\partial B(x_{\mathrm{g}})}{\partial x_{\mathrm{g}}}(x - x_{\mathrm{g}})\right] v_y \\ \frac{\mathrm{d}v_y}{\mathrm{d}t} &\simeq -w_c(x_{\mathrm{g}})\left[1 + \frac{\partial B(x_{\mathrm{g}})}{\partial x_{\mathrm{g}}}(x - x_{\mathrm{g}})\right] v_x. \end{aligned} \tag{3.4}$$

The first order of the motion equation in the x direction can be written as below,

$$\begin{aligned} \frac{\mathrm{d}v_{x1}}{\mathrm{d}t} - w_c v_{y1} &= -\frac{w_c(x_{\mathrm{g}})}{\mathrm{b}}\left[\frac{\partial B}{\partial x_{\mathrm{g}}}\rho\cos(w_c t)v_\perp \sin(w_c t)\right] \\ &= -\frac{v_\perp^2}{2B}\frac{\partial B}{\partial x_{\mathrm{g}}}\left[1 - \cos(2w_c t)\right]. \end{aligned} \tag{3.5}$$

Likewise, the first order of the motion equation in the y direction can be written as below,

$$\frac{\mathrm{d}v_{y1}}{\mathrm{d}t} - w_c v_{x1} = -\frac{v_\perp^2}{2B}\frac{\partial B}{\partial x_{\mathrm{g}}}\sin(2w_c t). \tag{3.6}$$

If these motion equations are averaged in the Larmor cycle, these equations can be written as below,

$$\begin{aligned} \frac{\mathrm{d}v_{x1}}{\mathrm{d}t} - w_c v_{y1} &= -\frac{v_\perp^2}{2B}\frac{\partial B}{\partial x_{\mathrm{g}}} \\ \frac{\mathrm{d}v_{x1}}{\mathrm{d}t} - w_c v_{y1} &= 0. \end{aligned}$$

Since the $\boldsymbol{F}_{\nabla B}$ corresponds with $e\boldsymbol{E}$ in $\boldsymbol{E} \times \boldsymbol{B}$, the ∇B drift can be written as below,

$$\boldsymbol{v}_{\nabla B} = -\frac{mv_\perp^2}{2eB}\frac{1}{\mathrm{b}}\frac{\partial B}{\partial x_\mathrm{g}}\boldsymbol{e}_y.$$

By generalizing this section, the ∇B drift can be written as,

$$\boldsymbol{v}_{\nabla B} = \frac{mv_\perp^2}{2eB}\frac{\boldsymbol{B} \times \nabla B}{B^2}. \tag{3.7}$$

3.1.3 Curvature drift

If the magnetic field strength has the curvature, the particles are affected by the centrifugal force,

$$\boldsymbol{F} = \frac{mv_\parallel^2}{R_c}\boldsymbol{B}.$$

The drift velocity from the centrifugal force can be written as below,

$$\boldsymbol{v}_\mathrm{d} = \frac{mv_\parallel^2}{eB^2}\frac{\boldsymbol{B} \times \boldsymbol{b}}{R_c}. \tag{3.8}$$

By using the equation:

$$\boldsymbol{B} \times (\nabla \times \boldsymbol{B}) \;=\; B\nabla B - (\boldsymbol{B} \cdot \nabla)\boldsymbol{B},$$

the gradient of the magnetic field strength can be written as below,

$$\begin{aligned}
\nabla B &= (\boldsymbol{b} \cdot \nabla)\mathbf{B} + \mathbf{b} \times (\nabla \times \mathbf{B}) \\
&= \frac{\partial B}{\partial l}\boldsymbol{b} + B\frac{\partial \boldsymbol{b}}{\partial l} + \boldsymbol{b} \times (\nabla \times \boldsymbol{B}) \\
&= \frac{\partial B}{\partial l}\boldsymbol{b} - B\frac{\boldsymbol{B}}{R_c} + \boldsymbol{b} \times (\nabla \times \boldsymbol{B}).
\end{aligned}$$

The cross product of the above equations and $\boldsymbol{B}$ can be written as below,

$$\begin{aligned}
\frac{\boldsymbol{B} \times \boldsymbol{b}}{R_c} &= \frac{1}{\mathrm{b}}\boldsymbol{B} \times \nabla B + \{\boldsymbol{b} \times (\nabla \times \boldsymbol{B})\} \times \boldsymbol{b} \\
&= \frac{1}{\mathrm{b}}\boldsymbol{B} \times \nabla B + (\nabla \times \boldsymbol{B}) - (\boldsymbol{b} \cdot (\nabla \times \boldsymbol{B}))\boldsymbol{b} \\
&= \frac{1}{\mathrm{b}}\boldsymbol{B} \times \nabla B + (\nabla \times \boldsymbol{B})_\perp.
\end{aligned}$$

Therefore, the curvature drift can be written as below,

$$\boldsymbol{v}_\mathrm{d} = \frac{mv_\parallel^2}{eB^3}\boldsymbol{b} \times \nabla B + \frac{mv_\parallel^2}{eB^2}(\nabla \times \boldsymbol{B})_\perp. \tag{3.9}$$

3.1.4 Summary of guiding center drift

The guiding center drift can be summarized as,

$$\boldsymbol{v}_{\mathrm{d}} = \frac{\boldsymbol{E}\times\boldsymbol{B}}{B^2} + \frac{mv_{\parallel}^2 + mv_{\perp}^2/2}{eB^3}(\boldsymbol{B}\times\nabla B) + \frac{mv_{\parallel}^2}{eB^2}(\nabla\times\boldsymbol{B})_{\perp}. \tag{3.10}$$

The magnetic momentum μ and the whole energy W can be written as below,

$$\mu = \frac{mv_{\perp}^2}{2B} \tag{3.11}$$

$$W = e\phi + \frac{m}{2}(v_{\parallel}^2 + v_{\perp}^2), \tag{3.12}$$

where ϕ is the electrostatic potential. Therefore, the guiding center drift can be written as below,

$$\begin{aligned}\boldsymbol{v}_{\mathrm{d}} &= \frac{\boldsymbol{b}\times\nabla\phi}{\mathrm{b}} + \frac{1}{eB}\left(\frac{mv_{\parallel}^2}{\mathrm{b}} + \mu\right)\boldsymbol{b}\times\nabla B + \frac{mv_{\parallel}^2}{eB^2}(\nabla\times\boldsymbol{B})_{\perp} \\ &= \frac{1}{eB}\boldsymbol{b}\times\left\{\nabla(e\phi + B\mu) + \frac{mv_{\parallel}^2}{\mathrm{b}}\nabla B\right\} + \frac{mv_{\parallel}^2}{eB^2}(\nabla\times\boldsymbol{B})_{\perp}.\end{aligned}$$

Moreover, by Eq. (3.12),

$$\nabla\left(\frac{1}{2}mv_{\parallel}^2\right) = \nabla\left(W - e\phi - \mu B\right).$$

If the whole energy and the magnetic moment are conserved, the velocity can be assumed to be the function of the position of the particles,

$$mv_{\parallel}\nabla v_{\parallel} = -\nabla\left(e\phi + \mu B\right).$$

By using this equation, the guiding center drift can be written as below,

$$\boldsymbol{v}_{\mathrm{d}} = \frac{mv_{\parallel}}{eB^2}\left\{-B\boldsymbol{b}\times\nabla v_{\parallel} + \mathrm{v}_{\parallel}\boldsymbol{b}\times\nabla B + v_{\parallel}(\nabla\times\boldsymbol{B})_{\perp}\right\}$$

Since

$$\begin{aligned}\nabla\times\left(\frac{v_{\parallel}\boldsymbol{B}}{\mathrm{b}}\right) &= \frac{v_{\parallel}}{\mathrm{b}}\nabla\times\boldsymbol{B} + \frac{1}{\mathrm{b}}\nabla v_{\parallel}\times\boldsymbol{B} - \frac{v_{\parallel}}{B^2}\nabla B\times\boldsymbol{B} \\ &= \frac{1}{\mathrm{b}}\left(-B\boldsymbol{b}\times\nabla v_{\parallel} + \mathrm{v}_{\parallel}\boldsymbol{b}\times\nabla\mathrm{B} + v_{\parallel}\nabla\times\boldsymbol{B}\right),\end{aligned}$$

the drift velocity of the guiding center orbit can be written as below [15],

$$\begin{aligned}\boldsymbol{v}_{\mathrm{d}} &= \frac{mv_{\parallel}}{eB}\nabla\times\left(\frac{v_{\parallel}\boldsymbol{b}}{\mathrm{b}}\right) \\ &= \frac{e\rho_{\parallel}}{m}\nabla\times\left(\rho_{\parallel}\boldsymbol{b}\right) \qquad (3.13)\\ \rho_{\parallel} &\equiv \frac{mv_{\parallel}}{eB}. \qquad (3.14)\end{aligned}$$

3.1.5 Parallel velocity of guiding center motion

In the previous discussion, the Larmor radius was assumed to be the zeroth order. However, since the distribution function might be moved from the normal distribution due to the Larmor motion, it should be modified to satisfy the drift kinetic theory. In the ideal drift kinetic theory, since the number of the particles is conserved, the divergence of the number flux becomes zero,

$$\nabla \cdot \left(\int \boldsymbol{v}_{\mathrm{d}} f \mathrm{d}\boldsymbol{v} \right) = 0. \tag{3.15}$$

The volume element in the velocity coordinates can be written as below,

$$\mathrm{d}\boldsymbol{v} = J \mathrm{d}W \mathrm{d}\mu \mathrm{d}\phi, \tag{3.16}$$

where W is the whole energy, μ is the magnetic moment and ϕ is the phase in the Larmor motion. Since the drift velocity does not depend on the phase of the Larmor motion, this equation can be written as below,

$$\mathrm{d}\boldsymbol{v} = 2\pi \langle J \rangle \, \mathrm{d}W \mathrm{d}\mu,$$

where, $\langle J \rangle$ is the averaged Jacobian in the Larmor phase. Since Eq. (3.15) is valid in any W and μ conditions, $\boldsymbol{v}_{\mathrm{d}}$ has to be modified to satisfy the below condition,

$$\nabla \cdot (\langle J \rangle \, \boldsymbol{v}_{\mathrm{d}}) = 0. \tag{3.17}$$

If the averaged Jacobian is the first order of the Larmor motion, $\langle J \rangle$ should satisfy the below condition [16],

$$\langle J \rangle = \frac{\mathrm{b}}{m^2 v_{\parallel}} \left(1 + \rho_{\parallel} \boldsymbol{b} \cdot \nabla \times \boldsymbol{b} \right). \tag{3.18}$$

In this case, the guiding center orbit can be written as below,

$$\boldsymbol{v}_{\mathrm{g}} = \frac{v_{\parallel}}{\mathrm{b}} \frac{1}{1 + \rho_{\parallel} \boldsymbol{b} \cdot \nabla \times \boldsymbol{b}} \left[\boldsymbol{b} + \nabla \times \left(\rho_{\parallel} \boldsymbol{b} \right) \right]. \tag{3.19}$$

3.2 Orbit of charted particles in rippled tokamaks

If these is no electric field, the parallel velocity can be written as below,

$$v_{\parallel} \;=\; \pm \sqrt{\frac{2}{m}(W - \mu B)}. \tag{3.20}$$

If the whole energy and the magnetic momentum are conserved, $v_{\parallel}$ becomes smaller with increasing the magnetic field strength B and finally it becomes zero. In this case, the

particles are trapped by the magnetic field. The conditions to become trapped particles are shown below,

$$\begin{aligned} 0 &> W - \mu B \\ 0 &> \frac{1}{2}mv_0^2 - \frac{mv_{\perp,0}^2}{2B_0}B \\ \left(\frac{v_{\perp,0}}{v_0}\right)^2 &> \frac{B_0}{\mathrm{b}} \end{aligned}$$

If the magnetic field strength is described as below,

$$B = B_0(1+\delta B), \quad \frac{v_{\perp,0}}{v_0} = \sin\lambda,$$

this condition can be modified as,

$$\sin^2\lambda > 1 - \delta B. \tag{3.21}$$

This equation means that the conditions to become trapped particles depends on the pitch angle and δB.

In the rippled tokamaks, there are two types of δB; the first is the difference due to the toroidal effect δB_1 and the second is the difference due to the toroidal field (TF) ripples δB_2. Generally δB_1 is much larger than δB_2.

3.2.1 Passing particles

If the particles satisfy $0 \leq \sin^2\lambda < 1 - \delta B_1$, they cycle in the torus direction. Since it takes $\tau = 2\pi R_0/v_\parallel$ to cycle in the torus direction, the particles cycle in the poloidal direction with the angular velocity w,

$$w = \frac{\iota}{\tau} = \frac{\iota v_\parallel}{2\pi R_0}, \tag{3.22}$$

where ι is the rotational transform. In the tokamak plasmas, because $\boldsymbol{B}$ is the torus direction and ∇B is the radius direction, the drift velocity is the vertical direction. Therefore, the motion equations of the guiding center orbit can be written as below,

$$\begin{aligned} \frac{\mathrm{d}X}{\mathrm{d}t} &= -wZ \\ \frac{\mathrm{d}Z}{\mathrm{d}t} &= wX + v_\mathrm{d} \end{aligned}$$

where X is $R - R_0$. Solution of these equations can be shown below,

$$\left(X + \frac{v_\mathrm{d}}{w}\right)^2 + Z^2 = r^2. \tag{3.23}$$

Equation (3.23) means that the orbit surface moves from the magnetic surface by v_d/w in the radius direction.

3.2.2 Banana particles

In the case of $1 - \delta B_1 \leq \sin^2 \lambda < 1 - \delta B_2$, the particles are trapped in the weak magnetic field at the outer torus. If the toroidal field is much stronger than the poloidal field, the magnetic field strength can be written as below,

$$B = \frac{B_0 R_0}{R} = \frac{B_0}{1 + (r/R)\cos\theta} \approx B_0 \left(1 - \frac{r}{R_0}\cos\theta\right). \tag{3.24}$$

In the case of $v_\perp \gg v_\parallel$, r component of the drift velocity can be written as below,

$$\frac{\mathrm{d}r}{\mathrm{d}t} = v_\mathrm{d} \sin\theta = \frac{m}{eB_0}\frac{v_\perp^2}{2R}\sin\theta. \tag{3.25}$$

On the other hand, the parallel component of the motion equation can be written as below,

$$\frac{\mathrm{d}v_\parallel}{\mathrm{d}t} = -\frac{v_\perp^2}{2B_0}\frac{\partial B}{\partial l} = \frac{v_\perp^2}{2B_0}\frac{B_0 r}{R_0}\sin\theta\frac{\partial\theta}{\partial l} = -\frac{v_\perp^2}{2R_0}\frac{B_\mathrm{p}}{B_0}\sin\theta. \tag{3.26}$$

Therefore, the particles cyclically move along the magnetic field line,

$$\begin{aligned} \frac{\mathrm{d}}{\mathrm{d}t}\left(r + \frac{m}{eB_\mathrm{p}}v_\parallel\right) &= 0 \\ r - r_0 = -\frac{m}{eB_\mathrm{p}}v_\parallel. \end{aligned} \tag{3.27}$$

Since the guiding center orbits of these particles seem to be banana shape, they are called banana particles.

In a high-beta plasma, the strong poloidal field is required in the outboard side of the torus to maintain the safety-factor on the plasma surface. Since the banana width is inversely proportional to the field strength, the banana width is squeezed [17]. Due to this orbit squeezing effect, the banana-orbit losses such as the first-orbit losses may be reduced. Especially in the spherical tokamaks, this effect is much stronger than that for the usual tokamaks because the poloidal field is comparable to the toroidal field at the outer torus. In this case, the valley of the field strength may appear in the radius direction. As the results, the several unique orbits can be seen.

3.2.3 Toroidal precession

The banana particles precess in the toroidal direction during the repetitive banana orbits. If the Taylor-expansion is used for the safety-factor q around the banana tip $(r_\mathrm{b}, \theta_\mathrm{b}, \zeta_\mathrm{b})$, it can be written as below,

$$q = q_\mathrm{b} + \frac{\mathrm{d}q}{\mathrm{d}r}(r - r_\mathrm{b}).$$

By using Eq. (3.27),

$$q = q_{\rm b} - \frac{mv_{\parallel}}{eB_{\rm p}}\frac{{\rm d}q}{{\rm d}r}. \tag{3.28}$$

The parallel component of the particle velocity can be written as below,

$$v_{\parallel} = \pm\sqrt{em}\left(W - \mu B_0(1-\epsilon\cos\theta)\right)^{1/2}$$

Since the parallel component of the velocity becomes zero at the banana tip,

$$W = \mu B_0(1-\cos\theta_{\rm b}). \tag{3.29}$$

Therefore,

$$v_{\parallel} = \pm\sqrt{em\mu\epsilon B_0}\left(\cos\theta - \cos\theta_{\rm b}\right)^{1/2}.$$

The toroidal angle is changed during the half bounce of the banana orbit,

$$\begin{aligned}
\phi &= \phi_0 + \int_{\mp\theta_{\rm b}}^{\pm\theta_{\rm b}} \left[q \pm \frac{m}{eB_{\rm p}}\frac{{\rm d}q}{{\rm d}r}\sqrt{em\mu\epsilon B_0}\left(\cos\theta - \cos\theta_{\rm b}\right)^{1/2}\right]{\rm d}\theta \\
&= \phi_0 \pm q\theta_{\rm b} \pm \frac{m}{eB_{\rm p}}\frac{{\rm d}q}{{\rm d}r}\sqrt{em\mu\epsilon B_0}\int_{\mp\theta_{\rm b}}^{\pm\theta_{\rm b}}\left[\left(\cos\theta - \cos\theta_{\rm b}\right)^{1/2}\right]{\rm d}\theta \\
&= \phi_0 \pm q\theta_{\rm b} + \frac{16m}{e}\frac{{\rm d}q}{{\rm d}r}\sqrt{\frac{em\mu\epsilon}{B_0}}\left[E(\Theta) + (\Theta^2-1)K(\Theta)\right] \\
\therefore\ \phi &= \phi_0 \pm q\theta_{\rm b} + \phi_{\rm p},
\end{aligned}$$

where, Θ equals to $\sin(\theta_{\rm b}/2)$, and $E(\Theta)$ and $K(\Theta)$ are respectively complete elliptic integrals which are defined by

$$K(\Theta) = \int_0^{\pi/2}\frac{{\rm d}\Theta}{(1-\Theta^2\sin^2\Theta)^{1/2}} \tag{3.30}$$

$$E(\Theta) = \int_0^{\pi/2}(1-\Theta^2\sin^2\Theta)^{1/2}{\rm d}\Theta. \tag{3.31}$$

If the initial toroidal angle ϕ_0 is zero, the toroidal angle is changed during one bounce of the banana orbit,

$$\Delta\phi = 2\phi_{\rm p}. \tag{3.32}$$

3.2.4 Banana drift

The canonical angular momentum of the guiding center orbit can be written as below,

$$P_\phi = mRv_\parallel + e\Psi = \text{const.} \tag{3.33}$$

Therefore, the deviation of P_ϕ about the poloidal angle is,

$$\begin{aligned} \frac{\mathrm{d}P_\phi}{\mathrm{d}\theta} = mR\frac{\partial v_\parallel}{\partial \theta} + e\frac{\partial \Psi}{\partial \theta} &= 0 \\ \therefore \quad \frac{\partial \Psi}{\partial \theta} &= -\frac{mR}{e}\frac{\partial v_\parallel}{\partial \theta}. \end{aligned}$$

Whereas, the parallel component of the particle velocity in the non-axisymmetric field can be written as below,

$$v_\parallel = \pm\sqrt{em}\,(W - \mu B_\theta(1 + \delta\cos N\phi))^{1/2}$$

where N is the number of the toroidal field coils. Therefore,

$$\frac{\partial \Psi}{\partial \theta} = \pm\frac{R}{ev_\parallel}\frac{\partial B_\theta}{\partial \theta}. \tag{3.34}$$

The difference of the poloidal magnetic flux Ψ between for the axisymmetric and the non-axissymetric field can be written as below,

$$\frac{\partial \Delta\Psi}{\partial \theta} = \mp\frac{R}{e}\frac{\partial B_\theta}{\partial \theta}\left(\frac{v_\parallel(0) - v_\parallel(\delta)}{v_\parallel(\delta)v_\parallel(0)}\right) \tag{3.35}$$

While, the parallel component of the particle velocity can be derived as below,

$$\begin{aligned} v_\parallel &= \sqrt{\frac{2W}{m}}\left[1 - \frac{B_\theta}{B_{\theta_\mathrm{b}}}\{1 + \delta\cos N\phi_\mathrm{b} + \delta(\cos N\phi - \cos N\phi_\mathrm{b})\}\right]^{1/2} \\ &= \sqrt{\frac{2W}{m}}\left[1 - \frac{B_\theta}{B_{\theta_\mathrm{b}}}(1 + \delta\cos N\phi_\mathrm{b})\right]^{1/2} \\ &\times \quad \left[1 - \frac{\mu\delta(\cos N\phi - \cos N\phi_\mathrm{b})}{2W\{1 - (B_\theta/B_{\theta_\mathrm{b}})(1 + \delta\cos N\phi_\mathrm{b})\}}\right] \end{aligned} \tag{3.36}$$

If the non-axisymmetry of the magnetic field is not so effective, this equation can be approximated as below,

$$\begin{aligned} v_\parallel &= \sqrt{\frac{2W}{m}}\left[1 - \frac{B_\theta}{B_{\theta_\mathrm{b}}}\right]^{1/2}\left[1 - \frac{\delta(\cos N\phi - \cos N\phi_\mathrm{b})}{2B_{\theta_\mathrm{b}}\{1 - (B_\theta/B_{\theta_\mathrm{b}})\}}\right] \\ &= v_\parallel(0)\left[1 - \frac{\delta(\cos N\phi - \cos N\phi_\mathrm{b})}{2B_{\theta_\mathrm{b}}\{1 - (B_\theta/B_{\theta_\mathrm{b}})\}}\right]. \end{aligned} \tag{3.37}$$

Therefore,

$$v_\parallel(0) - v_\parallel(\delta) = -\frac{v_\parallel(0)\delta(\cos N\phi - \cos N\phi_\mathrm{b})}{2B_{\theta_\mathrm{b}}\{1-(B_\theta/B_{\theta_\mathrm{b}})\}}.$$

By substituting this equation into Eq. (3.35),

$$\begin{aligned}\frac{\partial\Delta\Psi}{\partial\theta} &= \pm\frac{R}{e}\frac{\partial B_\theta}{\partial\theta}\left(\frac{v_\parallel(0)-v_\parallel(\delta)}{v_\parallel(\delta)v_\parallel(0)}\right)\\ &= \pm\frac{R\delta}{2e}\frac{\partial B_\theta/\partial\theta}{B_{\theta_\mathrm{b}}}\frac{1}{v_\parallel}\frac{\cos N\phi-\cos N\phi_\mathrm{b}}{1-(B_\theta/B_{\theta_\mathrm{b}})}\\ &= \pm\frac{R\delta}{2e\sqrt{emW}}\frac{\partial B_\theta/\partial\theta}{B_{\theta_\mathrm{b}}}\frac{\cos N\phi-\cos N\phi_\mathrm{b}}{\{1-(B_\theta/B_{\theta_\mathrm{b}})\}^{3/2}}. \end{aligned} \tag{3.38}$$

By using the Taylor-expansion around the banana tip for B_θ and $\cos N\phi$,

$$B_\theta = B_{\theta_\mathrm{b}} + \frac{\partial B_\theta}{\partial\theta}(\theta-\theta_\mathrm{b}) \tag{3.39}$$

$$\cos N\phi = \cos N\phi_\mathrm{b} - N\sin N\phi_\mathrm{b}(\phi-\phi_\mathrm{b}). \tag{3.40}$$

By substituting these equations into Eq. (3.38),

$$\frac{\partial\Delta\Psi}{\partial\theta} = \pm\frac{RNq\delta\sin N\phi_\mathrm{b}}{2e\sqrt{emW}}\left(\frac{\partial B_\theta/\partial\theta}{B_{\theta_\mathrm{b}}}\right)^{-1/2}_{\theta=\theta_\mathrm{b}}(\theta-\theta_\mathrm{b})^{-1/2}. \tag{3.41}$$

Therefore, the changes of Ψ for the one-quarter banana orbit can be described as below,

$$\begin{aligned}\Delta\Psi &= \int_0^{\theta_\mathrm{b}}\frac{\partial\Delta\Psi}{\partial\theta}\mathrm{d}\theta\\ &= \frac{RNq\delta}{e}\sqrt{\frac{\theta_\mathrm{b}}{emW}}\left(\frac{\partial B_\theta/\partial\theta}{B_{\theta_\mathrm{b}}}\right)^{-1/2}_{\theta=\theta_\mathrm{b}}\sin N\phi_\mathrm{b}.\end{aligned}$$

Therefore, this equation for the one-bounce banana orbit can be described as,

$$\begin{aligned}\Delta\Psi &= \frac{4RNq\delta}{e}\sqrt{\frac{\theta_\mathrm{b}}{emW}}\left(\frac{\partial B_\theta/\partial\theta}{B_{\theta_\mathrm{b}}}\right)^{-1/2}_{\theta=\theta_\mathrm{b}}\sin N\phi_\mathrm{b}\\ &= \Delta_\mathrm{b}\sin N\phi_\mathrm{b}.\end{aligned} \tag{3.42}$$

3.2.5 Ripple resonance

As shown in the previous section, the radial displacement depends on the toroidal angle of the reflection point,

$$\begin{aligned}\Delta\Psi &= \Delta_{\mathrm{b}} \sin N\phi_{\mathrm{b}} \\ \Delta_{\mathrm{b}} &= \frac{4RNq\delta}{e}\sqrt{\frac{\theta_{\mathrm{b}}}{emW}}\left(\frac{\partial B_\theta/\partial\theta}{B_{\theta_{\mathrm{b}}}}\right)^{-1/2}_{\theta=\theta_{\mathrm{b}}} \\ \phi_{\mathrm{p}} &= \frac{16m}{e}\frac{\mathrm{d}q}{\mathrm{d}r}\sqrt{\frac{em\mu\epsilon}{B_0}}\left[E(\Theta)+(\Theta^2-1)K(\Theta)\right].\end{aligned}$$

Therefore, if the banana particles satisfy the below condition,

$$2N\phi_{\mathrm{p}} = 2k\pi \qquad (k = 0, \pm1, \pm2, ...), \tag{3.43}$$

they always have the same displacement and the energetic ion losses might be increased.

3.2.6 Deeply ripple-trapped orbit

In the case of $1 - \delta B_2 \leq \sin^2\lambda \leq 1$, the particles are trapped by the TF ripples. These particles drift along the minimum magnetic field $B_{\min}$ contour [18]. $B_{\min}$ is the minimum value of the field strength with respect to the toroidal angle (i.e., the field strength between TFCs).

For example, if particles are trapped in the bottom of the TF ripples, $v_\parallel$ always equals to zero,

$$\frac{mv_\parallel^2}{2} = W - \mu B = 0.$$

Therefore,

$$\begin{aligned}\frac{mv^2}{2} &= \frac{m}{2}\frac{v_{\perp,0}^2}{B_{\min}}B \\ &= \frac{m}{2}\frac{v_0^2}{B_{\min}}B \\ \therefore\ B &= B_{\min}.\end{aligned} \tag{3.44}$$

In this case, the particles could not escape from the minimum magnetic field contour. Therefore, the deeply ripple-trapped particles move along $B_{\min}$ contour line.

3.3 Boozer coordinates

Due to the $\nabla \cdot \boldsymbol{B} = 0$, the magnetic field can be written by the several scalar functions as below [19],

$$\boldsymbol{B} = \nabla\psi \times \nabla\alpha. \tag{3.45}$$

Since

$$\boldsymbol{B} \cdot \nabla\psi = 0,$$

the magnetic flux surfaces ψ correspond to the magnetic surfaces. Therefore, if ψ is chosen as one component of the flux coordinates, B^ψ becomes zero. If the poloidal angle θ and toroidal angle ζ are chosen as other components of the flux coordinates, $\nabla\alpha$ also has periodicity. Therefore,

$$\begin{aligned} \nabla\alpha &= \tilde{A}(\psi,\theta,\zeta) \\ \therefore\ \alpha &= \mathrm{m}(\psi)\theta + \mathrm{n}(\psi)\zeta + \tilde{\alpha}(\psi,\theta,\zeta). \end{aligned}$$

In the case of $\mathrm{m} = 1$, $\mathrm{n} = -\iota(\psi)$ and $\tilde{\alpha} = 0$, α show the label for the magnetic field line.

$$\alpha = \theta - \iota(\psi)\zeta \tag{3.46}$$

By Eq. (3.46), the magnetic field can be modified as below,

$$\begin{aligned} \boldsymbol{B} &= \nabla\psi \times \nabla(\theta - \iota(\psi)\zeta) \\ &= \nabla\psi \times \nabla\theta + \iota(\psi)\nabla\zeta \times \nabla\psi. \end{aligned} \tag{3.47}$$

In this case, the contravariant component of the magnetic field can be written as below,

$$\begin{aligned} B^\psi &= 0 \\ B^\theta &= \frac{\iota}{\sqrt{\mathrm{g}}} \\ B^\zeta &= \frac{1}{\sqrt{\mathrm{g}}}, \end{aligned} \tag{3.48}$$

where $\sqrt{\mathrm{g}}$ is the Jacobian in the Boozer coordinates. Moreover, the toroidal flux Φ_{tor} can be written as below,

$$\Phi_{\mathrm{tor}} = \int \boldsymbol{B} \cdot \sqrt{\mathrm{g}}\mathrm{d}\mathbf{S}_{\mathrm{tor}} = \int \sqrt{\mathrm{g}}\boldsymbol{B} \cdot \nabla\zeta \mathrm{d}\theta\psi = 2\pi\psi, \tag{3.49}$$

where ψ is the toroidal flux which is divided by 2π.

Next, the covariant components of the magnetic field are derived. Since the divergence of the current density $\boldsymbol{j}$ is zero,

$$\begin{aligned} \boldsymbol{j} &= \frac{1}{\mu}\left\{\nabla\psi \times \nabla(I'(\psi)\theta + G'(\psi)\zeta - \tilde{\nu}(\psi,\theta,\zeta)\right\} \\ &= \frac{1}{\mu}\left(I'\nabla\psi\times\nabla\theta - G'\nabla\zeta\times\nabla\psi - \nabla\psi\times\nabla\tilde{\nu}\right), \end{aligned} \tag{3.50}$$

where $'$ shows the differentiation about ψ. According to the definitions of the toroidal current $I_{\rm tor}$ and the poloidal current $I_{\rm pol}$,

$$I_{\rm tor} = \int \boldsymbol{j}\cdot\nabla\zeta\sqrt{g}\mathrm{d}\theta\mathrm{d}\psi = 2\pi I(\psi) \tag{3.51}$$

$$I_{\rm pol} = \int \boldsymbol{j}\cdot\nabla\theta\sqrt{g}\mathrm{d}\zeta\mathrm{d}\psi = 2\pi G(\psi), \tag{3.52}$$

where I and G respectively show the toroidal current and the poloidal current divided by 2π. Due to the Ampere's law, the current density can be written as below,

$$\begin{aligned} \mu_0\boldsymbol{j} &= \nabla\times\boldsymbol{B} \\ &= \left(\frac{\partial B_\zeta}{\partial\theta} - \frac{\partial B_\theta}{\partial\zeta}\right)\nabla\theta\times\nabla\zeta + \left(\frac{\partial B_\psi}{\partial\zeta} - \frac{\partial B_\zeta}{\partial\psi}\right)\nabla\zeta\times\nabla\psi \\ &+ \left(\frac{\partial B_\theta}{\partial\psi} - \frac{\partial B_\psi}{\partial\theta}\right)\nabla\psi\times\nabla\theta. \end{aligned} \tag{3.53}$$

By substituting Eq. (3.50) into this equation,

$$\begin{aligned} \frac{\partial B_\zeta}{\partial\theta} - \frac{\partial B_\theta}{\partial\zeta} &= 0 \\ \frac{\partial B_\psi}{\partial\zeta} - \frac{\partial B_\zeta}{\partial\psi} &= -G' + \frac{\partial\tilde{\nu}}{\partial\zeta} \\ \frac{\partial B_\theta}{\partial\psi} - \frac{\partial B_\psi}{\partial\theta} &= I' - \frac{\partial\tilde{\nu}}{\partial\theta}. \end{aligned} \tag{3.54}$$

Therefore, the covariant components of the magnetic field can be written with the scalar function η,

$$\boldsymbol{B} = \tilde{\nu}\nabla\psi + I\nabla\theta + G\nabla\zeta + \nabla\eta. \tag{3.55}$$

Since η equals to zero in the Boozer coordinates, the covariant components can be written as below,

$$\begin{aligned} B_\psi &= \tilde{\nu} \\ B_\theta &= I \\ B_\zeta &= G. \end{aligned} \tag{3.56}$$

By summarizing this section, the contravariant and the covariant component can be written as below,

$$\boldsymbol{B} = \nabla\psi \times \nabla\theta + \iota(\psi)\nabla\zeta \times \nabla\psi = \tilde{\nu}\nabla\psi + I\nabla\theta + G\nabla\zeta. \tag{3.57}$$

The Jacobian $\sqrt{\mathrm{g}}$ can be written as below,

$$\begin{aligned} B^2 &= (G + \tau I)(\nabla\psi \times \nabla\theta) \cdot \nabla\zeta \\ \therefore\ \sqrt{\mathrm{g}} &= \frac{G + \tau I}{B^2}. \end{aligned} \tag{3.58}$$

In this case, the Jacobian is inversely proportional to the square of the magnetic field strength.

Chapter 4

Study of the mechanism of finite beta effects on the MHD equilibria and the energetic ion losses

The efficiency of the energetic ion confinement is reduced by the ripple fields, which are mainly generated by the finite number of toroidal field coils (TFCs) in a tokamak reactor. The finite beta effects alter the magnetic field structures and the energetic ion orbits. To evaluate these effects, the MHD equilibrium is calculated using the VMEC code in an ITER-like plasma and the orbits of energetic ions are calculated using the GCB code. The finite beta effects on the ripple ratio are categorized by two parts: the axisymmetric and the non-axisymmetric finite beta effects. In the center of a plasma, both effects increase the ripple ratio. While, the axisymmetric finite beta effect decreases the ripple ratio at the outer torus. The decrease of the ripple ratio by the axisymmetric finite beta effect is larger than the increase of it by the non-axisymmetric finite beta effect. Therefore, the finite beta effects increase the ripple ratio in the center of a plasma and decrease it at the outer torus. The diamagnetic effect reduces the field strength and alters the field contour structure. It significantly bends the field contour line in a high-beta plasma and produces two opposing effects: 1) the reduction of the energetic ion losses due to the closed field line contour and 2) the increase of these losses due to the field contour line bending effect. This paper was published in Nucl. Fusion 52 (2012) 083009 [20].

4.1 Introduction

The magnetic field structure, including the TF ripples, in tokamak plasmas can be calculated using two methods. The first method uses the two-dimensional (2D) MHD equilibrium, which can be obtained by solving the Grad-Shafranov equation. The approximated three-dimensional (3D) field structure can be obtained by superimposing the external TF

ripple components on the 2D MHD equilibrium field [21][6]. In this study, this approximation method is called vacuum approximation. The vacuum approximation does not include the non-axisymmetric field component caused by the equilibrium current, but includes the external TF ripples. The second method uses the full 3D MHD equilibrium including the effect of the non-axisymmetric component of the plasma. For example, the VMEC code which is based on the energy principle in the flux coordinates, can calculate such a 3D MHD equilibrium [10][11]. In this case, the non-axisymmetry of the plasma alters the TF ripples themselves [8][9]. If the 2D and 3D MHD equilibrium field are expressed by $\langle \boldsymbol{B} \rangle$ and $\boldsymbol{B_{3D}}$ respectively, the following equation can be obtained,

$$\boldsymbol{B_{3D}} \equiv \langle \boldsymbol{B} \rangle + \widetilde{\boldsymbol{B}} \equiv \langle \boldsymbol{B} \rangle + \widetilde{\boldsymbol{B}}^{\mathrm{ext}} + \widetilde{\boldsymbol{B}}^{\mathrm{pl}}, \tag{4.1}$$

where $\widetilde{\boldsymbol{B}}^{\mathrm{ext}}$ is the non-axisymmetric external field component generated by the external coil current (i.e., TFCs) and $\widetilde{\boldsymbol{B}}^{\mathrm{pl}}$ is the non-axisymmetric field component generated by the current in the plasma. The scale of this effect depends on the plasma beta and the engineering design of the device (e.g., the shape and number of TFCs). If $\widetilde{\boldsymbol{B}}^{\mathrm{pl}}$ is negligible, the vacuum approximation can be used instead of solving the 3D MHD equilibrium equation.

In an ITER operation, $\widetilde{\boldsymbol{B}}^{\mathrm{ext}}$ is not very large and the ripple ratio for the external TF ripples δ_{vac} is less than 0.01 in the plasma. In addition to that, the beta value for an ITER plasma is relatively low: the volume-averaged beta value $\langle \beta \rangle$ is approximately 2%. In this case, $\widetilde{\boldsymbol{B}}^{\mathrm{pl}}$ is negligible and performing the 3D calculation may be unnecessary. However, for $\langle \beta \rangle > 2\%$, these issues have not been fully discussed yet. Strumberger et.al. reported that $\widetilde{\boldsymbol{B}}^{\mathrm{pl}}$ increased δ by 10% in the high-beta ITER-like plasma and concluded that this difference is negligible [8]. However, since they did not calculate the energetic ion orbits, it can not be confirmed whether this increase negligibly affects the confinement of energetic ions.

The 2D MHD equilibrium field $\langle \boldsymbol{B} \rangle$ in Eq. (4.1) also affects the energetic ion losses. It is well known that the Shafranov shift, which is caused by the vertical field due to the Pfirsch-Schlüter current, changes the birth profile of the alpha particles and affects the confinement of them [22]. The $\langle \boldsymbol{B} \rangle$ also includes the diamagnetic effect of the toroidal field due to the diamagnetic current. By the diamagnetic effect, the magnetic field strength $|B|$ is reduced and the $|B|$ contour line on the poloidal cross-section is strongly altered. In a low-beta plasma, the diamagnetic effect on the magnetic field structure is sometimes ignored for the research of the energetic ion losses. Suzuki et.al. used the 3D MHD equilibrium equation code VMEC [10][11] to investigate the finite beta effects on the TF ripples [9]. They investigated in a relatively high-beta tokamak plasma, $\langle \beta \rangle \sim 12.9$ %, with an impractical circular cross-section. They clarified several finite beta effects, including the non-axisymmetric effect, the Shafranov shift effect, and the diamagnetic effect on the deeply ripple-trapped particles. However, since they did not calculate energetic ion orbits, the finite beta effects on them were not discussed.

For these reasons, both MHD equilibrium equation and orbit equation should be calculated to precisely analyze the finite beta effects on the ripple-induced orbit losses. In the present study, the VMEC and GCB codes [19] are respectively used to perform the MHD equilibrium and orbit calculations in a D-shaped tokamak; this is almost the same model as that used in Refs. [8] and [13]. The guiding center orbit equation can be calculated using the GCB code in the Boozer coordinates from the results obtained using the VMEC code [23][16][15]. To clarify the physical mechanism of the finite beta effects, the typical energetic ion orbits are calculated for the various beta plasmas. Therefore, the actual loss power fraction of fusion alpha particles could not be calculated in this study. The remainder of the paper is organized as follows. The finite beta effects on the MHD equilibria are clarified for a realistic D-shaped rippled tokamak in Sec. 4.2. These effects on the ripple-induced orbit losses are discussed in Sec. 4.3. Finally, Sec. 4.4 summarizes the findings and conclusions of this study.

4.2 MHD equilibrium calculation

The MHD equilibria are calculated using the VMEC code, which is based on the energy principle expressed in the flux coordinates (s, θ, ζ), where s is the normalized toroidal flux, θ is the poloidal angle, and ζ is the toroidal angle. There are three $\langle\beta\rangle$ cases in this study: 2.34% (J1), 3.99% (J2) and 5.22% (J3). $\langle\beta\rangle = 5.22$ % for J3 is realistic for the spherical tokamaks and the commercial reactors such as DEMO. To set the plasma inside the given separatrix, the toroidal magnetic flux at the plasma edge $\Psi_{\rm edge}$, the total plasma current $J_{\rm pl}$ and the external poloidal coil currents are changed. Because 18 TFCs produce $2\pi/18$ toroidal periods, the computational cost can be reduced by employing the periodic boundary conditions. In the VMEC calculations, the number of the radial grid points for s is 40 and the poloidal and toroidal mode numbers are 12 and 8, respectively.

4.2.1 Finite beta effects on field structures

This section clarifies the finite beta effects on the field structures. There are two plasma currents in a fusion plasma: the poloidal and toroidal currents. The poloidal current $j_{\rm pol}$ is called the diamagnetic current $j_{\rm dia}$ because it reduces the toroidal field strength in a high-beta plasma $\beta_{\rm pol} > 1$. Figures 4.1(a) and (b) respectively show the toroidal and vertical field components of J3 along the R direction at $(Z, \phi) = (0.5\ {\rm m}, 0)$. The red, green, and blue lines in this figure indicate the vacuum field due to the external coil current, the field due to the plasma current, and the equilibrium field, respectively. At $R = 7$ m, the toroidal field is strongly reduced to 4.5 T from 4.7 T, which is a 4 % reduction. Since a huge toroidal current $j_{\rm tor}$ is required to generate closed flux surfaces in a tokamak plasma, it is usually larger than $j_{\rm pol}$. In this toroidal current, Pfirsch-Schlüter current $j_{\rm PS}$ is also included. The magnitude of B_z is high, especially at the outer torus.

Figure 4.2 shows the magnitude of the equilibrium toroidal field $B_{\rm tor}$, the vacuum field $|B^{\rm ext}|$, and the equilibrium field $|B^{\rm eq}|$ for J3 in the R direction at $(Z, \phi) = (0.5\ {\rm m}, 0)$. The vacuum field strength $|B^{\rm ext}|$ is inversely proportional to R. At $R = 7.5$ m, $|B^{\rm eq}|$ is reduced by the diamagnetic effect, while it is increased by the poloidal field due to the plasma current beyond $R = 7.5$ m. In the results, $|B^{\rm eq}|$ has the same value at the same Z position and there is a hole in the R direction. This causes the $|B^{\rm eq}|$ contour to be closed at the outer torus; this effect is discussed in Sec. 4.2.4.

To accurately investigate the finite beta effects, the non-axisymmetric component of the field strength ΔB is represented according to [9],

$$
\begin{aligned}
\Delta B &\equiv B(\phi = 0) - B(\phi = \pi/18) \\
&= \left((\langle B \rangle_{\rm tor} + \widetilde{B}_{\rm tor})^2 + (\langle B \rangle_{\rm pol} + \widetilde{B}_{\rm pol})^2 \right)^{1/2} \\
&\qquad - \left((\langle B \rangle_{\rm tor} - \widetilde{B}_{\rm tor})^2 + (\langle B \rangle_{\rm pol} - \widetilde{B}_{\rm pol})^2 \right)^{1/2} \\
&\sim \left((\langle B \rangle_{\rm tor})^2 + (\langle B \rangle_{\rm pol})^2 \right)^{1/2} \left[\left(1 + 2 \frac{\langle B \rangle_{\rm tor} \widetilde{B}_{\rm tor} + \langle B \rangle_{\rm pol} \widetilde{B}_{\rm pol}}{(\langle B \rangle_{\rm tor})^2 + (\langle B \rangle_{\rm pol})^2} \right)^{1/2} \right. \\
&\qquad \left. - \left(1 - 2 \frac{\langle B \rangle_{\rm tor} \widetilde{B}_{\rm tor} + \langle B \rangle_{\rm pol} \widetilde{B}_{\rm pol}}{(\langle B \rangle_{\rm tor})^2 + (\langle B \rangle_{\rm pol})^2} \right)^{1/2} \right] \\
&\sim \left((\langle B \rangle_{\rm tor})^2 + (\langle B \rangle_{\rm pol})^2 \right)^{1/2} \left[\left(1 + \frac{\langle B \rangle_{\rm tor} \widetilde{B}_{\rm tor} + \langle B \rangle_{\rm pol} \widetilde{B}_{\rm pol}}{(\langle B \rangle_{\rm tor})^2 + (\langle B \rangle_{\rm pol})^2} \right) \right. \\
&\qquad \left. - \left(1 - \frac{\langle B \rangle_{\rm tor} \widetilde{B}_{\rm tor} + \langle B \rangle_{\rm pol} \widetilde{B}_{\rm pol}}{(\langle B \rangle_{\rm tor})^2 + (\langle B \rangle_{\rm pol})^2} \right) \right] \\
&\sim 2 \frac{\langle B \rangle_{\rm tor} \widetilde{B}_{\rm tor} + \langle B \rangle_{\rm pol} \widetilde{B}_{\rm pol}}{\left((\langle B \rangle_{\rm tor})^2 + (\langle B \rangle_{\rm pol})^2 \right)^{1/2}} \\
&\sim \frac{2 \langle B \rangle_{\rm tor} \widetilde{B}_{\rm tor}}{\left((\langle B \rangle_{\rm tor})^2 + (\langle B \rangle_{\rm pol})^2 \right)^{1/2}} + \frac{2 \langle B \rangle_{\rm pol} \widetilde{B}_{\rm pol}}{\left((\langle B \rangle_{\rm tor})^2 + (\langle B \rangle_{\rm pol})^2 \right)^{1/2}} \\
&\sim \frac{2 \widetilde{B}_{\rm tor}}{\left(1 + \left(\langle B \rangle_{\rm pol} / \langle B \rangle_{\rm tor} \right)^2 \right)^{1/2}} + \frac{2 \widetilde{B}_{\rm pol}}{\left(1 + \left(\langle B \rangle_{\rm tor} / \langle B \rangle_{\rm pol} \right)^2 \right)^{1/2}}
\end{aligned}
$$

By using $f = \langle B \rangle_{\rm tor} / \langle B \rangle_{\rm pol}$,

$$\begin{aligned} \Delta B &\sim 2\widetilde{B}_{\rm tor}(1+f^2)^{-1/2} + 2\widetilde{B}_{\rm pol}(1+f^{-2})^{-1/2} \\ &\sim 2\left(1-\frac{f^2}{2}\right)\widetilde{B}_{\rm tor} + 2f\widetilde{B}_{\rm pol} \\ &\sim 2\left(1-\frac{f^2}{2}\right)\widetilde{B}^{\rm ext}_{\rm tor} + 2\left(1-\frac{f^2}{2}\right)\widetilde{B}^{\rm pl}_{\rm tor} + 2f\widetilde{B}^{\rm ext}_{\rm pol} + 2f\widetilde{B}^{\rm pl}_{\rm pol} \\ \therefore\ \Delta B &\sim 2\left[\left(1-\frac{f^2}{2}\right)\widetilde{B}^{\rm ext}_{\rm tor} + \widetilde{B}^{\rm pl}_{\rm tor} + f\widetilde{B}^{\rm pl}_{\rm pol}\right] \end{aligned} \tag{4.2}$$

where $\langle B \rangle$ is the axisymmetric field component, $B^{\rm ext}$ is the vacuum field, and $B^{\rm pl}$ is the field generated by the plasma current. Unlike [9], $\widetilde{B}$ includes the non-axisymmetric poloidal field component. Therefore, $\widetilde{B}$ is affected not only by the non-axisymmetric field but also by the axisymmetric toroidal and poloidal fields. $\widetilde{B}^{\rm ext}_{\rm tor}$ has the largest effect because it is induced by the TF ripples. In contrast, the effect of $\widetilde{B}^{\rm ext}_{\rm pol}$ is negligibly small. The magnitude of $\widetilde{B}^{\rm pl}_{\rm pol}$ is larger than that of $\widetilde{B}^{\rm pl}_{\rm tor}$ because $j_{\rm tor}$ is larger than $j_{\rm pol}$ in a tokamak plasma. However, the effect of the non-axisymmetric poloidal field is reduced by the factor $f = \langle B \rangle_{\rm pol} / \langle B \rangle_{\rm tor}$. Therefore, the effect of $\widetilde{B}^{\rm pl}_{\rm pol}$ becomes important at the outer torus.

The effects of $\widetilde{B}^{\rm pl}_{\rm tor}$ and $\widetilde{B}^{\rm pl}_{\rm pol}$ should be considered separately. According to [9], $j_{\rm tor}$ is largest and $j_{\rm pol}$ is smallest under the TFCs in the toroidal direction. Since the poloidal field is mainly generated by $j_{\rm tor}$, the poloidal field from $j_{\rm tor}$ is largest and smallest at the top and bottom of the ripples, respectively. In the results, $j_{\rm tor}$ mainly enhances the non-axisymmetric field, whereas the toroidal field is mainly generated by the TFCs. If $j_{\rm pol}$ is diamagnetic for $\beta_{\rm pol} > 1$ plasma, $B_{\rm tor}$ will be reduced more at the bottom than at the top of the ripples, so $\widetilde{B}^{\rm pl}_{\rm tor}$ will be increased. This implies that the non-axisymmetric effects due to both $j_{\rm tor}$ and $j_{\rm pol}$ increase the ripple field in a high-beta plasma.

4.2.2 Ripple ratio along the toroidal angle

Figure 4.3(a) shows the ripple ratio for the vacuum toroidal ripple field $\delta_{\rm vac}$ on the poloidal cross-section. At the outer torus, $\delta_{\rm vac}$ is high because the gap between the TFCs is greater so that the non-axisymmetric field generated by the TFCs is greater. The maximum value of $\delta_{\rm vac}$ is almost 0.01, which is considered to be the upper limit for the tokamaks such as the JT-60U based on the consideration of energetic ion losses and plasma confinement [24]. The finite beta effects alter the ripple ratio. Figure 4.3(b) shows the ripple ratios δ for the vacuum ripple field $\delta_{\rm vac}$ and for scenario J3, δ(J3). Figure 4.4(a) shows $\delta_{\rm vac}$ and δ(J3) in the R direction at $(Z, \phi) = (0.5\ {\rm m}, 0)$. In these figures, δ is lower at the outer torus and higher in the core region. To perform the detailed analysis, the δ components

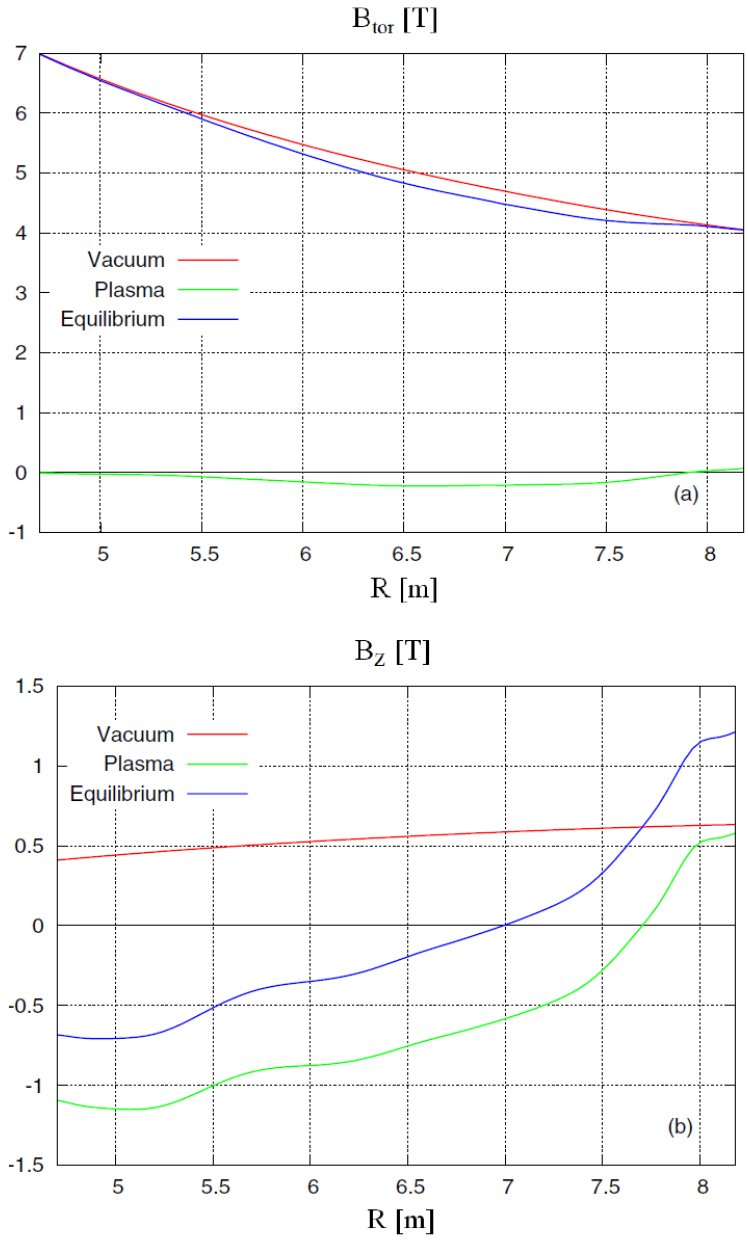

Figure 4.1: (a) B_{tor} and (b) B_{z} of the vacuum field, the field generated by the plasma current, and the equilibrium field for J3 in the R direction at $(Z, \phi) = (0.5\ \mathrm{m}, 0)$

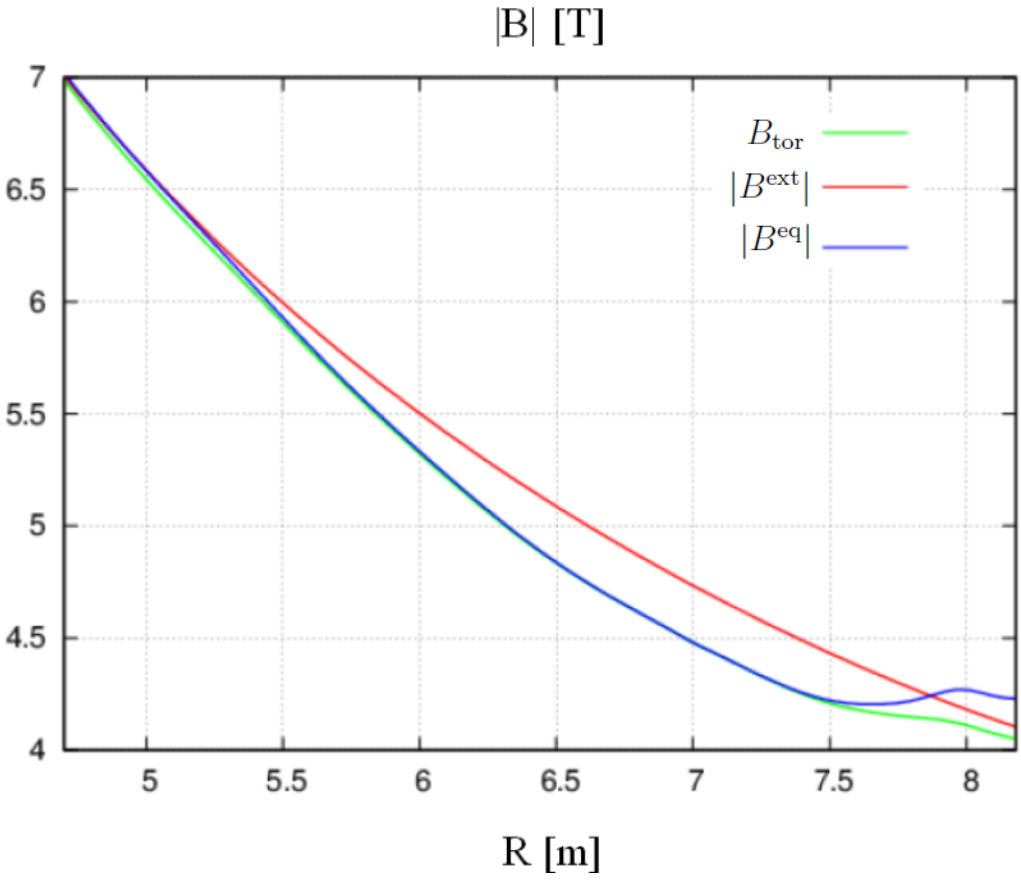

Figure 4.2: The magnitudes of the equilibrium toroidal field B_{tor}, the vacuum field $|B^{\mathrm{ext}}|$, and the equilibrium field $|B^{\mathrm{eq}}|$ for J3 in the R direction at $(Z, \phi) = (0.5\ \mathrm{m}, 0)$

are described by equation (4.2),

$$
\begin{aligned}
\delta &= \frac{B_{\max} - B_{\min}}{B_{\max} + B_{\min}} = \frac{\Delta B}{2\langle B\rangle} \\
&= \frac{\Delta B}{2}\langle B\rangle^{-1} \\
&= \frac{\Delta B}{2}\left(\left(\langle B\rangle_{\rm tor}\right)^2 + \left(\langle B\rangle_{\rm pol}\right)^2\right)^{-1/2} \\
&= \frac{\Delta B}{2\langle B\rangle_{\rm tor}}\left(1+f^2\right)^{-1/2} \\
&\sim \frac{\Delta B}{2\langle B\rangle_{\rm tor}}\left(1-\frac{f^2}{2}\right) \\
&\sim \frac{\Delta B}{2}\left(1-\frac{f^2}{2}\right)\left(\langle B\rangle_{\rm tor}^{\rm ext} + \langle B\rangle_{\rm tor}^{\rm pl}\right)^{-1} \\
&\sim \frac{\Delta B}{2\langle B\rangle_{\rm tor}^{\rm ext}}\left(1-\frac{f^2}{2}\right)\left(1-\frac{\langle B\rangle_{\rm tor}^{\rm pl}}{\langle B\rangle_{\rm tor}^{\rm ext}}\right) \\
&\sim \frac{1}{\langle B\rangle_{\rm tor}^{\rm ext}}\left(1-\frac{f^2}{2}\right)\left(1-\frac{\langle B\rangle_{\rm tor}^{\rm pl}}{\langle B\rangle_{\rm tor}^{\rm ext}}\right)\left[\left(1-\frac{f^2}{2}\right)\widetilde{B}_{\rm tor}^{\rm ext} + \widetilde{B}_{\rm tor}^{\rm pl} + f\widetilde{B}_{\rm pol}^{\rm pl}\right] \\
&\sim \frac{1}{\langle B\rangle_{\rm tor}^{\rm ext}}\left(1-\frac{f^2}{2}\right)^2\left(1-\frac{\langle B\rangle_{\rm tor}^{\rm pl}}{\langle B\rangle_{\rm tor}^{\rm ext}}\right)\widetilde{B}_{\rm tor}^{\rm ext} + \frac{\widetilde{B}_{\rm tor}^{\rm pl}}{\langle B\rangle_{\rm tor}^{\rm ext}} + \frac{f\widetilde{B}_{\rm pol}^{\rm pl}}{\langle B\rangle_{\rm tor}^{\rm ext}} \\
&\sim \frac{1}{\langle B\rangle_{\rm tor}^{\rm ext}}\left(1-f^2+\frac{f^4}{4}\right)\left(1-\frac{\langle B\rangle_{\rm tor}^{\rm pl}}{\langle B\rangle_{\rm tor}^{\rm ext}}\right)\widetilde{B}_{\rm tor}^{\rm ext} + \frac{\widetilde{B}_{\rm tor}^{\rm pl}}{\langle B\rangle_{\rm tor}^{\rm ext}} + \frac{f\widetilde{B}_{\rm pol}^{\rm pl}}{\langle B\rangle_{\rm tor}^{\rm ext}} \\
&\sim \frac{1}{\langle B\rangle_{\rm tor}^{\rm ext}}\left(1-f^2\right)\left(1-\frac{\langle B\rangle_{\rm tor}^{\rm pl}}{\langle B\rangle_{\rm tor}^{\rm ext}}\right)\widetilde{B}_{\rm tor}^{\rm ext} + \frac{1}{\langle B\rangle_{\rm tor}^{\rm ext}}\widetilde{B}_{\rm tor}^{\rm pl} + \frac{f}{\langle B\rangle_{\rm tor}^{\rm ext}}\widetilde{B}_{\rm pol}^{\rm pl} \\
&\sim \frac{1}{\langle B\rangle_{\rm tor}^{\rm ext}}\widetilde{B}_{\rm tor}^{\rm ext} - \frac{f^2\langle B\rangle_{\rm tor}^{\rm ext} + \langle B\rangle_{\rm tor}^{\rm pl}}{\left(\langle B\rangle_{\rm tor}^{\rm ext}\right)^2}\widetilde{B}_{\rm tor}^{\rm ext} + \frac{1}{\langle B\rangle_{\rm tor}^{\rm ext}}\widetilde{B}_{\rm tor}^{\rm pl} + \frac{f}{\langle B\rangle_{\rm tor}^{\rm ext}}\widetilde{B}_{\rm pol}^{\rm pl} \\
\therefore\ \delta &\sim \delta_{\rm vac} + \delta_{\rm 2D} + \delta_{\rm tor}^{\rm pl} + \delta_{\rm pol}^{\rm pl}
\end{aligned}
\tag{4.3}
$$

where $\delta_{\rm 2D}$, $\delta_{\rm tor}^{\rm pl}$, and $\delta_{\rm pol}^{\rm pl}$ are the finite beta effects of the axisymmetric component and the non-axisymmetric toroidal field and poloidal field components, respectively. To clarify the finite beta effect on the TF ripples, Fig. 4.4(b) shows each δ component for J3 along the R direction at $(Z, \phi) = (0.5\ \mathrm{m}, 0)$. While all the finite beta effects are comparable, they are much smaller than $\delta_{\rm vac}$.

Table 4.1 shows each δ component at $(R, Z) = (7.9\ \mathrm{m}, 0.5\ \mathrm{m})$ for J3. The axisymmetric finite beta effects $\delta_{\rm 2D}$ reduce the vacuum toroidal ripple $\delta_{\rm vac}$ by 3.85 %, while the non-axisymmetric finite beta effects $\delta_{\rm tor}^{\rm pl}$ and $\delta_{\rm pol}^{\rm pl}$ increase $\delta_{\rm vac}$ by 2.81 and 5.93 %, respectively.

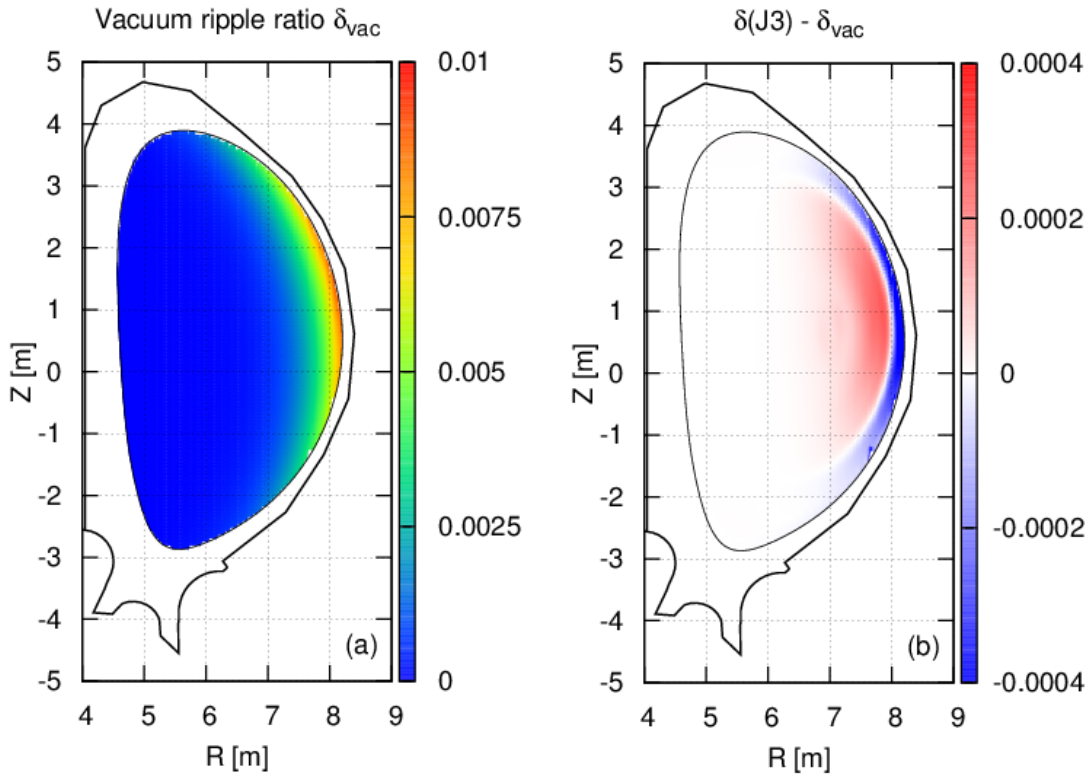

Figure 4.3: The distributions of δ for (a) the vacuum toroidal ripple field and (b) J3 on the poloidal cross-section

This means that δ of the 3D MHD equilibrium field is increased by 8.73 % compared to δ for the vacuum approximation in the $\langle\beta\rangle = 5.22$ % plasma. We were unable to determine whether this 8.73 % increase in δ is negligibly small; this problem should be solved by calculating the actual loss power fraction of the energetic ions in a future study.

4.2.3 Ripple well depth along magnetic field line

In the previous section, the non-axisymmetric field was evaluated as a function of the toroidal angle for fixed R and Z. However, for energetic ion orbits, it is more meaningful to define the ripple field along the field line. The ripple well depth d_w along the field line is defined by

$$\mathrm{d}_w = \frac{B'_{\max} - B'_{\min}}{B'_{\max} + B'_{\min}}, \tag{4.4}$$

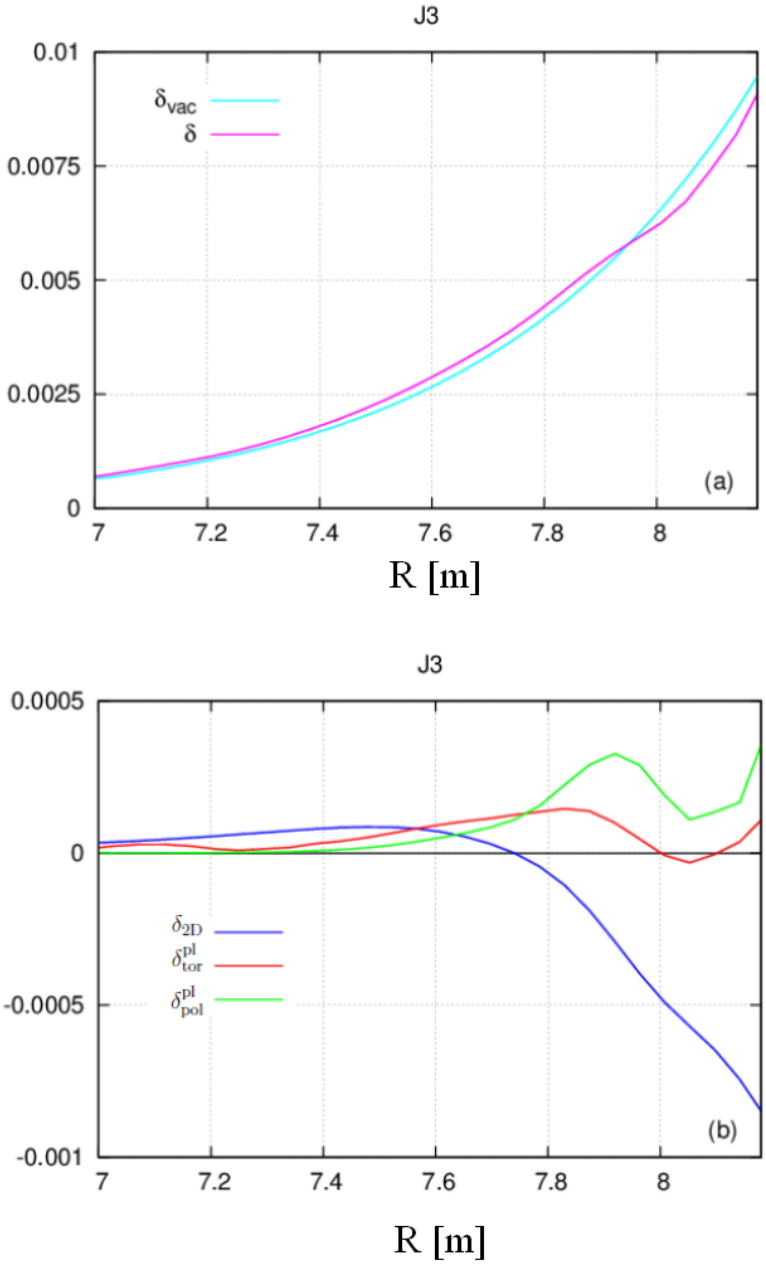

Figure 4.4: (a) The vacuum toroidal ripple ratio and the ripple ratio for J3 and (b) each δ component for J3 in the R direction at $(Z, \phi) = (0.5\ \mathrm{m}, 0)$

Table 4.1: δ components at $(R, Z) = (7.9\ \mathrm{m}, 0.5\ \mathrm{m})$ for J3

Scenario	$\langle\beta\rangle$ %	δ_{vac}	δ_{2D}	$\delta^{\mathrm{pl}}_{\mathrm{tor}}$	$\delta^{\mathrm{pl}}_{\mathrm{pol}}$	δ
J3	5.22	0.004909	-0.000189	0.000138	0.000291	0.005149
		100 %	-3.85 %	2.81 %	5.93 %	104.88 %

where B'_{max} and B'_{min} are respectively the maximum and minimum values of $|B|$ along the field line. Figure 4.6(a) shows the d_w distribution for J3 on the poloidal cross-section. The ripple well depth d_w depends strongly on the field line pitch (i.e., the local inclination of the field lines). The ripple well exists if the following condition is satisfied,

$$\alpha \equiv \left| \frac{(\partial \langle B \rangle / \partial l)}{(\partial B_{\mathrm{3D}} / \partial l)} \right| < 1 \tag{4.5}$$

where l is the distance along the field line [25][26]. For a steeper pitch, α is increased and d_w is reduced, as shown in Fig. 4.5. Figure 4.6(b) shows the difference in the ripple well depths d_w for J3 and J1 (i.e., J3 − J1) to clarify the finite beta effects on the ripple well. In this figure, δ is reduced at the outer torus and increased at the core region. This relation is more remarkable than δ in Sec. 4.2.2. It implies that the field line pitch is steep in a high-beta plasma at the outer torus.

The Pfirsch-Schlüter current flows along the magnetic field line. This parallel current generates the poloidal magnetic field and alters the field line pitch. Figure 4.7(a) shows $|B| / |B_0|$ on the field line that passes through $(R, Z, \phi) = (8.0\ \mathrm{m}, 0.5\ \mathrm{m}, 0)$ for the 2D equilibrium field, where B_0 is $|B|$ at $(R, Z, \phi) = (8.0\ \mathrm{m}, 0.5\ \mathrm{m}, 0)$. As mentioned above, the field line pitch becomes steeper at the outer torus with increasing the beta value. Figure 4.7(b) shows $|B| / |B_0|$ for the 3D equilibrium field. In this figure, d_w is reduced at the outer torus because of the steeper field line pitch in a high-beta plasma.

4.2.4 Change in the field strength contour

The deeply ripple-trapped particles are repeatedly reflected by the magnetic mirror effect and they drift along the bottom of the ripple well [18]. The B_{min} contour, which was defined in Sec. 4.2.2, can be used to estimate and control their orbits.

Figures 4.8(a), (b), and (c) show the B_{min} contours for J1, J2, and J3, respectively. At the outer torus, the contour curvature becomes higher with increasing the beta value and it eventually becomes closed at the outer torus. This phenomena is induced by the diamagnetic effect of j_{pol} and the paramagnetic effect of j_{tor}, as mentioned in Sec. 4.2.1. The curved B_{min} contour enables the deeply ripple-trapped particles to move more easily to high δ and d_w regions. However, if this contour is completely closed in a high-beta plasma, the trapped particle losses will be reduced.

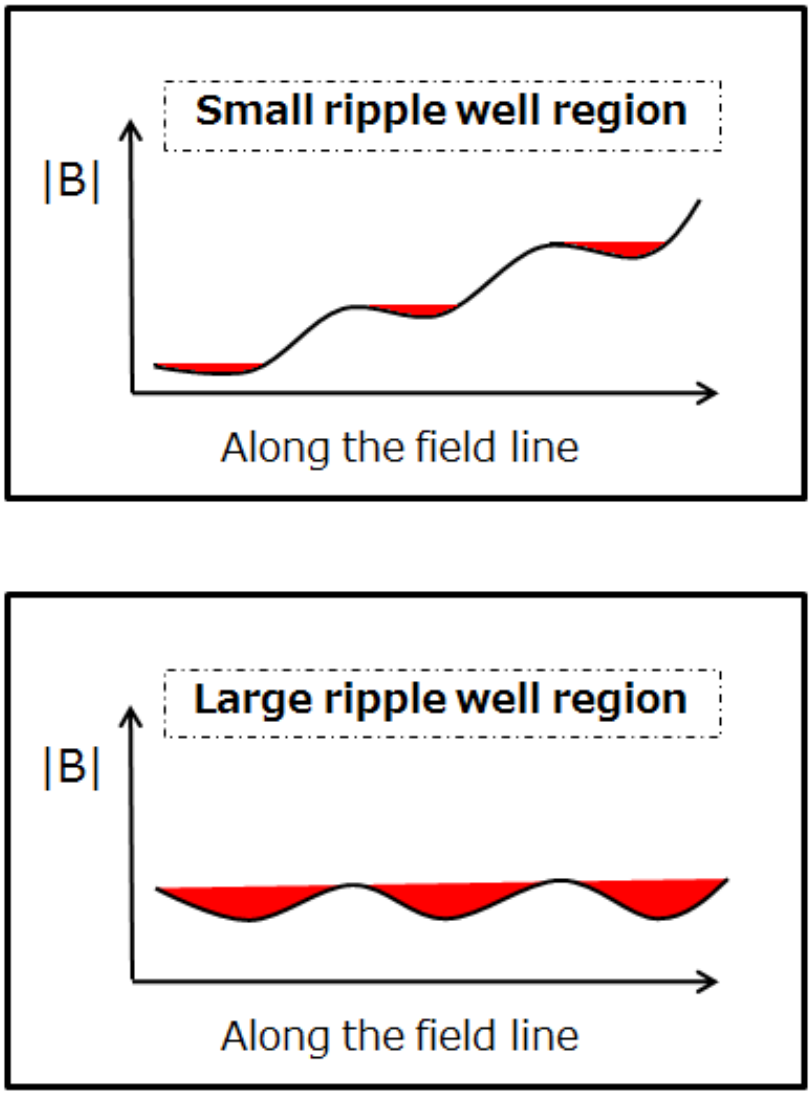

Figure 4.5: The ripple well region for the pitch of the magnetic field line

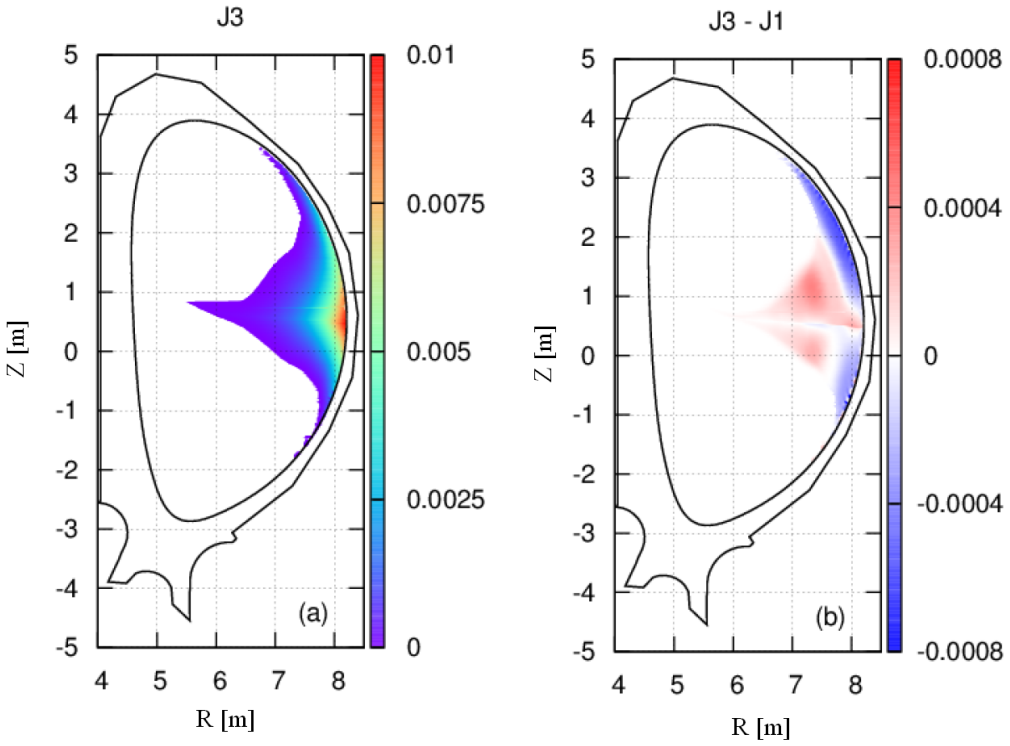

Figure 4.6: The distribution of d_w for (a) J3 and (b) J3 − J1 in the poloidal cross-section

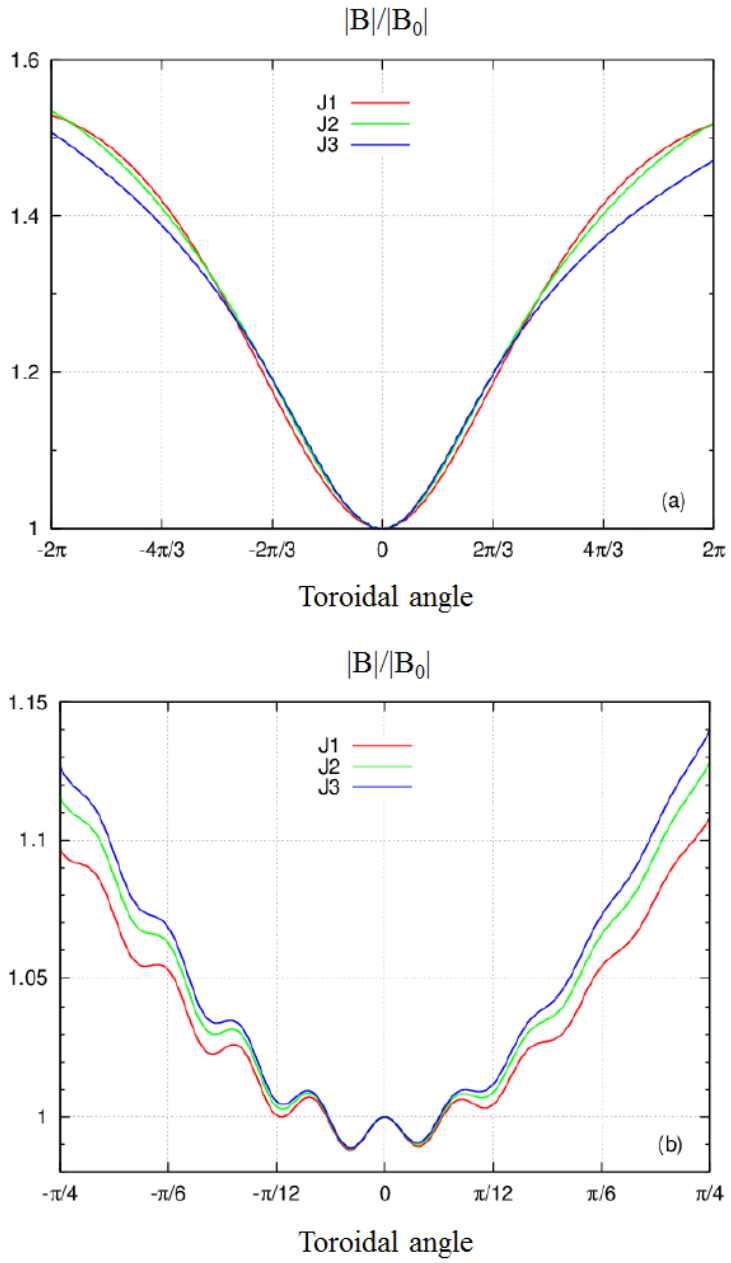

Figure 4.7: The variation in $|B|/|B_0|$ for (a) 2D and (b) 3D MHD equilibrium field on the field line that passes through $(R, Z, \phi) = (8.0\text{ m}, 0.5\text{ m}, 0)$

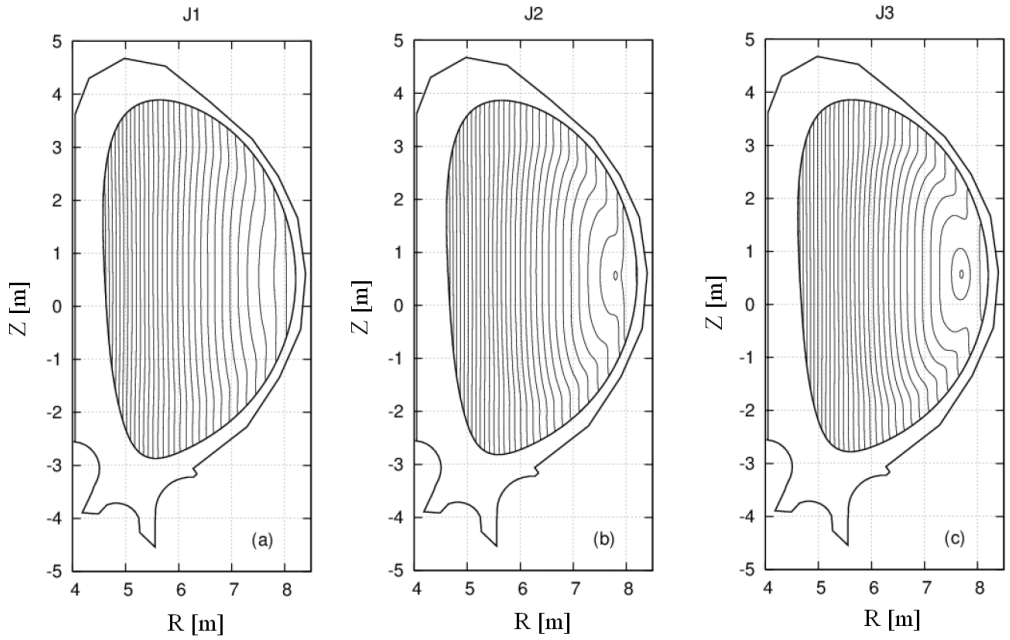

Figure 4.8: $B_{\min}$ contours for (a) J1, (b) J2, and (c) J3 in the poloidal cross-section

Not only the deeply ripple-trapped particles, but also the banana-trapped particles are associated with the field strength $|B|$ contour because the banana tip also moves along it. Because the parallel velocity $v_{\parallel}$ is zero at the banana tip, the magnetic moment μ_m can be written as,

$$\mu_m = \frac{mv_{\perp}^2}{2\,|B|} = \frac{mv^2}{2B_{\text{tip}}}, \tag{4.6}$$

where B_{tip} is $|B|$ at the banana tip. The banana tip follows the $|B|$ contour because μ_m and $\frac{mv^2}{2}$ are conserved. If the particles are trapped in the closed $|B|$ contour region, they do not be lost. However, if the particles are trapped in the non-closed $|B|$ contour region, their orbits strongly depend on the $|B|$ contour curvature. The diamagnetic effect increases the $|B|$ contour curvature and the banana tip also more easily move to the outer torus. Therefore, the particles, which are trapped in the non-closed $|B|$ contour region, are more strongly affected by the ripple field and the energetic ion losses will be increased. This is confirmed in Section 3 where their orbits are calculated.

4.2.5 Change in the flux surface positions

The Shafranov shift strongly affects the alpha particle losses, which are produced by a thermal-thermal reaction. The vertical field is generated by the Pfirsch-Schlüter current and the flux surfaces are shifted to the outer torus. Figure 4.9 shows the changes in the positions of the normalized toroidal flux surfaces $s = (0.2, 0.4, 0.6, 0.8, \text{and } 1.0)$ at $\zeta = 0$.

The Shafranov shift moves the generation points of the alpha particles out to the outer torus, namely the higher ripple region. In addition, it reduces the distance from the generation point to the first wall. In the results, the Shafranov shift effect increases the energetic ion losses and the heat loads due to the fusion alpha particles.

4.3 Finite beta effects on energetic ion orbits

4.3.1 Classification of orbits in a rippled tokamak

The finite beta effects on the MHD equilibria were clarified in the previous section. However, the orbit calculation is also required to quantitatively estimate the finite beta effects on the energetic ion losses. In this study, the energetic ion orbits are calculated by the GCB code, which is based on the guiding center orbit equations in the Boozer coordinates. However, the orbits cannot be determined outside the plasma because the flux coordinates are used. This calculation also ignores collisions. Therefore, the particles are assumed to be lost when the guiding center reaches the plasma boundary, unless the tracing time exceeds 0.01 s, in which case they are assumed to be non-loss particles. While the actual loss power fraction of energetic ions could not be obtained, it is sufficient to only classify the orbits in a rippled tokamak.

Figures 4.10(a), (b), and (c) show the orbit classification of the alpha particles that start at $(R, Z, \phi) = (7.5\text{ m}, 0.5\text{ m}, \pi/18)$ for J1, J2, and J3, respectively. The initial energy E_0 is divided between 1.0 and 3.5 MeV in 0.1 MeV intervals and the pitch angle λ, which is defined as

$$\lambda = \frac{1}{\pi}\mathrm{Tan}^{-1}\left(\frac{v_\perp}{v_\parallel}\right). \tag{4.7}$$

is divided between 0 and 1 in 0.01 intervals. They are classified according to the following colors:

- Passing particles [Blue]
- Banana-trapped loss particles [Red]
- Banana-trapped non-loss particles [Light blue]
- Ripple-trapped loss particles [Black]

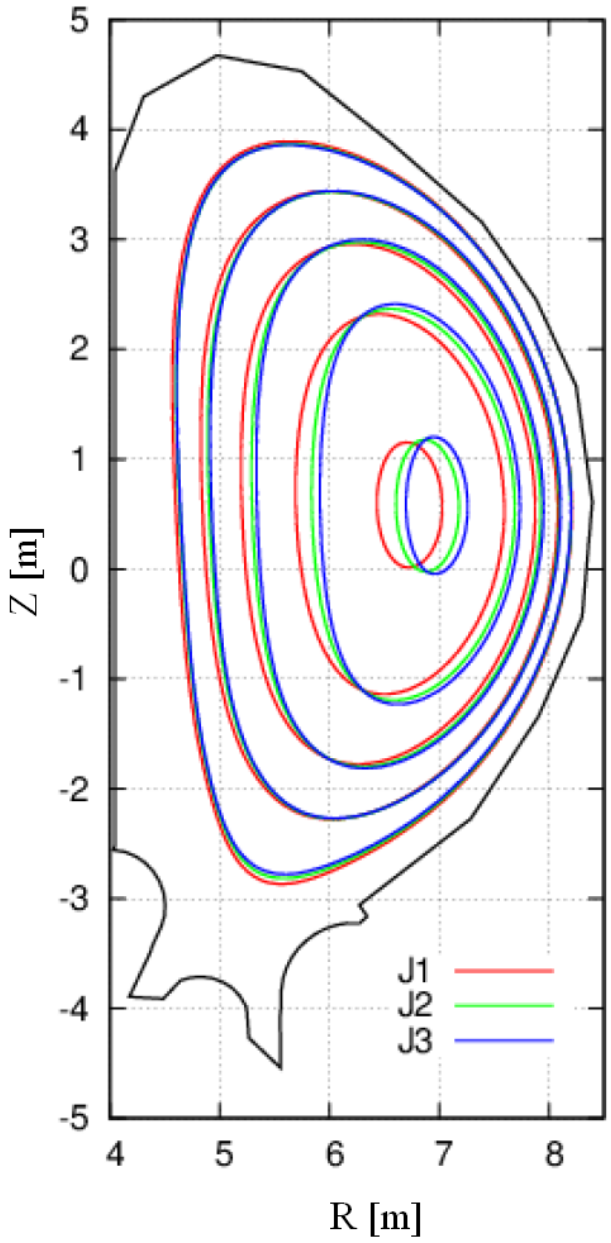

Figure 4.9: The changes in the position of s = (0.2, 0.4, 0.6, 0.8, and 1.0) at $\zeta = 0$ for each beta value

- Ripple-trapped non-loss particles [Yellow],

where ripple-trapped particles are defined as trapped particles that are confined only in the d_w region and the banana-trapped particles are the other trapped particles. Figures 4.11(a), (b), and (c) show the $B_{\min}$ contours (the black line) and the orbits of the particles (the red line), which start from $(R, Z, \phi) = (7.5\ \text{m}, 0.5\ \text{m}, \pi/18)$ for J1, J2, and J3, respectively. For J3, the $B_{\min}$ contour is closed at the initial point; it thus describes a closed path. For J1 and J2, these particles reach the plasma boundary. For J1, the deeply ripple-trapped particles escape from the d_w region and become the disturbed banana particles. However for J2, the orbit follows the $B_{\min}$ contour because this contour curves toward the high ripple region.

Figures 4.12(a) and (b) respectively show the loss power fraction ϵ and the loss position on the plasma boundary for 3.5 MeV alpha particles with respect to λ. The initial position is fixed at $(R, Z, \phi) = (7.5\ \text{m}, 0.5\ \text{m}, \pi/18)$ and λ is divided between 0 and 1 in 0.0001 intervals. Figure 4.13(a) shows that the loss process can be separated into the rapid and slow loss. The rapid loss particles appear only in J2; they thus originate from deeply ripple-trapped loss particles. Furthermore, the localized loss position appears only for J2 in Fig. 4.13(b) around $(Z, \phi) = (-0.8\ \text{m}, \pi/36)$. Banana-trapped loss particles have a longer loss time than deeply ripple-trapped particles and the loss positions of the banana-trapped loss particles are widely distributed over the entire plasma boundary. However, the conditions for the deeply ripple-trapped particles are strict, namely $\lambda \sim 0.5$ at the bottom of the ripple well (in this study, $\phi = \pi/18$). The deeply ripple-trapped and the banana-trapped loss particles have quite different loss times and positions. Therefore, the two loss processes should be distinguished when analyzing the finite beta effects on the energetic ion losses.

4.3.2 Finite beta effects on trapped particles

In the previous section, the energetic ion orbits were categorized with respect to λ. In this section, the orbits of the trapped particles are analyzed with respect to the initial position. Figures 4.13(a), (b), and (c) show the classification of the trapped particles that start from $\phi = \pi/18$ with $\lambda = 0.5$, using the same color scheme as Fig. 4.10.

For J2, the number of the ripple-trapped particles (the black region) is increased at the outer torus for two reasons: the increased non-axisymmetric field at the core region and the curved $B_{\min}$ contour, as mentioned in Sec. 4.2.4. The latter is the more important effect because the boundary between the red and black regions has a similar shape to that of the $B_{\min}$ contour and the increase in the ripple ratio is quite small inside the plasma. The closed $B_{\min}$ contour region (the yellow region) for J2 is quite small, whereas the yellow region becomes remarkable for J3 and the number of the deeply ripple-trapped loss particles is highly reduced by this effect. The number of banana-trapped loss particles (the red region) is increased for J3. At $Z = 0.5$ m, the boundary between the red and light-blue region is located at 7 m for J1 and 6.6 m for J3. The banana-trapped

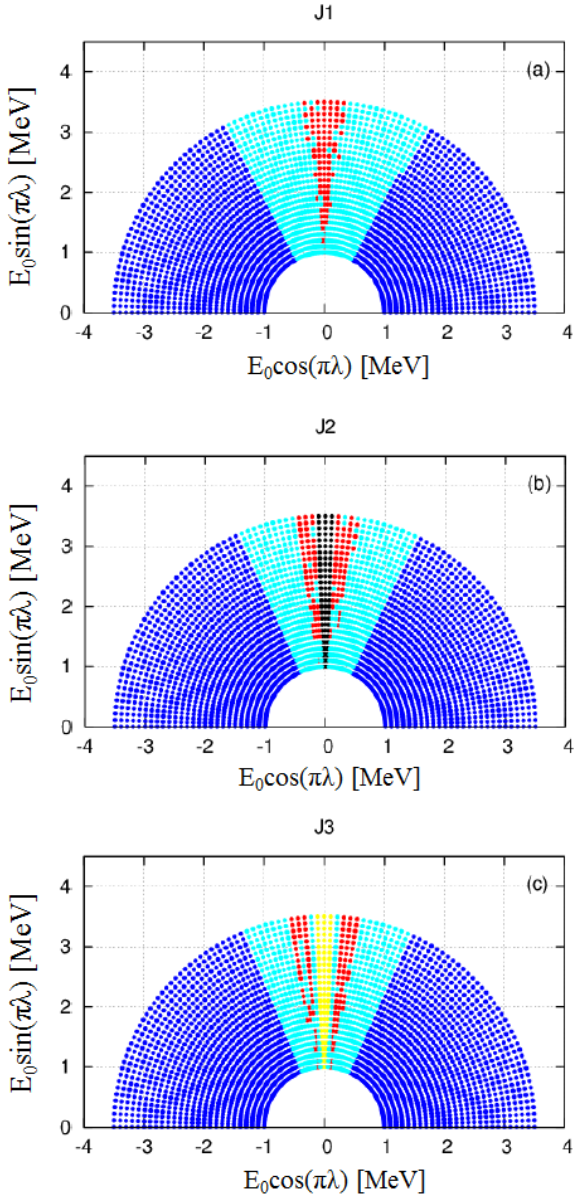

Figure 4.10: The orbit classification of the alpha particles starting from $(R, Z, \phi) = (7.5\text{ m}, 0.5\text{ m}, \pi/18)$ for (a) J1, (b) J2, and (c) J3

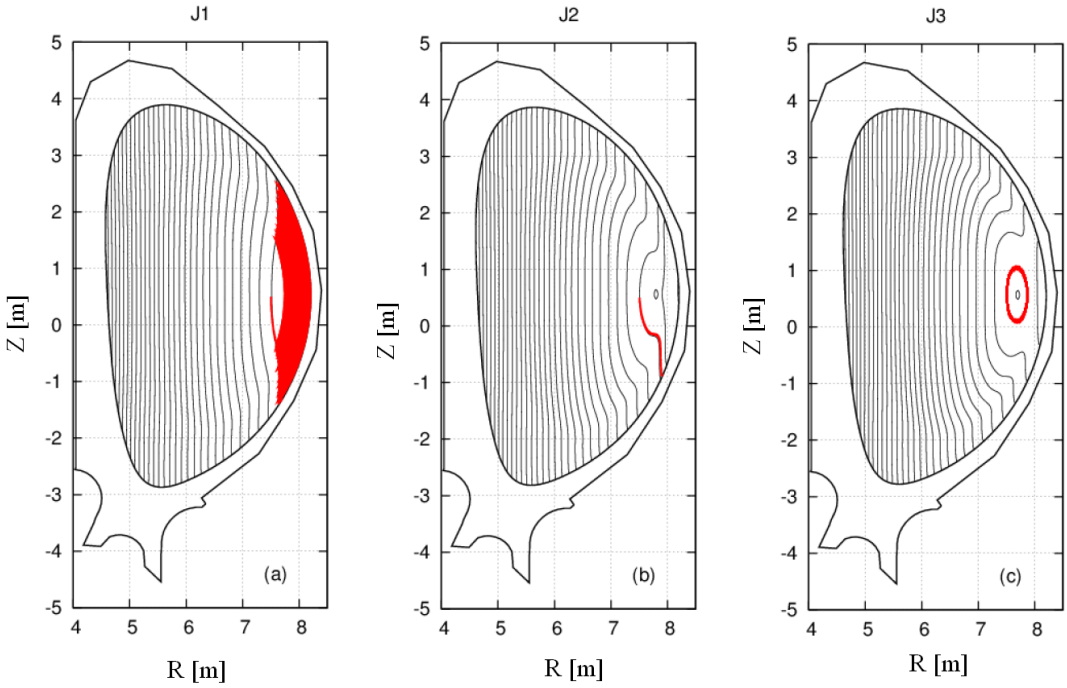

Figure 4.11: The $B_{\min}$ contour (the black line) and the orbits of the particles (the red line) that start from $(R, Z, \phi) = (7.5\ \text{m}, 0.5\ \text{m}, \pi/18)$ with $\lambda = 0.5$ for (a) J1, (b) J2, and (c) J3

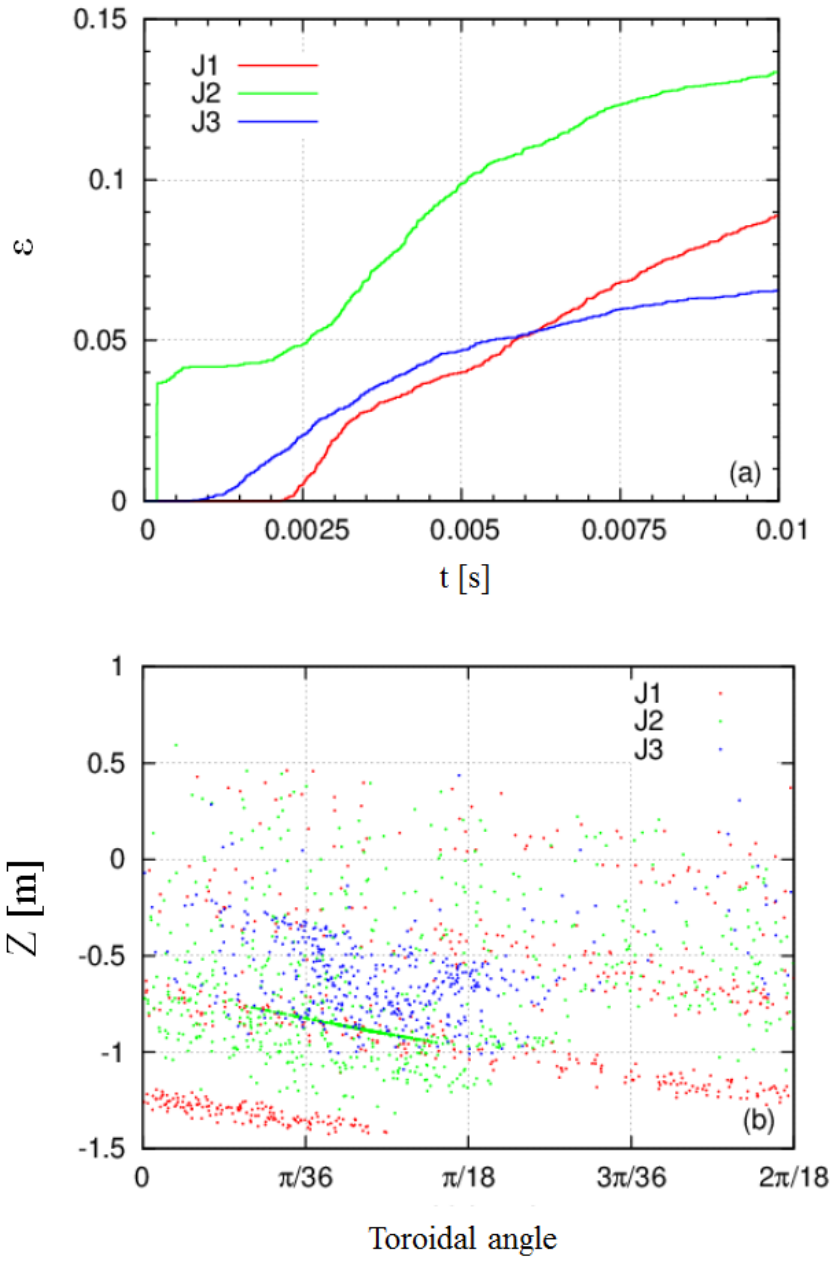

Figure 4.12: (a) The loss power fraction ϵ and (b) the loss position of alpha particles with respect to λ, which start from $(R, Z, \phi) = (7.5\ \text{m}, 0.5\ \text{m}, \pi/18)$

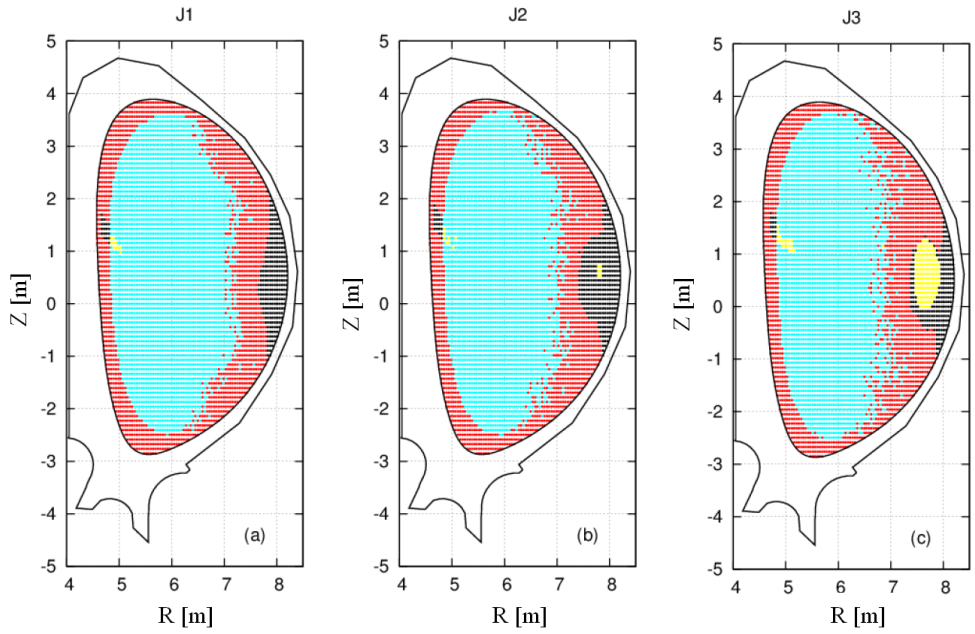

Figure 4.13: The orbit classification of the trapped particles that start from $\phi = \pi/18$ with $\lambda = 0.5$ for (a) J1, (b) J2, and (c) J3

loss particles also originate from the curved $B_{\min}$ contour. A yellow region appears near $(R, Z) = (5\ \mathrm{m}, 1\ \mathrm{m})$. At the inner torus, there are strong ripples because the field strength along the field line is a maximum and the numerator of equation (4.5) becomes quite small. Therefore, particles starting from $(R, Z) = (5\ \mathrm{m}, 1\ \mathrm{m})$ with $\lambda = 0.5$ will be trapped by the ripple well and become passing particles. In the results, they are categorized as the ripple-trapped non-loss particles.

In these figures, the magnitude of the finite beta effects strongly depends on the generation points of the targeted energetic ions. For example, the positions and the pitch angle of the alpha particles produced by the thermal-thermal reaction are randomly disturbed. Therefore, the number of the deeply ripple-trapped particles is quite low. However, for the NBI-generated fast ions, the strong confinement of the deeply ripple-trapped particles permits quasi-perpendicular injection to realize better beam penetration. In the future, the ripple-induced orbit losses should be statistically investigated by the Monte Carlo calculations while considering birth profiles using codes such as the F3D-OFMC code [27].

4.4 Summary

Finite beta effects on the energetic ion losses were studied in a realistic D-shaped tokamak. The finite beta effects on the MHD equilibria were clarified. This topic has been investigated by Suzuki et.al. [9] and Strumberger et.al. [8]. Suzuki et.al. state that "the magnitude of $\widetilde{B}_{\rm pol}$ is usually very small compared with $\widetilde{B}_{\rm tor}$". However, the opposite relation was observed in this study, which indicates that the non-axisymmetric poloidal field cannot be ignored. Strumberger et.al. mainly focused on the non-axisymmetric finite beta effect. In their calculations, the non-axisymmetric finite beta effect increased the ripple ratio by 8.2%, which is very similar to the 8.73% increase obtained in the present study. To precisely clarify the physical considerations, the finite beta effects on the ripple ratio were categorized using equation (4.3). The non-axisymmetric toroidal and poloidal field components generated by the plasma current respectively increased the ripple ratio by up to 2.81 and 5.93% and the axisymmetric finite beta effect reduced it by 3.85%.

Suzuki et.al. said the $B_{\rm min}$ contour was closed in an unrealistic high-beta plasma [9]. In this study, the $B_{\rm min}$ contour started to be closed for $\langle\beta\rangle = 4$ % and a wide closed $|B|$ contour region was obtained for $\langle\beta\rangle = 5$ %. Unlike [9], we investigated how much these finite beta effects alter the energetic ion orbits. The orbit calculations were performed from the same initial position (R, Z) in the different beta plasmas. In Fig. 4.13, a non-loss particle (the yellow) region appears at the outer torus for J2 and J3. The diamagnetic effect reduces the energetic ion losses, which are trapped in the closed $|B|$ contour region. If the particles are trapped in the non-closed $|B|$ contour region, their orbits strongly depend on the contour curvature. Since the $|B|$ contour curvature is increased by the diamagnetic effect, the trapped particles can easily move to the outer torus (i.e., the high ripple region). The banana-trapped loss (the red color) region extends inside the plasma with increasing the beta value. This implies that other trapped particles inside the plasma become loss particles by the finite beta effects. This effect has not been mentioned in the previous studies; we clarified it by calculating the energetic ion orbits actually.

The magnitude of the finite beta effects depends strongly on the generation points of the targeted energetic ions. In the future, we will attempt to estimate the actual loss power fraction of the energetic ions such as the alpha particles and the NBI-generated fast ions including the birth profiles and the Coulomb collisions using the F3D-OFMC code [27]. The quantitative evaluation of the finite beta effects on target energetic ion losses will greatly help to design the fusion reactors that can confine energetic ions successfully. However, there is a problem about the VMEC calculation. Since the flux coordinates are used in the VMEC, the calculation region is limited only in the plasma region. The equilibrium magnetic field between the plasma boundary and the first wall is required to quantitatively evaluate the energetic ion losses. Therefore, this problem should be resolved in the next chapter.

Chapter 5

Development of field calculation method in the vacuum region using the VMEC results

For the orbit calculation, the MHD equilibrium field should be calculated by a MHD calculation code. The full 3D MHD equilibria can be easily obtained by the VMEC code. However, the calculation region is limited to the inside plasma region because the flux coordinates are used in this code. The MHD equilibrium magnetic field between the plasma boundary and the first wall is required to quantitatively evaluate the energetic ion losses. The field calculation code, which is based on the Biot-Savart law using the VMEC results, is developed. The details of the method and results are described in this study. This paper was published in Plasma Science and Technology 15 115 (2013) [28].

5.1 Introduction

The VMEC code is one of the 3D, free boundary MHD equilibrium calculation code and it has been ordinary used in a helical plasma [10][11]. In these days, the VMEC code is used also in the rippled tokamaks [8][9][29]. The full 3D MHD equilibria can be easily obtained by the VMEC code, while the calculation region is limited to the inside plasma region because the flux coordinates are used in this code. In the result, the loss power fraction and the loss position of the energetic ions could not be accurately evaluated. The equilibrium field consists of the magnetic fields from the external coil current and the plasma equilibrium current. If the plasma is assumed to be a kind of coils, the equilibrium field can be calculated from every coil shape and every coil current by using the Biot-Savart law. The equilibrium field calculation code, which is based on this idea, is developed in this study. The separatrix structures and the heat loads on the wall can be analyzed with this code.

In Sec. 5.2, the field calculation code is precisely explained. In Sec. 5.3, the 3D magnetic configuration, which is obtained by this code, is analyzed. Finally, the summaries and conclusions are described in Sec. 5.4.

5.2 Details of the developed calculation code

The equilibrium field can be calculated inside the plasma by the VMEC code in the flux coordinates (s, θ, ζ), where s, θ and ζ are the normalized toroidal magnetic flux, the poloidal angle and the toroidal angle, respectively. The toroidal angle ζ of the flux coordinates is consistent with the toroidal angle ϕ of the cylindrical coordinates (R, Z, ϕ).

5.2.1 Inverse-Mapping for the inside plasma region

Inside the plasma, the equilibrium field in the flux coordinates is transformed to that in the cylindrical coordinates by the Inverse-Mapping method [30]. The components of the position vector (R, Z, ϕ) in the VMEC can be written as,

$$R(s,\theta,\zeta) = \sum_{\mathrm{mn}} [R^{\mathrm{c}}_{\mathrm{mn}}(s)\cos(\mathrm{m}\theta - \mathrm{n}\zeta) + R^{\mathrm{s}}_{\mathrm{mn}}(s)\sin(\mathrm{m}\theta - \mathrm{n}\zeta)] \tag{5.1}$$

$$Z(s,\theta,\zeta) = \sum_{\mathrm{mn}} [Z^{\mathrm{c}}_{\mathrm{mn}}(s)\cos(\mathrm{m}\theta - \mathrm{n}\zeta) + Z^{\mathrm{s}}_{\mathrm{mn}}(s)\sin(\mathrm{m}\theta - \mathrm{n}\zeta)] \tag{5.2}$$

$$\phi(s,\theta,\zeta) = \zeta. \tag{5.3}$$

Since the cylindrical coordinates (R, Z, ϕ) are independent, the Taylor-expanding of R and Z about the initial guess (s^0, θ^0, ϕ) can be written as below,

$$R(s,\theta,\zeta) = R^0 + R^0_{\mathrm{s}}(s - s_0) + R^0_\theta(\theta - \theta_0) + O_R(\Delta^2) \tag{5.4}$$

$$Z(s,\theta,\zeta) = Z^0 + Z^0_{\mathrm{s}}(s - s_0) + Z^0_\theta(\theta - \theta_0) + O_Z(\Delta^2) \tag{5.5}$$

Where,

$$\begin{aligned}
R^0 &= R(s^0,\theta^0,\zeta) \\
Z^0 &= Z(s^0,\theta^0,\zeta) \\
R^0_{\mathrm{s}} &= \left.\frac{\partial R}{\partial s}\right|_{(s^0,\theta^0,\zeta)} \\
R^0_\theta &= \left.\frac{\partial R}{\partial \theta}\right|_{(s^0,\theta^0,\zeta)} \\
Z^0_{\mathrm{s}} &= \left.\frac{\partial Z}{\partial s}\right|_{(s^0,\theta^0,\zeta)} \\
Z^0_\theta &= \left.\frac{\partial Z}{\partial \theta}\right|_{(s^0,\theta^0,\zeta)}.
\end{aligned}$$

Therefore, the solution can be written as below,

$$s(R,Z,\phi) = s^0 + \frac{R^0_\theta(Z-Z^0) - Z^0_\theta(R-R^0)}{\tau^0} + O_{\rm s}(\Delta^2) \tag{5.6}$$

$$\theta(R,Z,\phi) = \theta^0 + \frac{Z^0_{\rm s}(R-R^0) - R^0_\theta(Z-Z^0)}{\tau^0} + O_\theta(\Delta^2) \tag{5.7}$$

where

$$\begin{aligned} s^0 &= s(R^0,Z^0,\phi) \\ \theta^0 &= \theta(R^0,Z^0,\phi) \\ \tau^0 &= R^0_\theta Z^0_{\rm s} - R^0_{\rm s} Z^0_\theta. \end{aligned}$$

s^1 and θ^1 are defined as the solution using the initial guess (s^0,θ^0,ϕ) without the second order error term $O(\Delta^2)$,

$$s^1 = s^0 + \frac{R^0_\theta(Z-Z^0) - Z^0_\theta(R-R^0)}{\tau^0} \tag{5.8}$$

$$\theta^1 = \theta^0 + \frac{Z^0_{\rm s}(R-R^0) - R^0_\theta(Z-Z^0)}{\tau^0} \tag{5.9}$$

Moreover, by using (s^1,θ^1,ϕ), the solution (s^2,θ^2,ζ) can be obtained. These equations are generalized as below,

$$s^{\rm k} = s^{k-1} + \frac{R^{k-1}_\theta(Z-Z^{k-1}) - Z^{k-1}_\theta(R-R^{k-1})}{\tau^{k-1}} \tag{5.10}$$

$$\theta^{\rm k} = \theta^{k-1} + \frac{Z^{k-1}_{\rm s}(R-R^{k-1}) - R^{k-1}_\theta(Z-Z^{k-1})}{\tau^{k-1}} \tag{5.11}$$

If these equations are solved until the first order error terms $(s^{\rm k}-s^{k-1})$ and $(\theta^{\rm k}-\theta^{k-1})$ become sufficiently small, the solution (s,θ,ζ) for given (R,Z,ϕ) can be obtained. Since the equilibrium magnetic field can be written in VMEC as below,

$$\begin{aligned} \boldsymbol{B}(R,Z,\phi) &= \boldsymbol{B}(s^{\rm k},\theta^{\rm k},\zeta) \\ &= \sum_{\rm mn} \left[\boldsymbol{B}^{\rm c}_{\rm mn}(s^{\rm k})\cos({\rm m}\theta^{\rm k}-{\rm n}\zeta) + \boldsymbol{B}^{\rm s}_{\rm mn}(s^{\rm k})({\rm m}\theta^{\rm k}-{\rm n}\zeta)\right] \end{aligned} \tag{5.12}$$

the equilibrium magnetic field can be obtained inside the plasma region by the Inverse-Mapping method.

5.2.2 Biot-Savart method for the outside plasma region

This section shows the method of the calculation of the equilibrium field $\boldsymbol{B}$ in the vacuum region using the VMEC results. According to the Biot-Savart law, the current density in

a plasma $\boldsymbol{j}_{\rm pl}$ produces the magnetic field on the certain position $\boldsymbol{r}$,

$$\boldsymbol{B}^{\rm pl}(\boldsymbol{r}) = \mu_0 \iiint_V \frac{\boldsymbol{j}_{\rm pl}(\boldsymbol{r}^{'}) \times (\boldsymbol{r} - \boldsymbol{r}^{'})}{4\pi|\boldsymbol{r} - \boldsymbol{r}^{'}|^3} {\rm d}\boldsymbol{r}^{'}. \tag{5.13}$$

In the VMEC, the current density is written as the flux coordinates (s, θ, ζ),

$$\boldsymbol{j}_{\rm pl} = j^{\theta}_{\rm pl} \nabla\zeta \times \nabla s + j^{\zeta}_{\rm pl} \nabla s \times \nabla\theta. \tag{5.14}$$

The current density can be written in the Cartesian coordinates (X, Y, Z),

$$\begin{aligned} j_{\rm pl}(X) &= \boldsymbol{j}_{\rm pl} \cdot \nabla X \\ &= \boldsymbol{j}_{\rm pl} \cdot \left(\frac{\partial X}{\partial s}\nabla s + \frac{\partial X}{\partial \theta}\nabla\theta + \frac{\partial X}{\partial \zeta}\nabla\zeta \right) \\ &= \frac{1}{\sqrt{g}} \left(j^{\theta}_{\rm pl}\frac{\partial X}{\partial \theta} + j^{\zeta}_{\rm pl}\frac{\partial X}{\partial \zeta} \right) \\ &= \frac{1}{\sqrt{g}} \left(j^{\theta}_{\rm pl} X_{\theta} + j^{\zeta}_{\rm pl} X_{\zeta} \right), \end{aligned} \tag{5.15}$$

where $\sqrt{g}$ is the Jacobian in the flux coordinates (s, θ, ζ). The Y and Z components of $\boldsymbol{j}_{\rm pl}$ can be similarly obtained as,

$$\begin{aligned} j_{\rm pl}(Y) &= \frac{1}{\sqrt{g}} \left(j^{\theta}_{\rm pl} Y_{\theta} + j^{\zeta}_{\rm pl} Y_{\zeta} \right) \\ j_{\rm pl}(Z) &= \frac{1}{\sqrt{g}} \left(j^{\theta}_{\rm pl} Z_{\theta} + j^{\zeta}_{\rm pl} Z_{\zeta} \right). \end{aligned}$$

Therefore, the X component of the $\boldsymbol{B}^{\rm pl}$ can be written as,

$$\begin{aligned} B^{\rm pl}(X) &= \frac{\mu_0}{4\pi} \iiint_V \frac{j_{\rm pl}(Y^{'})(Z - Z^{'}) - j_{\rm pl}(Z^{'})(Y - Y^{'})}{\left((X - X^{'})^2 + (Y - Y^{'})^2 + (Z - Z^{'})^2\right)^{3/2}} {\rm d}\boldsymbol{r}^{'} \\ &= \frac{\mu_0}{4\pi} \iiint_V \frac{\left(j^{\theta}_{\rm pl} Y^{'}_{\theta} + j^{\zeta}_{\rm pl} Y^{'}_{\zeta} \right)(Z - Z^{'}) - \left(j^{\theta}_{\rm pl} Z^{'}_{\theta} + j^{\zeta}_{\rm pl} Z^{'}_{\zeta} \right)(Y - Y^{'})}{\left((X - X^{'})^2 + (Y - Y^{'})^2 + (Z - Z^{'})^2\right)^{3/2}} {\rm d}s{\rm d}\theta{\rm d}\zeta. \end{aligned}$$

As well as the $B^{\rm pl}(X)$, the Y and Z components of $\boldsymbol{B}^{\rm pl}$ can be written as,

$$\begin{aligned} B^{\rm pl}(Y) &= \frac{\mu_0}{4\pi} \iiint_V \frac{\left(j^{\theta}_{\rm pl} Z^{'}_{\theta} + j^{\zeta}_{\rm pl} Z^{'}_{\zeta} \right)(X - X^{'}) - \left(j^{\theta}_{\rm pl} X^{'}_{\theta} + j^{\zeta}_{\rm pl} X^{'}_{\zeta} \right)(Z - Z^{'})}{\left((X - X^{'})^2 + (Y - Y^{'})^2 + (Z - Z^{'})^2\right)^{3/2}} {\rm d}s{\rm d}\theta{\rm d}\zeta \\ B^{\rm pl}(Z) &= \frac{\mu_0}{4\pi} \iiint_V \frac{\left(j^{\theta}_{\rm pl} X^{'}_{\theta} + j^{\zeta}_{\rm pl} X^{'}_{\zeta} \right)(Y - Y^{'}) - \left(j^{\theta}_{\rm pl} Y^{'}_{\theta} + j^{\zeta}_{\rm pl} Y^{'}_{\zeta} \right)(X - X^{'})}{\left((X - X^{'})^2 + (Y - Y^{'})^2 + (Z - Z^{'})^2\right)^{3/2}} {\rm d}s{\rm d}\theta{\rm d}\zeta. \end{aligned}$$

The components of the position vector (R, Z) in the VMEC can be written as Eq.(5.1) and Eq.(5.2). In the VMEC, ζ in the flux coordinates equals to the ϕ in the cylindrical coordinates. Therefore, the components of the position vector (X, Y, Z) can be written as,

$$
\begin{aligned}
X(s,\theta,\zeta) &= \sum_{\mathrm{mn}} \left[R^{\mathrm{c}}_{\mathrm{mn}}(s)\cos(\mathrm{m}\theta - \mathrm{n}\zeta) + R^{\mathrm{s}}_{\mathrm{mn}}(s)\sin(\mathrm{m}\theta - \mathrm{n}\zeta)\right]\cos\zeta \qquad (5.16)\\
Y(s,\theta,\zeta) &= \sum_{\mathrm{mn}} \left[Z^{\mathrm{c}}_{\mathrm{mn}}(s)\cos(\mathrm{m}\theta - \mathrm{n}\zeta) + Z^{\mathrm{s}}_{\mathrm{mn}}(s)\sin(\mathrm{m}\theta - \mathrm{n}\zeta)\right]\sin\zeta \qquad (5.17)\\
Z(s,\theta,\zeta) &= \sum_{\mathrm{mn}} \left[Z^{\mathrm{c}}_{\mathrm{mn}}(s)\cos(\mathrm{m}\theta - \mathrm{n}\zeta) + Z^{\mathrm{s}}_{\mathrm{mn}}(s)\sin(\mathrm{m}\theta - \mathrm{n}\zeta)\right].
\end{aligned}
$$

Therefore, the partial differentiation of (X, Y, Z) with respect to θ and ζ can be written as,

$$
\begin{aligned}
X_\theta &= \frac{\partial R}{\partial \theta}\cos\zeta \qquad (5.18)\\
X_\zeta &= \frac{\partial R}{\partial \zeta}\cos\zeta - R\sin\zeta \qquad (5.19)\\
Y_\theta &= \frac{\partial R}{\partial \theta}\sin\zeta \qquad (5.20)\\
Y_\zeta &= \frac{\partial R}{\partial \zeta}\sin\zeta + R\cos\zeta \qquad (5.21)\\
Z_\theta &= \frac{\partial Z}{\partial \theta} \qquad (5.22)\\
Z_\zeta &= \frac{\partial Z}{\partial \zeta}. \qquad (5.23)
\end{aligned}
$$

Where, the partial differentiation of (R, Z) with respect to θ and ζ can be written as,

$$
\begin{aligned}
\frac{\partial R}{\partial \theta} &= \sum_{\mathrm{mn}} m\{-R^{\mathrm{c}}_{\mathrm{mn}}(s)\sin(\mathrm{m}\theta - \mathrm{n}\zeta) + R^{\mathrm{s}}_{\mathrm{mn}}(s)\cos(\mathrm{m}\theta - \mathrm{n}\zeta)\} \qquad (5.24)\\
\frac{\partial R}{\partial \zeta} &= \sum_{\mathrm{mn}} n\{R^{\mathrm{c}}_{\mathrm{mn}}(s)\sin(\mathrm{m}\theta - \mathrm{n}\zeta) - R^{\mathrm{s}}_{\mathrm{mn}}(s)\cos(\mathrm{m}\theta - \mathrm{n}\zeta)\} \qquad (5.25)\\
\frac{\partial Z}{\partial \theta} &= \sum_{\mathrm{mn}} m\{-Z^{\mathrm{c}}_{\mathrm{mn}}(s)\sin(\mathrm{m}\theta - \mathrm{n}\zeta) + Z^{\mathrm{s}}_{\mathrm{mn}}(s)\cos(\mathrm{m}\theta - \mathrm{n}\zeta)\} \qquad (5.26)\\
\frac{\partial Z}{\partial \zeta} &= \sum_{\mathrm{mn}} n\{Z^{\mathrm{c}}_{\mathrm{mn}}(s)\sin(\mathrm{m}\theta - \mathrm{n}\zeta) - Z^{\mathrm{s}}_{\mathrm{mn}}(s)\cos(\mathrm{m}\theta - \mathrm{n}\zeta)\}. \qquad (5.27)
\end{aligned}
$$

Therefore, the components of the magnetic field $B^{\mathrm{pl}}(X)$, $B^{\mathrm{pl}}(Y)$ and $B^{\mathrm{pl}}(Z)$ can be obtained. These magnetic field components can be written in the cylindrical coordinates

as,

$$B^{\mathrm{pl}}(R) = B^{\mathrm{pl}}(X)\cos\phi + B^{\mathrm{pl}}(Y)\sin\phi \tag{5.28}$$

$$B^{\mathrm{pl}}(\phi) = -B^{\mathrm{pl}}(X)\sin\phi + B^{\mathrm{pl}}(Y)\cos\phi. \tag{5.29}$$

To obtain the equilibrium field $\boldsymbol{B}(\boldsymbol{r})$, the vacuum field vector $\boldsymbol{B}^{\mathrm{ext}}(\boldsymbol{r})$, which is generated by the external coil current density $\boldsymbol{j}^{\mathrm{i}}_{\mathbf{c}}(\boldsymbol{r}')$, should be superimposed on $\boldsymbol{B}^{\mathrm{pl}}(\boldsymbol{r})$,

$$\begin{aligned}\boldsymbol{B}(\boldsymbol{r}) &= \boldsymbol{B}^{\mathrm{pl}}(\boldsymbol{r}) + \boldsymbol{B}^{\mathrm{ext}}(\boldsymbol{r}) \\ &= \boldsymbol{B}^{\mathrm{pl}}(\boldsymbol{r}) + \mu_0 \sum_{\mathrm{i}=1}^{N} \iiint_{C_{\mathrm{i}}} \frac{\boldsymbol{j}^{\mathrm{i}}_{\mathbf{c}}(\boldsymbol{r}'_{\mathrm{i}}) \times (\boldsymbol{r} - \boldsymbol{r}'_{\mathrm{i}})}{4\pi|\boldsymbol{r} - \boldsymbol{r}'_{\mathrm{i}}|^3} \mathrm{d}V_{\mathrm{i}}.\end{aligned} \tag{5.30}$$

5.3 Calculation accuracy of developed code

The magnetic field components which are obtained by both calculation methods on the plasma boundary are compared in this section. In this study, the calculation model is referred by the 9MA scenario of an ITER operation. The volume-averaged beta value is set to 2% which is same as the original ITER operation [8][13]. Figure 5.1 (a) and (b) show the relative error of each field component $\Delta B_R/|B|$, $\Delta B_Z/|B|$ and $\Delta B_{\mathrm{tor}}/|B|$ on the plasma boundary between the results from the VMEC code and the developed field calculation code along the poloidal angle θ at $\phi = 0$ and along the toroidal angle ϕ at $\theta = 0$, respectively. Although the calculation error appear in these figures, the maximum relative error is only approximately 0.2%. Therefore, the developed field calculation code has high enough numerical accuracy. In this case, the normalized toroidal magnetic flux s, the poloidal angle θ and the toroidal angle θ is divided to 40, 360 and 720, respectively. To obtain the field structures, a lot of computational time and resources are required. Therefore, the equilibrium field is obtained by the Inverse-Mapping method inside the plasma and calculated by the Biot-Savart law outside the plasma.

5.4 Summary

In this study, the VMEC code is used to analyze the non-axisymmetric finite beta effect. However, the equilibrium field could not be calculated inside the plasma because the flux coordinates are used. The field calculation code, which is based on the Biot-Savart law, is developed. The magnetic field configuration, which obtained by this method, is compared to the VMEC result and the maximum relative error is less than 0.3%. This calculation method can help us to quantitatively evaluate the energetic ion losses using the VMEC results in the next chapter.

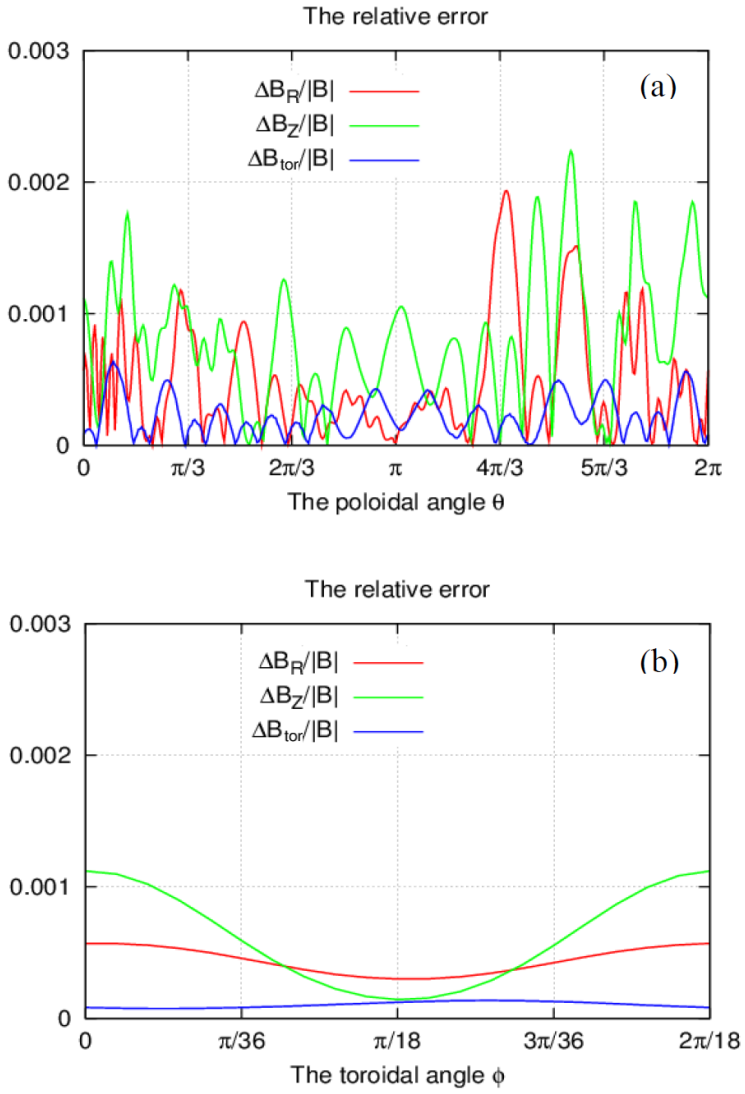

Figure 5.1: The relative error of each field component between the results from the VMEC code and the developed field calculation code on the plasma boundary (a) along the poloidal angle θ at $\phi = 0$ and (b) along the toroidal angle ϕ at $\theta = 0$

Chapter 6

Quantitative evaluation of finite beta effects on alpha particle losses

In tokamak plasmas, the confinement of energetic ions depends on the magnetic field structure. If the plasma pressure is finite, the equilibrium current (i.e., the Pfirsch-Schlüter current and diamagnetic current) flows in the plasma to maintain the MHD equilibrium. These plasma currents generate the poloidal and toroidal magnetic field component and alter the field structure. Moreover, if the TF ripples are taken into account in the MHD equilibrium calculation, the non-axisymmetric component of the equilibrium current can alter the TF ripples themselves. When the plasma beta becomes high, the changes in the field structure due to the equilibrium current might affect the confinement of energetic ions significantly. We intend to clarify how these currents alter the field structure and affect the confinement of alpha particles in high-beta plasmas. The MHD equilibrium is calculated using the VMEC code and the orbits of fusion alpha particles are followed by using the fully three-dimensional magnetic field orbit-following Monte Carlo code. In relatively low-beta plasmas (e.g., the volume-averaged beta value $\langle\beta\rangle \leq 2\%$), the changes in the magnetic field component due to the plasma current negligibly affect the confinement of the alpha particles except for the Shafranov shift effect. However for $\langle\beta\rangle \geq 3\%$, the diamagnetic effect reduces the magnetic field strength and significantly increases alpha particle losses. In these high-beta cases, the non-axisymmetric field component generated by the equilibrium current also increases these losses, but not as effectively as compared to the diamagnetic effect. This paper was published in Physics of Plasmas 20 (2013) 082511 [31].

6.1 Introduction

In Chapter 4, the several kinds of finite beta effects on the energetic ion losses were clarified. However, the finite beta effects on the energetic ion losses could not be quantitatively evaluated because the equilibrium field could not be calculated in the vacuum region using

the VMEC. Due to the calculation tool which was introduced in Chapter 5, the 3D MHD equilibrium field was obtained not only in the plasma region, but also in the vacuum region. By using this 3D field, the fully 3D magnetic field orbit-following Monte-Carlo (F3D-OFMC) code can be used [27]. Since this code is widely used in the field of the energetic ion confinement, it possess higher reliability. In this study, the non-axisymmetric field component $\widetilde{\boldsymbol{B}}^{\mathrm{pl}}$ and the toroidal field component of the 2D MHD equilibrium field $\langle \boldsymbol{B} \rangle_{\mathrm{tor}}^{\mathrm{pl}}$ are focused on. Moreover, the finite beta effects should be clarified not only on the energetic ion losses, but also on the heat loads on the wall. This research can help to design the prospective nuclear fusion reactor.

The remainder of the paper is organized as follows. Sec. 6.2 introduces the calculation model and the calculation code. Sec. 6.3 shows the results of the orbit calculations for the fusion alpha particles. Sec. 6.4 describes the mechanism of the finite beta effects of the energetic ion losses. Finally, Sec. 6.5 summarizes the findings and conclusions of this study.

6.2 Research method

In this study, the calculation model is referred by the 9MA scenario of an ITER operation. The MHD equilibrium is calculated using the VMEC code. For the outside of the plasma, the magnetic field is calculated using the Biot-Savart law which were introduced in the previous chapter [28]. The volume-averaged beta value $\langle \beta \rangle$ is changed from 0% to about 7%. The beta values are shown in Table 6.1. When $\langle \beta \rangle = 7\%$, β_N corresponds to 10 for the tokamak model in this study. Since this value exceeds the Troyon limit, it is unrealistic to achieve such high-beta plasmas used in this calculation. However, the high-beta plasma whose $\langle \beta \rangle$ exceeds 5%, which is desirable for the economical reasons, can be achieved in the low-aspect-ratio tokamaks such as the spherical tokamak (ST). Since the MHD equilibrium current depends on $\langle \beta \rangle$, knowledge obtained in this study can be applied to such a stable high-beta tokamak.

To quantitatively evaluate how equilibrium current alters the field structure and affects the energetic ion losses, the orbits of the energetic ions are calculated for the following three magnetic fields:

(i) $\boldsymbol{B}^{(\mathrm{i})} \equiv \boldsymbol{B}_{3\mathrm{D}} = \langle \boldsymbol{B} \rangle + \widetilde{\boldsymbol{B}} = \langle \boldsymbol{B} \rangle + \widetilde{\boldsymbol{B}}^{\mathrm{ext}} + \widetilde{\boldsymbol{B}}^{\mathrm{pl}} = \langle \boldsymbol{B} \rangle_{\mathrm{pol}} + R \langle B \rangle_{\mathrm{tor}} \nabla\phi + \widetilde{\boldsymbol{B}}^{\mathrm{ext}} + \widetilde{\boldsymbol{B}}^{\mathrm{pl}}$

In this case, the magnetic field structure obtained from the full 3D MHD equilibrium with VMEC is used in the orbit calculation.

(ii) $\boldsymbol{B}^{(\mathrm{ii})} = \langle \boldsymbol{B} \rangle + \widetilde{\boldsymbol{B}}^{\mathrm{ext}} = \langle \boldsymbol{B} \rangle_{\mathrm{pol}} + \langle \boldsymbol{B} \rangle_{\mathrm{tor}} + \widetilde{\boldsymbol{B}}^{\mathrm{ext}} = \langle \boldsymbol{B} \rangle_{\mathrm{pol}} + R \langle B \rangle_{\mathrm{tor}} \nabla\phi + \widetilde{\boldsymbol{B}}^{\mathrm{ext}}$

This case corresponds to the vacuum approximation, where the non-axisymmetric component of the external field $\widetilde{\boldsymbol{B}}^{\mathrm{ext}}$ is superimposed on the axisymmetric MHD equilibrium field $\langle \boldsymbol{B} \rangle$. In this study, $\widetilde{\boldsymbol{B}}^{\mathrm{ext}}$ is defined as $\boldsymbol{B}^{\mathrm{ext}} - \langle \boldsymbol{B} \rangle^{\mathrm{ext}}$, where $\boldsymbol{B}^{\mathrm{ext}}$

is the external magnetic field including the TF ripples. The $\langle \boldsymbol{B} \rangle$ is calculated using VMEC with the axisymmetric condition and can be expressed as follows:

$$\begin{aligned} \langle \boldsymbol{B} \rangle &= \langle \boldsymbol{B} \rangle_{\rm pol} + \langle \boldsymbol{B} \rangle_{\rm tor} \\ &= \frac{1}{2\pi} \nabla\Psi \times \nabla\phi + f(\Psi)\nabla\phi, \end{aligned}$$

where Ψ is the poloidal magnetic flux and $f(\Psi)$ is the flux surface quantity, which is defined as $f(\Psi) = R \langle B \rangle_{\rm tor}$. If we compare $\boldsymbol{B}^{\rm (i)}$ and $\boldsymbol{B}^{\rm (ii)}$, $\widetilde{\boldsymbol{B}}^{\rm pl}$ is missing in $\boldsymbol{B}^{\rm (ii)}$.

(iii) $\boldsymbol{B}^{\rm (iii)} = \langle \boldsymbol{B} \rangle_{\rm pol} + \langle \boldsymbol{B} \rangle_{\rm tor}^{\rm ext} + \widetilde{\boldsymbol{B}}^{\rm ext} = \langle \boldsymbol{B} \rangle_{\rm pol} + R_0 B_0 \nabla\phi + \widetilde{\boldsymbol{B}}^{\rm ext}$

When it is compared to $\boldsymbol{B}^{\rm (ii)}$, $\langle \boldsymbol{B} \rangle_{\rm tor} = f(\Psi)\nabla\phi = R \langle B \rangle_{\rm tor} \nabla\phi$ is approximated by $R_0 B_0 \nabla\phi$, where $B_0 =$ constant is the external toroidal field at an arbitrary radius R_0. If we define $\Psi^{\rm pl}$ as the poloidal flux produced by the current in the plasma, $\boldsymbol{B}^{\rm (iii)}$ can also be expressed as follows:

$$\boldsymbol{B}^{\rm (iii)} = \frac{1}{2\pi} \Psi^{\rm pl} \times \nabla\phi + \boldsymbol{B}^{\rm ext}.$$

Since $f(\Psi) \approx R_0 B_0$ is a good approximation for low-beta plasmas, it is frequently used in the orbit calculation of the energetic ions in the rippled tokamaks. In this approximation, the toroidal magnetic field component $\langle \boldsymbol{B} \rangle_{\rm tor}^{\rm pl}$, mainly generated by the diamagnetic current is ignored. However, since the changes in $f(\Psi)$ from $R_0 B_0$ can not be neglected in high-beta plasmas, the influence of this effect will be evaluated.

By calculating and comparing the fusion alpha particle losses among three cases mentioned above, Case (i), Case (ii) and Case (iii) (i.e., $\boldsymbol{B}^{\rm (i)}$, $\boldsymbol{B}^{\rm (ii)}$ and $\boldsymbol{B}^{\rm (iii)}$), how the changes in field structure affect the confinement of alpha particles can be evaluated. For three magnetic field models, 10,000 fusion alpha particle orbits are followed using the F3D-OFMC code [27]. In this code, the guiding center orbits can be calculated by considering the slowing down and the pitch angle scattering processes. If the particles reach the first wall before the reduction of the kinetic energy to the thermal energy due to Coulomb collisions, they are assumed to be lost. The birth profile of the fusion alpha particles depends on the plasma pressure. Due to the Shafranov shift, the radial position of the magnetic axis moves to the outboard side of the torus. Therefore, the birth points of the fusion alpha particles also move to the out board side on increasing the plasma beta. The same birth profiles are used for the three cases if the beta value of the plasma is the same.

6.3 Fusion alpha particle losses

To evaluate the fusion alpha particle losses, the loss power fraction ϵ is introduced in this study. The loss power fraction is defined by the ratio of the total kinetic energy of the all

Table 6.1: The beta values in this calculation

$\langle\beta\rangle$ [%]	$\beta_{\rm t}$	$\beta_{\rm N}$
0.60	0.0061	0.848
1.26	0.0127	1.764
2.02	0.0204	2.839
2.79	0.0282	3.910
3.54	0.0358	4.975
4.35	0.0440	6.112
5.18	0.0524	7.279
6.02	0.0609	8.454
6.77	0.0686	9.524
7.56	0.0767	10.65

lost particles to the total initial energy of the all particles. Figure 6.1 shows the averaged value of ϵ for the fusion alpha particles. The blue, green and red cross symbols show ϵ for Cases (i), (ii) and (iii), respectively. For $\langle\beta\rangle = 2.02$, 6.77, and 7.56% plasma, the orbit calculations are performed five times with the different random numbers determining the initial conditions for the Monte-Carlo calculations. For example, Table 6.2 shows the average, the dispersion and the standard deviation of ϵ for Case (i) in $\langle\beta\rangle = 6.77\%$. The standard deviation consistent with the error bar in Fig. 6.1. The solid circles of each color present the averaged value of ϵ, while the error bars show the standard deviation of it. Figure 6.2 shows the ϵ for the collisionless orbit. In this case, the particles are assumed to be lost when the guiding center reaches the plasma boundary, unless the tracing time exceeds 0.01 s, in which case they are assumed to be non-loss particles. Although the magnitude of ϵ is different between Fig. 6.1 and Fig. 6.2, the shape of the curved line and the relationships for Case (i), (ii), and (iii) are similar. Therefore, the difference of the results is not caused by the Coulomb collisions, but caused by the finite beta effects.

The loss power fraction is the largest for Case (i) and the smallest for Case (iii) at the same beta plasma, meaning that both the non-axisymmetric field component, $\widetilde{\boldsymbol{B}}^{\rm pl}$, and the toroidal magnetic field component generated by the equilibrium plasma current, $\langle\boldsymbol{B}\rangle^{\rm pl}_{\rm tor}$, increase the fusion alpha particle losses. First, $\widetilde{\boldsymbol{B}}^{\rm pl}$ is discussed. With increasing the plasma beta, the difference between ϵ for Cases (i) and (ii) increases, but still remains small in sufficiently high-beta plasmas. For example, for $\langle\beta\rangle = 6.77\%$, ϵ is increased by approximately 0.0052 because of $\widetilde{\boldsymbol{B}}^{\rm pl}$ (i.e., approximately 5% increase in comparison with that for Case (i)). Since this difference is larger than the respective error bar, $\widetilde{\boldsymbol{B}}^{\rm pl}$ causes ϵ to increase.

Second, $\langle\boldsymbol{B}\rangle^{\rm pl}_{\rm tor}$ is discussed. The loss power fraction for Case (ii) is larger than that for Case (iii), and therefore, $\langle\boldsymbol{B}\rangle^{\rm pl}_{\rm tor}$ increases ϵ. For the normal operation in an ITER

plasma, $\langle\beta\rangle$ is planned to be about 2%. Since there is no significant difference between ϵ in Cases (ii) and (iii) at this plasma beta, $\langle \boldsymbol{B} \rangle_{\rm tor}^{\rm pl}$ negligibly affects the energetic ion losses in the low-beta plasmas. However, on increasing the plasma beta, this difference also increases, but it is gradually saturated above $\langle\beta\rangle = 7\%$. In the high-beta plasmas, ϵ is most strongly increased by $\langle \boldsymbol{B} \rangle_{\rm tor}^{\rm pl}$. Therefore, the changes in the field structure due to $\langle \boldsymbol{B} \rangle_{\rm tor}^{\rm pl}$ could not be ignored for energetic ion losses in the plasma with $\langle\beta\rangle \geq 3\%$.

The effect of the poloidal field due to the equilibrium plasma current should be mentioned. The Shafranov shift effect increases the fusion alpha particle losses because the generation points of the fusion alpha particles are moved to the outboard side of the torus [22]. On increasing the plasma beta, ϵ for Case (iii) also increases until $\langle\beta\rangle = 6\%$. The loss fraction ϵ for $\langle\beta\rangle = 6\%$ is three times bigger than that for $\langle\beta\rangle = 0.5\%$. Over this beta value, ϵ does not increase evidently because the amount of the magnetic axis shift becomes smaller as the plasma beta increases. Moreover, the strong poloidal field is needed to fix the safety-factor profile and the shape of the plasma boundary in the high-beta plasmas. Because this field reduces the ripple ratio in the outboard side of the torus, ϵ is gradually reduced at $\langle\beta\rangle = 6\%$ for Case (iii) [20].

The loss power fraction for Case (iii) is reduced not only by the decrease of δ but also by the other factors. The Shafranov shift also affects the toroidal precession rate, $w_{\rm D}$, of the trapped particles. Due to the Shafranov shift effect, $w_{\rm D}$ is reduced and the energetic ion losses might be decreased [32]. Moreover, the width of the banana orbit is squeezed by the strong poloidal field in the outboard side of the torus [17]. Although the first-orbit losses of the alpha particles are not so effective in this case, this orbit squeezing effect might reduce these losses. It is quite difficult to qualitatively evaluate these effects on the energetic ion losses in this study. If it is possible, the more simple tokamak models should be used (e.g., up-down symmetric tokamak).

6.4 Effect of plasma current on energetic ion losses

6.4.1 Non-axisymmetric field component $\widetilde{\boldsymbol{B}}^{\rm pl}$

Figure 6.3(a) shows the difference between the ripple ratio for Cases (i) and (ii) (i.e., $\delta(\boldsymbol{B}^{\rm (i)})$ and $\delta(\boldsymbol{B}^{\rm (ii)})$) at $\langle\beta\rangle = 6.77\%$. It shows that $\widetilde{\boldsymbol{B}}^{\rm pl}$ increases δ throughout the plasma and increases by 0.0004 at maximum. On the contrary, this non-axisymmetric field component increases the loss power fraction ϵ by 0.0052 (i.e., an approximately 5% increase in comparison with Case (i)). It means that $\widetilde{\boldsymbol{B}}^{\rm pl}$ does not strongly affect ϵ. Under the condition of this study, in which the maximum $\delta_{\rm vac}$ is approximately 0.01 in plasma, vacuum approximation can also be used for $\langle\beta\rangle = 7\%$. Therefore, the conclusion in reference [8] can be confirmed even for the high-beta plasmas unless the ripple ratio is sufficiently small.

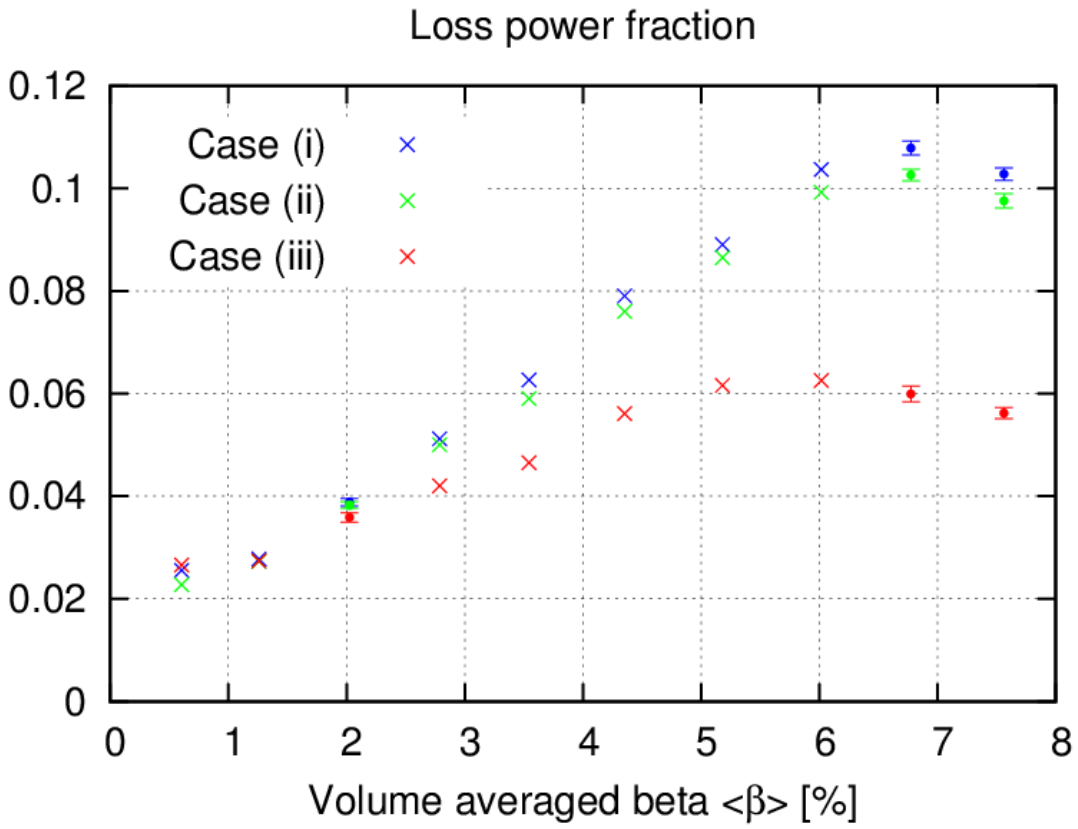

Figure 6.1: The loss power fraction ϵ for Cases (i), (ii) and (iii) are represented by the blue, green and red cross symbols, respectively. For $\langle\beta\rangle = 2.02$, 6.77, and 7.56%, the solid circles of each color indicate the averaged value of ϵ and the error bars show the standard deviation of ϵ.

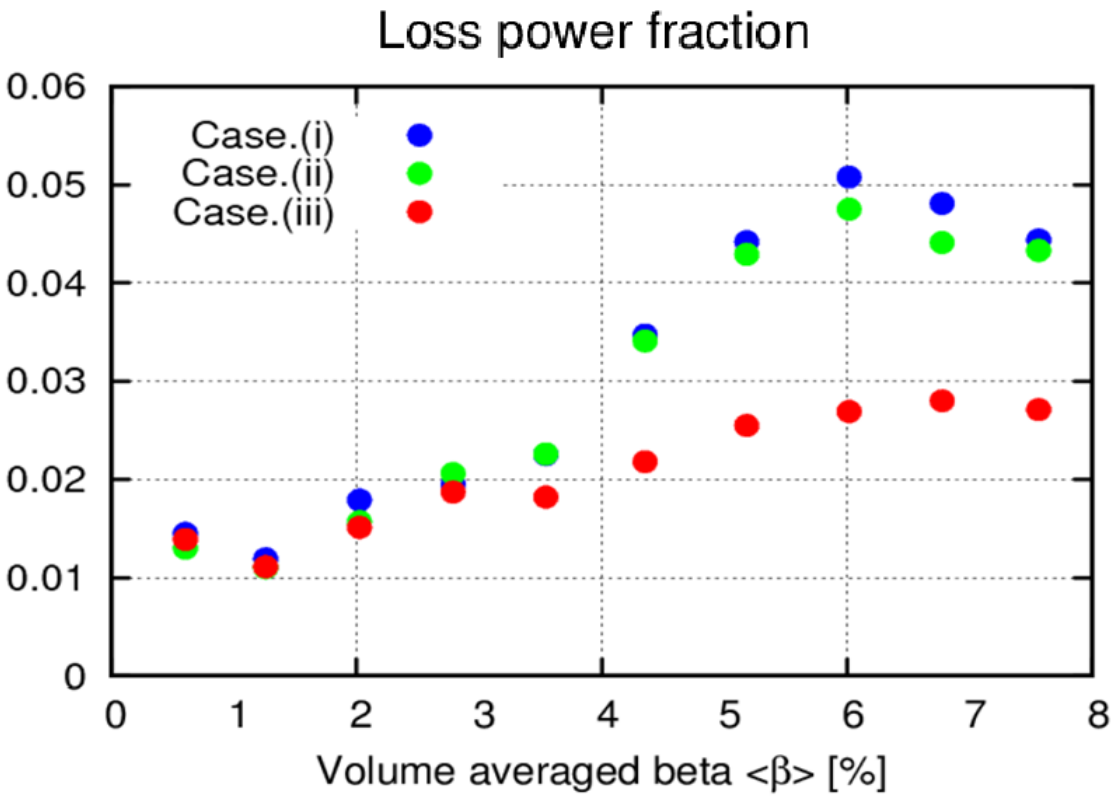

Figure 6.2: The loss power fraction ϵ for the collisionless orbit

Table 6.2: The error bar of ϵ for Case (i) in $\langle\beta\rangle = 6.77\%$

Random seed	Loss power fraction ε	(ε-<ε>)^0.5
0	0.1100	4.48E-06
1	0.1087	7.71E-07
2	0.1065	1.87E-06
3	0.1066	1.66E-06
4	0.1075	1.13E-07
Average <ε>	0.1078	
Dispersion	1.78E-06	
Standard deviation	0.001334	

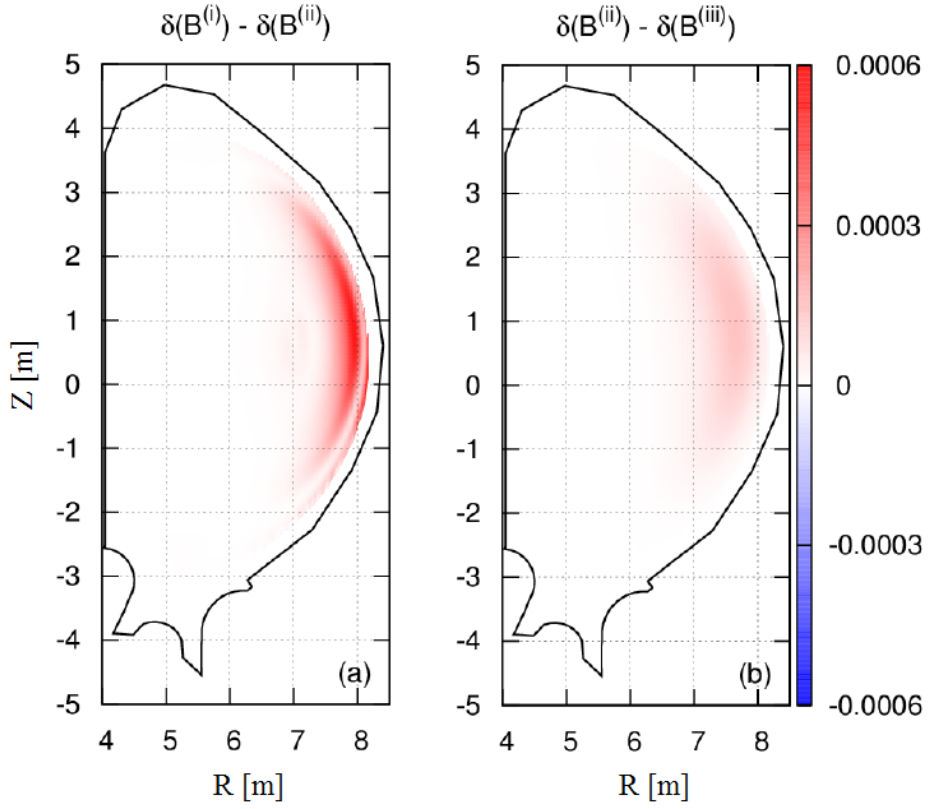

Figure 6.3: The difference of the ripple ratio at $\langle\beta\rangle = 6.77\%$ (a) $\delta(\boldsymbol{B}^{(\mathrm{i})}) - \delta(\boldsymbol{B}^{(\mathrm{ii})})$ and (b) $\delta(\boldsymbol{B}^{(\mathrm{ii})}) - \delta(\boldsymbol{B}^{(\mathrm{iii})})$.

6.4.2 Toroidal field component $\langle \boldsymbol{B} \rangle_{\rm tor}^{\rm pl}$

Figure 6.3(b) shows the difference between the ripple ratio for Cases (ii) and (iii) (i.e., $\delta(\boldsymbol{B}^{(\rm ii)})$ and $\delta(\boldsymbol{B}^{(\rm iii)})$) at $\langle\beta\rangle = 6.77\%$. Not only the non-axisymmetric field component but also the axisymmetric field component alters δ [9][20]. At $(R, Z) = (7.6\ \text{m}, 0.5\ \text{m})$, $\langle \boldsymbol{B} \rangle_{\rm tor}^{\rm pl}$ maximally increases δ by 0.0001. This value is negligible, but ϵ is doubled at $\langle\beta\rangle = 6.77\%$. Therefore, there should be another factor including the increase of ϵ.

The diamagnetic current reduces the external toroidal field and alters the field strength $|B|$ contour line; this effect is known as the diamagnetic effect. Figures 6.4(a) and (b) show the $|B|$ contour line at $\phi = 0$ for $\boldsymbol{B}^{(\rm ii)}$ and $\boldsymbol{B}^{(\rm iii)}$ at $\langle\beta\rangle = 6.77\%$, respectively. Because of the diamagnetic effect, the $|B|$ contour line is bent and the closed $|B|$ contour region appears in the outboard side of the torus. If the reflection point of a trapped energetic ion is located in this region, it is not lost because $|B|$ at the subsequent bounce points is constant and banana tips of the orbit of this particle should be always on the same closed $|B|$ contour line [20]. This means that $\langle \boldsymbol{B} \rangle_{\rm tor}^{\rm pl}$ reduces the number of the lost particles whose banana tips are in the closed $|B|$ contour region. Figures 6.5 show the collisionless orbit of a particle which trapped at $(R, Z, \phi) = (7.3\ \text{m}, 1.1\ \text{m}, 0)$ (i.e., the green circle). The trapped points and the orbit are described by the blue dots and the red line, respectively. For Case (ii), since the particle is trapped in the closed $|B|$ contour region, the trapped points describe the closed path. As the result, the particles does not lose even if the tracing time exceeds 5[ms]. While for Case (iii), a particle reaches at the first wall in the relatively short time (i.e., 0.5[ms]).

In contrast, if the bounce position of a trapped particle is not in the closed $|B|$ contour region, its orbit is strongly affected by this contour line bending effect [20]. The $|B|$ contour line for Case (ii) is highly bent in the outboard side of the torus in comparison with Case (iii). Since the energetic ions bounce at the same $|B|$ contour line, the trapped particles can more easily move to the outboard side of the torus (i.e., the high $\delta_{\rm vac}$ region) for such a shape of the $|B|$ contour line. As same as Figures 6.5, Figures 6.6 show the collisionless orbit of a particle which trapped at $(R, Z, \phi) = (7.2\ \text{m}, 1.9\ \text{m}, 0)$. At this point, the $|B|$ contour line for Case (ii) is strongly bent when it is compared to that for Case (iii). As the result, the particle for Case (ii) reaches at the wall in 5[ms], but the particle for Case (iii) does not lose.

As shown above, the bending of $|B|$ contour line due to the diamagnetic effect causes the increase of the trapped particle losses. However, once the $|B|$ contour line is closed, the loss of the trapped particles whose banana tips are in the closed $|B|$ contour region decreases. Since the closed $|B|$ contour line can appear at $\langle\beta\rangle \geq 5\%$ and this region is limited to a quite narrow area, its effect on the particle loss is not substantial. As a result, $\langle \boldsymbol{B} \rangle_{\rm tor}^{\rm pl}$, which represents the diamagnetic effect, increases the energetic ion losses in the high-beta plasmas as shown in Figs. 6.1.

The diamagnetic effect alters the magnetic field structure, the $|B|$ contour line and the bounce points of a banana particle. The loss of a banana particle depends on the bounce

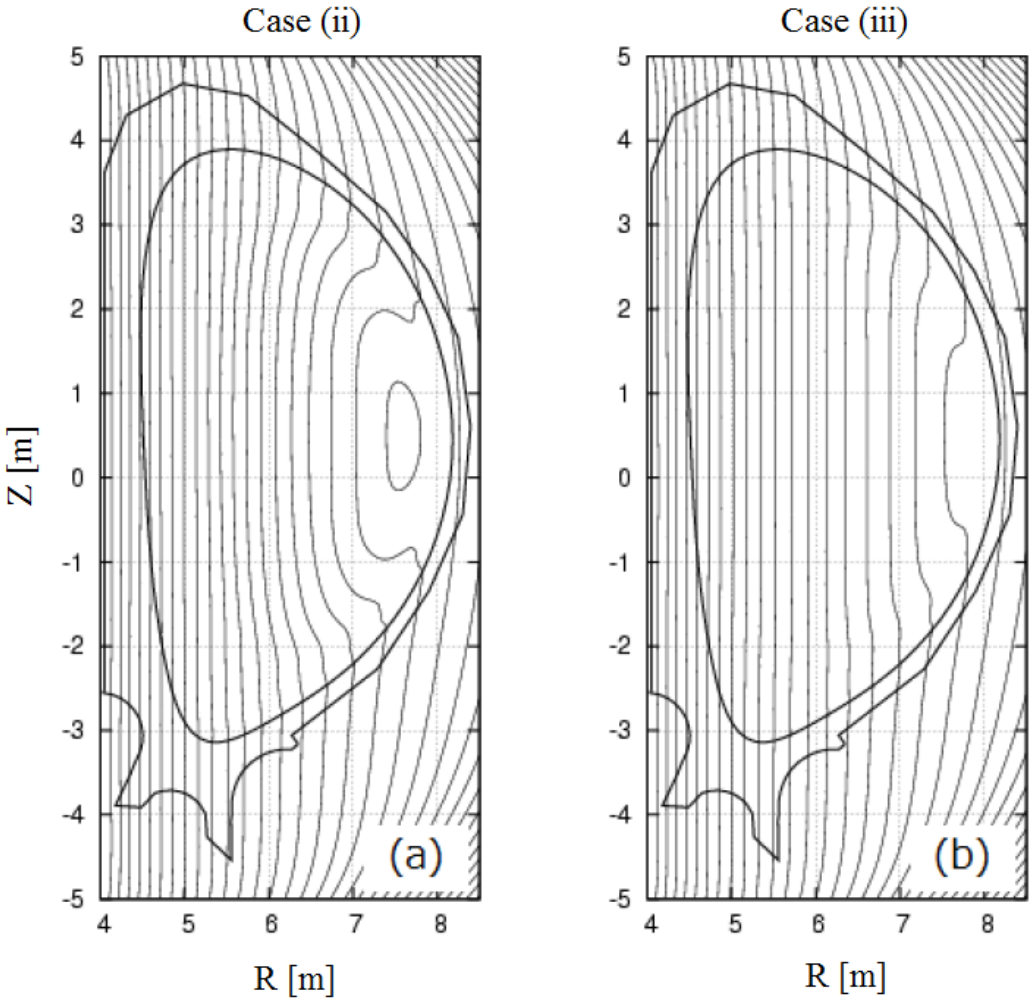

Figure 6.4: The field strength $|B|$ contour line at $\phi = 0$ for (a) Case (ii) and (b) Case (iii)

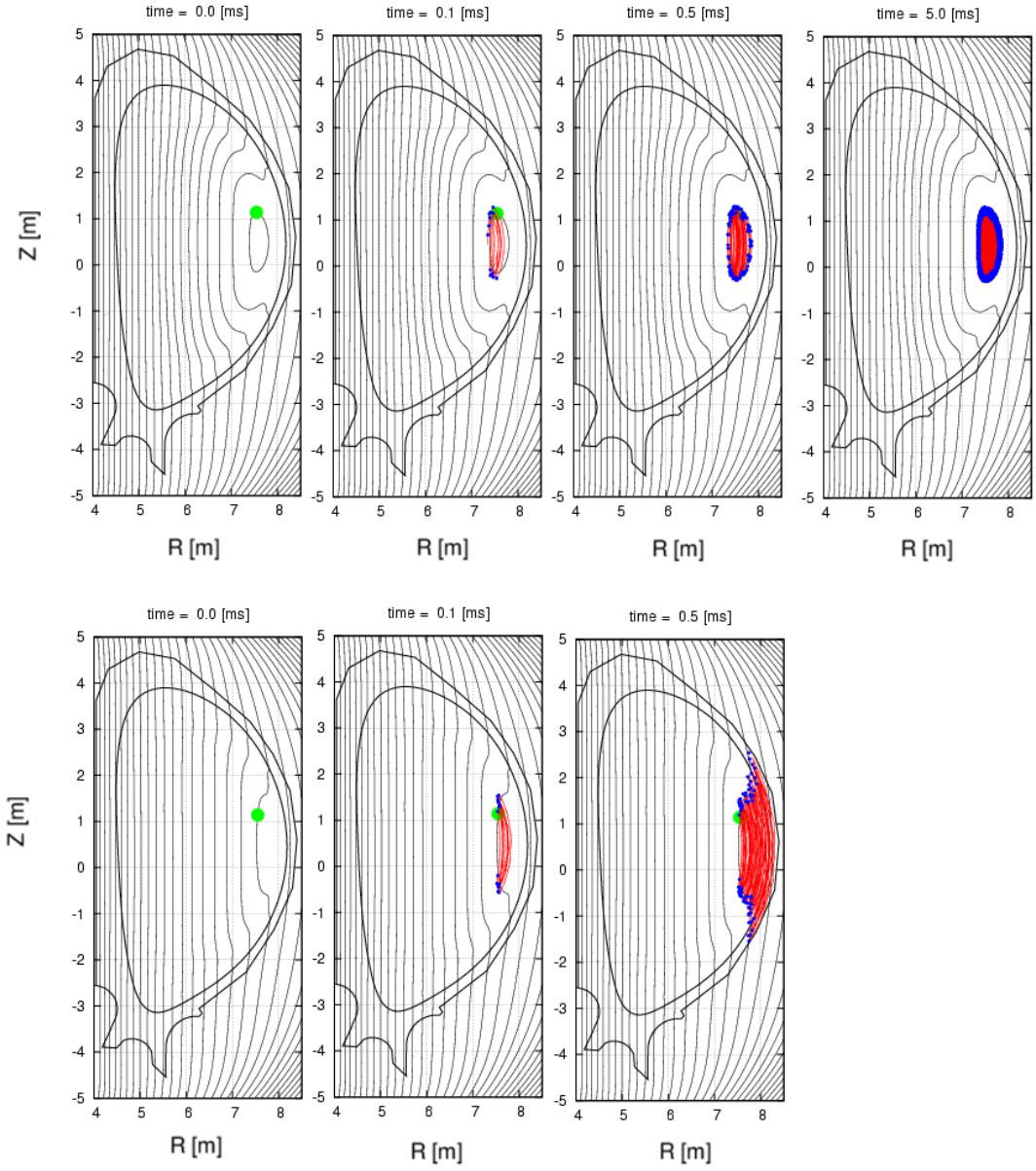

Figure 6.5: The orbit of a banana particle is shown by the red line and the trapped point is described by the blue dots, starting from the green circle $(R, Z, \phi) = (7.3\ \mathrm{m}, 1.1\ \mathrm{m}, 0)$ with a pitch angle $\lambda = \pi/2$ for Case (ii) and Case (iii)

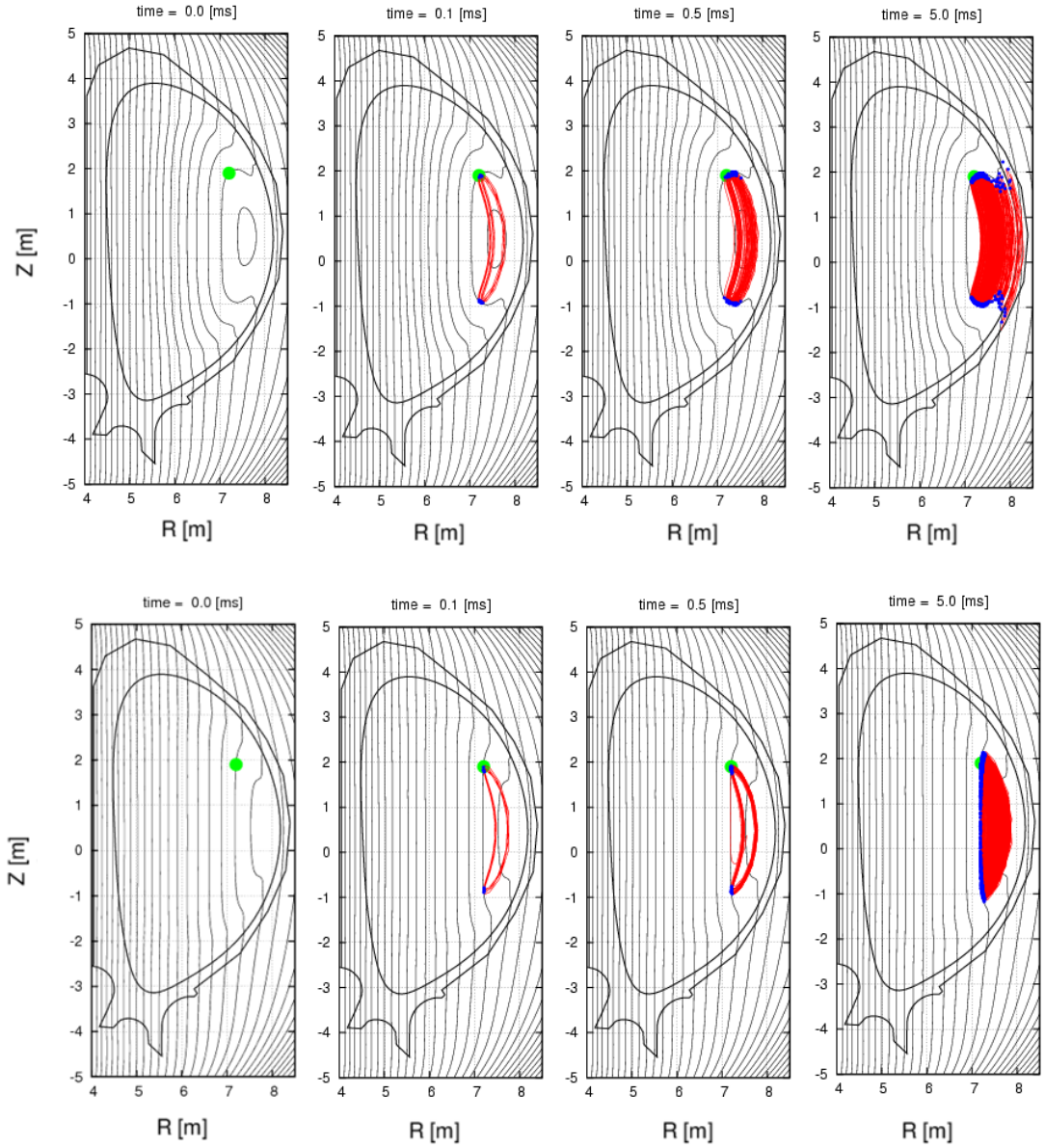

Figure 6.6: The orbit of a banana particle is shown by the red line and the trapped point is described by the blue dots, starting from the green circle $(R, Z, \phi) = (7.2\ \text{m}, 1.9\ \text{m}, 0)$ with a pitch angle $\lambda = \pi/2$ for Case (ii) and Case (iii)

points; therefore, we intend to clarify how the diamagnetic effect changes the energetic ion losses by following the orbits of the trapped ions. The color depth in Figs. 6.7 shows the orbit tracing time of the alpha particles having the initial position (R, Z). The initial positions (R, Z) are distributed over the plasma, while the initial toroidal angle ϕ is fixed at $\pi/18$. The alpha particles orbits are followed with a pitch angle $\lambda = \pi/2$ (i.e., with no parallel velocity at the initial position). To clearly estimate the effect of $\langle \boldsymbol{B} \rangle^{\rm pl}_{\rm tor}$, in this calculation the collisions are ignored (i.e., the magnetic moment and the initial energy are conserved). If the particles reach the first wall before the orbit tracing time exceeds 0.01 s, they are assumed to be lost. These orbits are followed for Cases (ii) and (iii) at $\langle \beta \rangle = 6.77\%$.

If a banana particle is trapped in the closed $|B|$ contour area, it is not lost for the collisionless case, while it may be lost if it is trapped further inside the plasma because of the $|B|$ contour line bending effect. In this beta plasma, the position of the magnetic axis locates at $(R, Z) = (7.0\ \text{m}, 0.5\ \text{m})$. Since the generation points of the alpha particles depend on the magnetic axis, in this case, the $|B|$ contour line bending effect on the alpha particle losses is much stronger than the closed $|B|$ contour effect. Moreover, in a sufficiently high-beta plasma (e.g., $\langle \beta \rangle = 10\%$), $\langle \boldsymbol{B} \rangle^{\rm pl}_{\rm tor}$ might reduce ϵ because of the closed $|B|$ contour effect.

6.5 Heat loads

Figures 6.8 show the heat loads of fusion alpha particles [W/m^2], where the vertical and horizontal axes represent the vertical position Z m and the toroidal angle ϕ, respectively. According to the previous report [13], the heat loads depend on the wall shape. In this study, the 2D wall shape shown in Fig. 1.4(c) is used for all field models in all beta plasmas. In the low-beta plasmas, the difference of the heat loads among three magnetic fields is negligible. On the contrary, in the high-beta plasmas, the heat loads are quite different for Cases (ii) and (iii). The heat loads are increased and a hot spot appear in $Z = -1$ m (i.e. Zone A in Fig.6.8 (e)). Figures 6.9 show the $|B|$ contour line at $\phi = 0$ for Case (ii) and (iii), respectively. Because of the diamagnetic effect, the $|B|$ contour line is bent in the outboard side of the torus. Figure 6.9(c) only shows the $|B|$ contour which passes $(R, Z, \phi) = (7.2\ \text{m}, 1.9\ \text{m}, 0)$ for Case (ii) and (iii). The $|B|$ contour line for Case (iii) contacts with the wall at $Z = -2.2$ m, while that for Case (ii) contacts at $Z = -1.5$ m. Since the trapped points follow the $|B|$ contour line, most of alpha particles are lost in Zone A in Fig.6.8 (e).

In this paragraph, the histograms of the ratio of the lost particles $N_{\rm Loss}$ and all test particles $N_{\rm all}$ are shown. The blue, green, and red bar graph show $N_{\rm Loss}/N_{\rm All}$ in $\langle \beta \rangle = 6.77\%$ for Case (i), Case (ii), and Case (iii), respectively. The horizontal axis in Figures 6.10 represent energy for the lost particles and that in Figures 6.11 represent the pitch angle λ in Eq. (4.7) on the lost point. Because of the diamagnetic effect, the number of

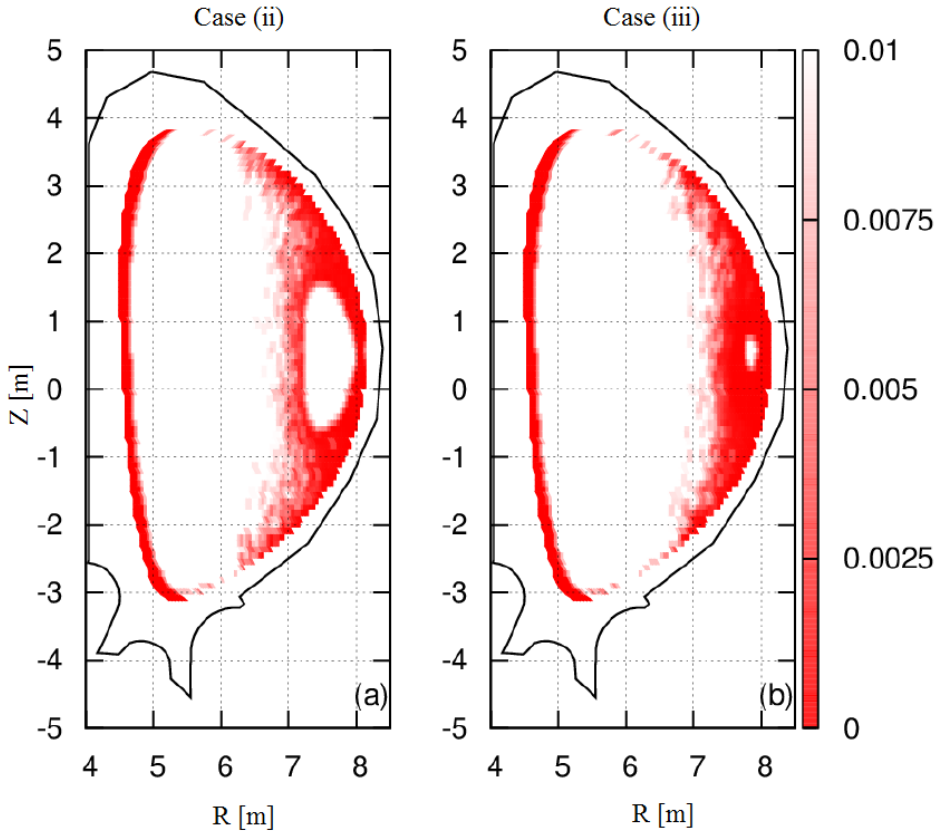

Figure 6.7: Color depth shows the orbit tracing time [s] for alpha particles at the initial position (R, Z). These particles started their motion from $\phi = \pi/18$ with no parallel velocity. Figures (a) and (b) show the results for Case (ii) and (iii) at $\langle\beta\rangle = 6.77\%$, respectively.

lost particles which have over 3MeV is increased. The N_{Loss} of high energetic particles for Case (ii) becomes approximately twice when it is compared to that for Case (iii). These particles mainly consist of the trapped particles $\lambda \sim 0.5$ in Figures 6.11. Due to the $|B|$ contour line bending effect, the trapped particles are promptly lost when they are generated in the outside of the torus. These prompt lost particles produce the Zone A as shown in Fig.6.8 (e). The effects of the non-axisymmetric plasma current is not effective for the heat loads. While, the diamagnetic effect can produce the heat spot in the high-beta plasmas and this effect should not be ignored for the analysis of the energetic ion losses.

6.6 Summary

Plasma currents flow to keep the MHD equilibrium. These currents generate the poloidal and toroidal fields and alter the magnetic field structure. These changes also affect the confinement of the energetic ions. In this study, we clarified how the equilibrium current changes the field structure and affects energetic ion losses. It is found that the non-axisymmetric field component $\widetilde{\boldsymbol{B}}^{\mathrm{pl}}$ and the toroidal field component $\langle \boldsymbol{B} \rangle^{\mathrm{pl}}_{\mathrm{tor}}$, which is mainly produced by the diamagnetic current, increase the fusion alpha particle losses and that the magnitude of these effects depends on the plasma beta.

The effect of $\widetilde{\boldsymbol{B}}^{\mathrm{pl}}$ is not prominent in this study. Even in the high-beta plasma $\langle \beta \rangle = 6.77\%$, it increases the loss power fraction ϵ by approximately 0.0052 (i.e., approximately 5% increase compared with that for Case (i)). Therefore, the vacuum approximation can be used under the conditions of this study in which the maximum δ_{vac} is approximately 0.01 in plasma. The conclusions of a previous study [8] can be confirmed by calculating the orbits of fusion alpha particles actually. However, if the number of TFCs is reduced or if the optional coils such as the edge localized mode mitigation coils are installed, the non-axisymmetry of the magnetic field may be increased. This means that the non-axisymmetry of the plasma current will also be increased. Therefore, the effect of $\widetilde{\boldsymbol{B}}^{\mathrm{pl}}$ on the alpha particle losses for such reactors should be evaluated carefully.

The $\langle \boldsymbol{B} \rangle^{\mathrm{pl}}_{\mathrm{tor}}$, which is mainly due to the diamagnetic effect, negligibly affects the energetic ion losses for $\langle \beta \rangle \leq 2\%$. However, the $|B|$ contour line is significantly bent over this beta value, thus producing two opposing effects: 1) the reduction of the energetic ion losses due to the closed $|B|$ contour and 2) increase of these losses due to the $|B|$ contour line bending effect. The latter is normally stronger than the former for fusion alpha particles; for example, when $\langle \beta \rangle = 6.77\%$, ϵ is doubled by $\langle \boldsymbol{B} \rangle^{\mathrm{pl}}_{\mathrm{tor}}$. Therefore, the changes in field structure due to the diamagnetic effect could not be ignored for the energetic ion losses corresponding to the $\langle \beta \rangle \geq 3\%$ plasma. Because of the diamagnetic effect, the $|B|$ contour line intersects with the reactor wall near the center of the Z axis. Therefore, the heat spot shifts above the Z-axis in this study.

It is well known that the Shafranov shift changes the birth profile of the alpha particles

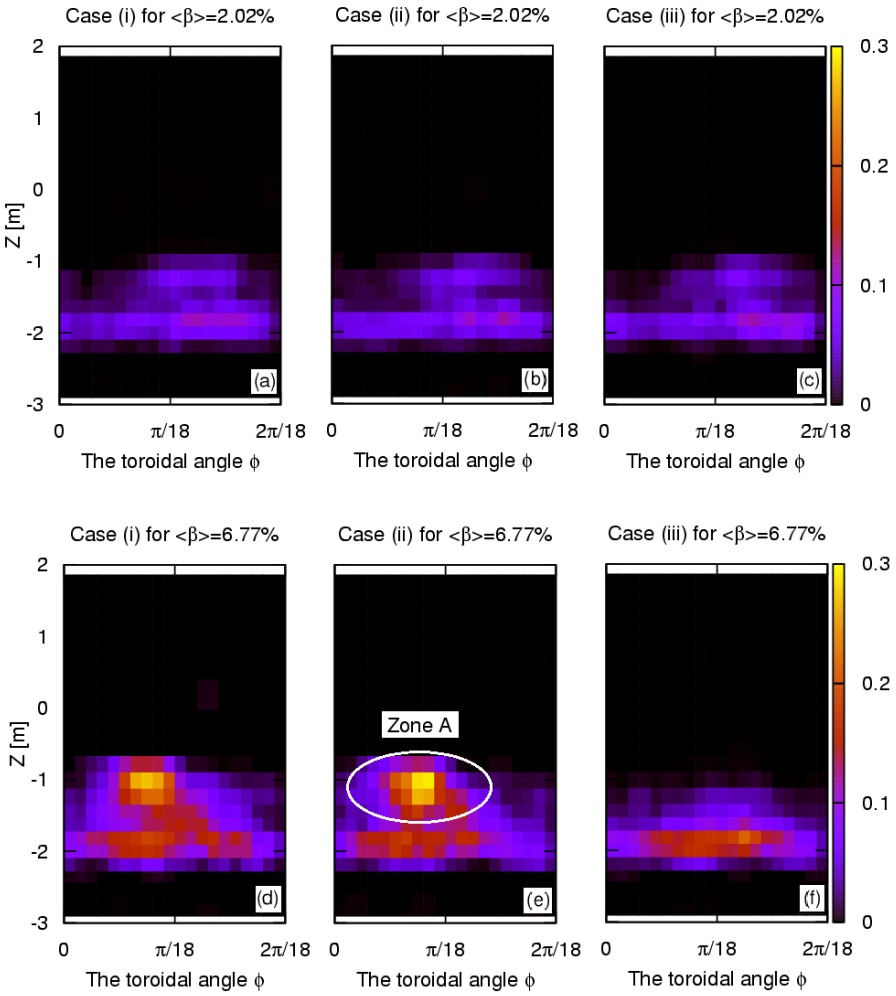

Figure 6.8: The heat loads of the fusion alpha particles [W/m^2].

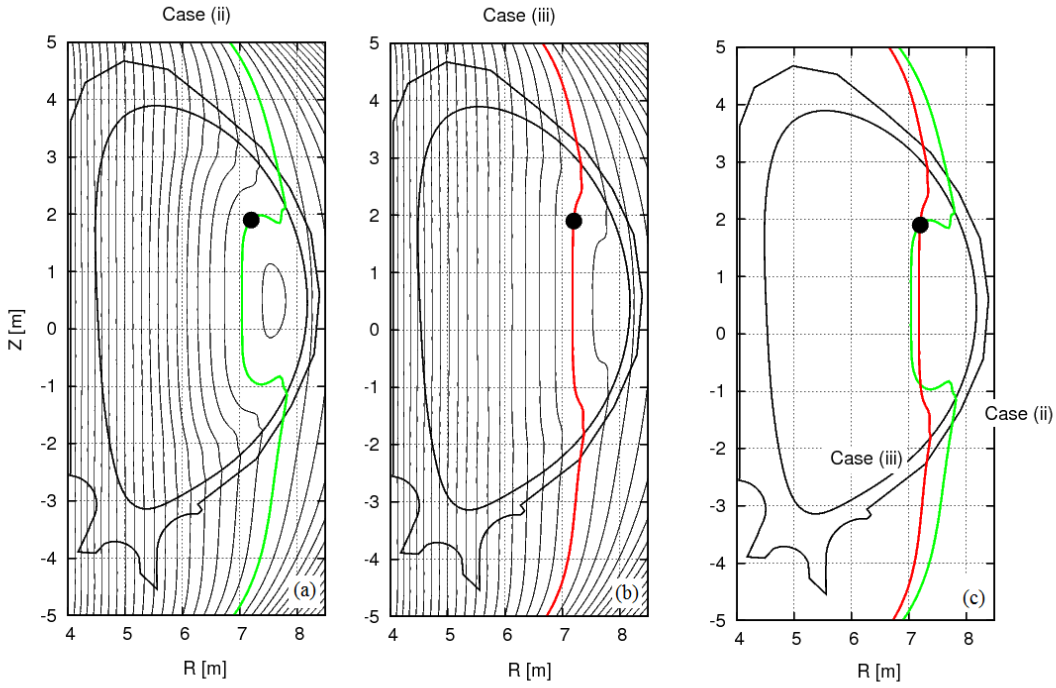

Figure 6.9: Figures (a) and (b) show the $|B|$ contour line at $\phi = 0$ for Case (ii) and (iii), respectively. The red and green line in Fig. (c) show the $|B|$ contour for Case (ii) and (iii) which passes $(R, Z, \phi) = (7.2\ \mathrm{m}, 1.9\ \mathrm{m}, 0)$ (the black circle).

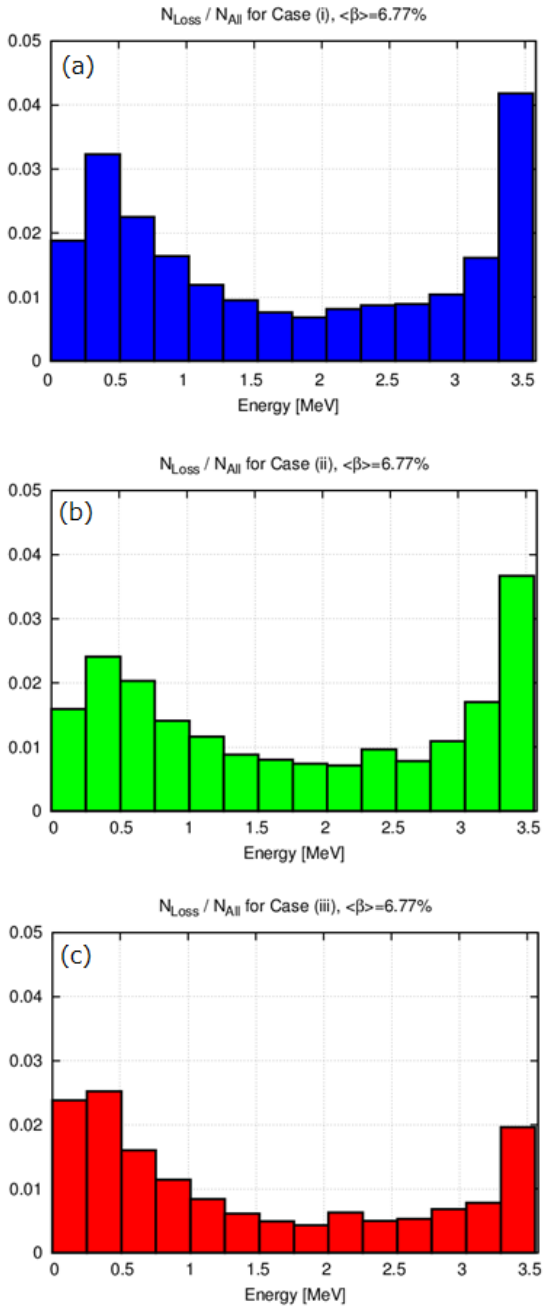

Figure 6.10: $N_{\mathrm{Loss}}/N_{\mathrm{All}}$ against the energy for the lost particles in $\langle\beta\rangle = 6.77\%$ for Case (i), Case (ii), and Case (iii), respectively.

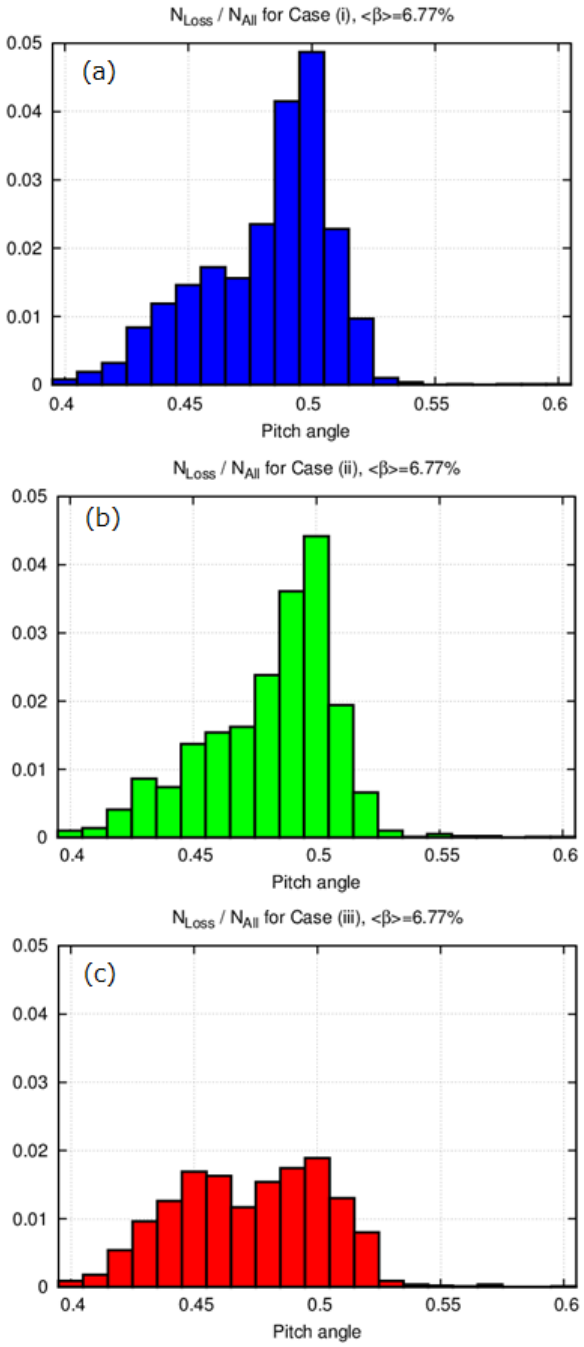

Figure 6.11: $N_{\rm Loss}/N_{\rm All}$ against the pitch angle λ on the lost point in $\langle\beta\rangle = 6.77\%$ for Case (i), Case (ii), and Case (iii), respectively.

and affects their losses. Since the fusion alpha particles are generated at the further outer torus (i.e., the high δ_{vac} region) because of the Shafranov shift, the fusion alpha particles are more strongly affected by the TF ripples. In this study, ϵ at $\langle\beta\rangle = 6\%$ is three times larger than that at $\langle\beta\rangle = 0.5\%$.

The Shafranov effects on the toroidal precession and the orbit squeezing effect of the strong poloidal field could not be fully discussed . Although these effects might reduce the energetic ion losses, these effects on energetic ion losses could not be quantitatively evaluated in this study. To analyze precisely, the more simple tokamak models should be used (e.g., up-down symmetric tokamak).

Following the fusion alpha particles orbits, several effects of the equilibrium current on both the magnetic field structure and the energetic ion losses were clarified. The magnitude of each effect depends on the plasma beta $\langle\beta\rangle$ and the engineering design of the device, such as the aspect ratio and the number of TFCs. The loss power fraction was most strongly increased by the diamagnetic effect in the high-beta plasmas, but this relation might be different in other high δ_{vac} tokamak plasmas. Moreover, it is unrealistic to achieve the high-beta plasmas such as $\langle\beta\rangle = 7\%$ under the conditions of this study. On the other hand, in the low-aspect-ratio tokamaks such as STs, it is not difficult to attain such high-beta plasma. In future work, we intend to clarify how the equilibrium current changes the magnetic field structure and affects the energetic ion losses in other tokamaks such as STs and high δ_{vac} tokamaks.

Chapter 7

Conclusion

The energetic ion losses in the rippled tokamaks are studied in this thesis. The finite beta effects alter the magnetic field structure and the energetic ion losses. The physical mechanism of the finite beta effects should be clarified especially in the high-beta rippled tokamaks. This research can be separated by two parts: the MHD equilibrium calculation and the orbit calculation. Firstly, the MHD equilibrium should be calculated to clarify the finite beta effects on the field structure. Secondly, the orbit calculation should be performed using the MHD equilibrium field. By changing the beta values in an ITER-like plasma, the several kinds of the finite beta effects on the energetic ion losses are clarified in this study.

In Chapter 4, the finite beta effects on the magnetic field structure and the orbits of the energetic ions are clarified. The finite beta effects on the ripple ratio δ are categorized by two parts: the axisymmetric and the non-axisymmetric finite beta effects. In the center of a plasma, both effects increase δ. While, the axisymmetric finite beta effect decreases it at the outer torus. The decrease of δ by the axisymmetric finite beta effect is strongly larger than the increase of it by the non-axisymmetric finite beta effect. Therefore, the finite beta effects increase δ in the center of a plasma and decrease it at outer torus. The diamagnetic effect reduces the field strength $|B|$ and alter the field contour structure. It significantly bends the $|B|$ contour line in a high-beta plasma and produces two opposing effects: 1) the reduction of the energetic ion losses due to the closed $|B|$ contour and 2) increase of these losses due to the $|B|$ contour line bending effect.

In Chapter 5, the problem of the VMEC code about the calculation region is resolved. The full 3D MHD equilibria can be easily obtained by the VMEC code, while the calculation region is limited to the inside plasma region because the flux coordinates are used in this code. However, the equilibrium magnetic field between the plasma boundary and the first wall is required to quantitatively evaluate the energetic ion losses. The field calculation code, which is based on the Biot-Savart law using the VMEC results, is developed. The computation accuracy of the field component obtained by this method is sufficiently high; it is less than 0.3 % in the plasma boundary.

In Chapter 6, the finite beta effects on the energetic ion losses are quantitatively evaluated. The MHD equilibrium is calculated using the VMEC code and the orbits of fusion alpha particles are followed by using the F3D-OFMC code. In $\langle\beta\rangle \leq 2\%$, the changes in the magnetic field component due to the plasma current negligibly affect the confinement of the alpha particles except for the Shafranov shift effect. However for $\langle\beta\rangle \geq 3\%$, the diamagnetic effect reduces the $|B|$ and significantly increases the alpha particle losses. The diamagnetic effect produces two opposing effects: 1) the reduction of energetic ion losses due to the closed $|B|$ contour and 2) increase of these losses due to the $|B|$ contour line bending effect. For the fusion alpha particles, the diamagnetic effect usually increases the energetic ion losses. The increase of the lost particles is induced by the high-energetic trapped particles. Because of the diamagnetic effect, the $|B|$ contour line intersects with the reactor wall near the center of the Z axis. Therefore, the heat spot shifts above the Z-axis in this study. In these high-beta cases, the non-axisymmetric field component generated by the equilibrium current also increases these losses, but not as effectively as compared to the diamagnetic effect.

In this paper, an ITER-like plasma configuration is used as the calculation model. However, the strength of each finite beta effect on the energetic ion losses might be changed if the number of the TFCs is reduced, the local ferrite materials are installed, the aspect ratio is altered, and the target energetic ions are changed. Therefore, the energetic ion losses should be analyzed for these tokamak configurations carefully. Moreover, the HINT code should be used instead of the VMEC in order to clarify the effect of the magnetic island and the stochasticity of the flux surfaces on the energetic ion losses.

Finally, the summary of the important results in this study are briefly shown by a run of the item.

1. The problems of the VMEC code about the calculation region are resolved by using the Biot-Savart law.

2. The important finite beta effects on the energetic ion losses consist of the Shafranov shift effect, the changes of the ripple ratio δ, and the diamagnetic effect.

3. Although the Shafranov shift effect increases the energetic ion losses as beta increases, the rate of the increase becomes slower in a high-beta plasma.

4. In the center of a plasma, the both axisymmetric and non-axisymmetric finite beta effects increase δ. While, the axisymmetric finite beta effect decreases it at the outer torus. Totally, the finite beta effects increase δ in the center of a plasma and decrease it at the outer torus.

5. Although the non-axisymmetric finite beta effect increases the energetic ion losses, it is not so effective for the ITER-like configuration. Under the conditions of this

research, the loss power fraction ϵ is increased by five percent due to the non-axisymmetric finite beta effect for $\langle\beta\rangle = 7\%$.

6. For the ITER-like configurations, the $|B|$ contour can be closed for $\langle\beta\rangle = 5\%$ because of the diamagnetic effect.

7. The diamagnetic effect produces two kinds of effects on the energetic ion losses: 1) the reduction of the energetic ion losses due to the closed $|B|$ contour and 2) increase of these losses due to the $|B|$ contour line bending effect.

8. For the fusion alpha particles, the diamagnetic effect usually increases the high-energetic trapped ion losses.

9. Because of the diamagnetic effect, the $|B|$ contour line intersects with the reactor wall near the center of the Z axis. Therefore, the heat spot shifts above the Z-axis in this study.

Appendix A

MHD equilibrium calculation

A.1 Grad-Shafranov equation

The Grad-Shafranov equation is one kind of the MHD equilibrium equation for the tokamak plasmas. Since plasmas are assumed to be axisymmetric systems in this equation, the effects of the non-axisymmetric plasmas could not be taken into account.

Since the divergence of the magnetic field is zero and the gradient of the magnetic flux function Ψ is perpendicular to the magnetic field,

$$\begin{aligned} \nabla \cdot \boldsymbol{B} &= \frac{1}{R}\frac{\partial}{\partial R}(RB_R) + \frac{1}{R}\frac{\partial B_{\rm tor}}{\partial \phi} + \frac{\partial B_Z}{\partial Z} = 0 \\ \boldsymbol{B} \cdot \nabla \Psi &= B_R\frac{\partial \Psi}{\partial R} + B_{\rm tor}\frac{1}{R}\frac{\partial \Psi}{\partial \phi} + B_Z\frac{\partial \Psi}{\partial Z} = 0. \end{aligned}$$

If the plasmas can be assumed to be axisymmetric,

$$\begin{aligned} B_R &= -\frac{1}{R}\frac{\partial \Psi}{\partial Z} \\ B_Z &= \frac{1}{R}\frac{\partial \Psi}{\partial R}. \end{aligned} \tag{A.1}$$

Therefore, the magnetic field can be written as below,

$$\boldsymbol{B} = \frac{1}{R}\nabla\Psi \times \boldsymbol{e}_\phi + B_{\rm tor}\boldsymbol{e}_\phi. \tag{A.2}$$

Similarly, the divergence of the current density vector is zero and the gradient of the magnetic flux function I is perpendicular to the current vector. Therefore,

$$\begin{aligned} j_R &= -\frac{1}{R}\frac{\partial I}{\partial Z} \\ j_Z &= \frac{1}{R}\frac{\partial I}{\partial R} \\ \boldsymbol{j} &= \frac{1}{R}\nabla I \times \boldsymbol{e}_\phi + j_{\rm tor}\boldsymbol{e}_\phi. \end{aligned} \tag{A.3}$$

From the Ampere's law, the below condition can be derived,

$$RB_{\mathrm{tor}} = \mu_0 I \equiv F. \tag{A.4}$$

From the Ampere's law and the MHD equilibrium equation, the Grad-Shafranov equation can be derived as below,

$$R\frac{\partial}{\partial R}\left(\frac{1}{R}\frac{\partial \Psi}{\partial R}\right) + \frac{\partial^2 \Psi}{\partial Z^2} = -\frac{\mathrm{d}}{\mathrm{d}\Psi}\left(\frac{F^2}{2}\right) - R^2\mu_0\frac{\mathrm{d}p}{\mathrm{d}\Psi}. \tag{A.5}$$

A.2 VMEC code

The VMEC (Variational Moment Equilibrium Code) is an efficient computer code to calculate the 3D MHD equilibria using the inverse spectral method [10][11][33]. The total energy W_{pl} in the plasma region V_{pl} is written as,

$$W_{\mathrm{pl}} = \int_{V_{\mathrm{pl}}} \left(\frac{B^2}{2\mu_0} + \frac{P}{\gamma - 1}\right) \mathrm{d}V, \tag{A.6}$$

where P is the scalar plasma pressure. The total energy is minimized based on the variational principal. The magnetic field B is described by the Clebsch representation as,

$$\boldsymbol{B} = \nabla s \times \nabla \left(\acute{\psi}(s)\theta - \acute{\chi}(s)\zeta + \lambda\right), \tag{A.7}$$

where s is the label of the magnetic surface, $\acute{\psi}(s)$ and $\acute{\chi}(s)$ are respectively derivatives of the toroidal and poloidal flux function. θ, ζ are the poloidal and toroidal angle in the flux coordinates. It is noted that $\lambda(s, \theta, \zeta)$ is a stream function to determine the optimized poloidal angle as described later. In Eq. (A.6), the value B^2 is represented by the contravariant component of the magnetic field on the flux coordinates and W_{pl} is varied with respect to these variables. When the toroidal angel ζ is set to be same as the geometrical toroidal angle ϕ in the cylindrical coordinates (R, Z, ϕ) for simplicity, it is not necessary to vary W_{pl} with respect to ϕ. Here R is the major radius and Z is the hight from the midplane. Then, from Eq. (A.6), the variational form of W_{pl} can be obtained as,

$$\delta W_{\mathrm{pl}} = -\int_{V_{\mathrm{pl}}} \boldsymbol{F} \cdot \delta \boldsymbol{x} \mathrm{d}s\mathrm{d}\theta\mathrm{d}\zeta. \tag{A.8}$$

It should be noted that $\boldsymbol{x} = (R, \lambda, Z)$. From Eq. (A.8), it is obvious that the MHD equilibrium which satisfies $\delta W_{\mathrm{pl}} = 0$ is obtained when $\boldsymbol{F} = 0$. It can be shown that the condition $\boldsymbol{F} = 0$ is equivalent to the condition that the MHD residual force $\acute{\boldsymbol{F}} = -\boldsymbol{J} \times \boldsymbol{B} + \nabla P$ is exactly zero, when $\boldsymbol{J}$ is the current represented by $\boldsymbol{J} = \nabla \times \boldsymbol{B}$. Therefore, in the VMEC, the following numerical scheme is developed to find out the

solution $\boldsymbol{x}$ correspond to the equilibrium plasma configuration which satisfies $\boldsymbol{F} = 0$ instead of solving $\acute{\boldsymbol{F}} = 0$ directly.

In the VMEC, the shape of the flux surface (R, Z) and λ are the Fourier decomposed with respect to (θ, ζ) as follows:

$$\begin{aligned} R(s,\theta,\zeta) &= \sum_{\mathrm{mn}} R^{\mathrm{c}}_{\mathrm{mn}}(s)\cos(\mathrm{m}\theta - \mathrm{n}\zeta) + R^{\mathrm{s}}_{\mathrm{mn}}(s)\sin(\mathrm{m}\theta - \mathrm{n}\zeta) \\ Z(s,\theta,\zeta) &= \sum_{\mathrm{mn}} Z^{\mathrm{c}}_{\mathrm{mn}}(s)\cos(\mathrm{m}\theta - \mathrm{n}\zeta) + Z^{\mathrm{s}}_{\mathrm{mn}}(s)\sin(\mathrm{m}\theta - \mathrm{n}\zeta) \\ \lambda(s,\theta,\zeta) &= \sum_{\mathrm{mn}} \lambda^{\mathrm{c}}_{\mathrm{mn}}(s)\cos(\mathrm{m}\theta - \mathrm{n}\zeta) + \lambda^{\mathrm{s}}_{\mathrm{mn}}(s)\sin(\mathrm{m}\theta - \mathrm{n}\zeta) \end{aligned} \tag{A.9}$$

where $(R_{\mathrm{mn}}, Z_{\mathrm{mn}}, \lambda_{\mathrm{mn}})$ correspond to the moments of (R, Z, λ) that are defined on the discretized radial meshes. Using these Fourier representations, Eq. (A.8) can be written as,

$$\frac{\mathrm{d}W_{\mathrm{pl}}}{\mathrm{d}t} = \sum_{\mathrm{mn}} \int_{V_{\mathrm{pl}}} \boldsymbol{F}^{*}_{\mathrm{mn}} \cdot \frac{\partial \boldsymbol{x}_{\mathrm{mn}}}{\partial t} \mathrm{d}s\mathrm{d}\theta\mathrm{d}\zeta, \tag{A.10}$$

where t is the artificial time and $\boldsymbol{F}^{*}_{\mathrm{mn}}$ is complex conjugate of $\boldsymbol{F}_{\mathrm{mn}}$. In the 3D configurations, the large number of the moment amplitudes are needed to describe an equilibrium with sufficient numerical accuracy. Therefore, an iteration method is developed to follow the path along with $\mathrm{d}W_{\mathrm{pl}}/\mathrm{d}t$ which decreases a maximum rate (i.e., the steepest-descent method) [34]. The descent path equation for Eq. (A.10) is

$$\frac{\partial \boldsymbol{x}_{\mathrm{mn}}}{\partial t} = \boldsymbol{F}_{\mathrm{mn}} \tag{A.11}$$

and the maximum decreasing rate of W_{pl} along this path is given by

$$\frac{\mathrm{d}W_{\mathrm{pl}}}{\mathrm{d}t} = \sum_{\mathrm{mn}} \int_{V_{\mathrm{pl}}} |\boldsymbol{F}_{\mathrm{mn}}|^2 \, \mathrm{d}s\mathrm{d}\theta\mathrm{d}\zeta. \tag{A.12}$$

From Eq. (A.12), it is clear that the total energy W_{pl} is decreased monotonously according to the solution $\boldsymbol{x}_{\mathrm{mn}}$ of Eq. (A.11). Since the first order differential equation (A.11) is not easy to solve numerically, the second order equation;

$$\frac{\partial^2 \boldsymbol{x}_{\mathrm{mn}}}{\partial t^2} + \frac{1}{\tau}\frac{\partial \boldsymbol{x}_{\mathrm{mn}}}{\partial t} = \boldsymbol{F}_{\mathrm{mn}} \tag{A.13}$$

is solved instead of Eq. (A.11) in the VMEC code, which is called the second order Richardson scheme. The parameter $\tau > 0$ has little effect on the stability of the least-damped mode of Eq. (A.13), minimizing the number of iterations required to reach steady state.

A.3 HINT code

The HINT code is a 3D MHD equilibrium calculation code based on the time-dependent relaxation method in the Cartesian coordinates [33]. In these coordinates, the calculation is performed as follows.

The first step (step-A) is a relaxation process to satisfy the condition $\boldsymbol{B} \cdot \nabla p = 0$. Since this condition is equivalent to no pressure variation along the magnetic field lines, this process calculates the averaged pressure along the field line that passes through a grid point;

$$p \sim \bar{p} = \frac{\int pB^{-1}\mathrm{d}l}{\int B^{-1}\mathrm{d}l}, \tag{A.14}$$

and uses this update the pressure on that grid point. If some field line reaches to the computational boundary, the pressure sets to $p = 0$ on the grid point. The averaged plasma pressure $\bar{p}$ is calculated on all grid points.

The next step (step-B) is a relaxation of the magnetic field with the plasma pressure distribution fixed. The process solves the time evolution of the dissipative equations;

$$\frac{\partial}{\partial t}(\rho \boldsymbol{v}) = -f_{\mathrm{c}}\left[\nabla p - (\boldsymbol{j} - \boldsymbol{j_0}) \times \boldsymbol{B}\right] \tag{A.15}$$

$$\frac{\partial \boldsymbol{B}}{\partial t} = \nabla \times [\boldsymbol{v} \times \boldsymbol{B} - \eta(\boldsymbol{j} - \boldsymbol{j_0} - \boldsymbol{j_{\mathrm{net}}})] \tag{A.16}$$

$$\boldsymbol{j} - \boldsymbol{j}_0 = \frac{1}{\mu_0}\nabla \times (\boldsymbol{B} - \boldsymbol{B}_0) \tag{A.17}$$

where $\boldsymbol{B_0}$ is the vacuum magnetic field and $\boldsymbol{j_{\mathrm{net}}}$ is the net current (e.g., the Ohmic and the neoclassical current) [35][36]. The dissipative parameter η is assumed to be constant. The factor f_{c},

$$f_{\mathrm{c}} = \begin{cases} 1 & (B \le B_{\mathrm{c}}) \\ (B_{\mathrm{c}}/B)^2) & (B > B_{\mathrm{c}}) \end{cases} \tag{A.18}$$

is calculated on all grid points, where B is the magnetic field strength and B_{c} is specified to between the maximum and the minimum value of the magnetic field in the poloidal plane.

With these steps, the equilibrium state is finally determined through iteration until the prescribed net current condition is satisfied.

Appendix B

Development of the calculation tool

B.1 Determination of the external coil currents

There are two situations exist in the VMEC: a fixed boundary and a free boundary conditions. Because the last flux surface is given by the input parameter for the fixed boundary conditions, the vacuum field is not necessary. Whereas for the free boundary conditions, the last flux surface is controlled by the total toroidal magnetic flux. Therefore, each coil current is needed to calculate the MHD equilibria using the VMEC for any pressure profile, the safety-factor profile and the last flux surfaces. This section explains about the methods to determine the external coil currents which are necessary for the free boundary calculation in the VMEC.

Firstly, the fixed boundary calculation is performed for the given pressure profile, the safety-factor profile and the last flux surface. An example of the calculation model is shown in Fig. B.1. With the VMEC results, the equilibrium field $\boldsymbol{B}$ is obtained on the plasma boundary ($\boldsymbol{r}$). Using the magnetic field calculation method which was introduced in Section 5.2.2, the magnetic field component $\boldsymbol{B}^{\mathrm{pl}}(\boldsymbol{r})$ is also obtained on the plasma boundary. Therefore, the vacuum field $\boldsymbol{B}^{\mathrm{ext}}(\boldsymbol{r})$ to keep the MHD equilibria for the given input parameters are written as below,

$$\boldsymbol{B}^{\mathrm{ext}}(\boldsymbol{r}) = \boldsymbol{B}(\boldsymbol{r}) - \boldsymbol{B}^{\mathrm{pl}}(\boldsymbol{r}). \tag{B.1}$$

By the current density of each external coil $\boldsymbol{j}_{\mathbf{c}}^{\mathrm{k}}(\boldsymbol{r}')$, the current flows on the cross-section S_{k},

$$\hat{J}_{\mathrm{c}}^{\mathrm{k}} = \mu_0 \iint_{C_{\mathrm{k}}} \frac{\boldsymbol{j}_{\mathbf{c}}^{\mathrm{k}}(\boldsymbol{r}_{\mathrm{k}}') \times (\boldsymbol{r} - \boldsymbol{r}_{\mathrm{k}}')}{4\pi|\boldsymbol{r} - \boldsymbol{r}_{\mathrm{k}}'|^3} \mathrm{d}S_{\mathrm{k}}. \tag{B.2}$$

If 1[A] flows on the cross-section of a external coil, the magnetic field component is produces as,

$$\boldsymbol{B}_{\mathrm{c}}^{\mathrm{k}}(\boldsymbol{r}) = \frac{\mu_0}{\hat{J}_{\mathrm{c}}^{\mathrm{k}}} \iiint_{C_{\mathrm{k}}} \frac{\boldsymbol{j}_{\mathbf{c}}^{\mathrm{k}}(\boldsymbol{r}_{\mathrm{k}}') \times (\boldsymbol{r} - \boldsymbol{r}_{\mathrm{k}}')}{4\pi|\boldsymbol{r} - \boldsymbol{r}_{\mathrm{k}}'|^3} \mathrm{d}V_{\mathrm{k}}. \tag{B.3}$$

Therefore, equation (B.1) can be written as,

$$\sum_{\mathrm{k}=1}^{N} J_{\mathrm{c}}^{\mathrm{k}} \boldsymbol{B}_{\mathrm{c}}^{\mathrm{k}}(\boldsymbol{r}) = \boldsymbol{B}(\boldsymbol{r}) - \boldsymbol{B}^{\mathrm{pl}}(\boldsymbol{r}) \tag{B.4}$$

where N is the number of the external coils.

Secondly, the plasma boundary is divided in n and the position vector is defined as $\boldsymbol{r}_{\mathrm{l}}$ ($\mathrm{l} = 1, 2, 3, ..., n$). The square error of equation (B.4) on $\boldsymbol{r}_{\mathrm{l}}$ is written as,

$$\begin{aligned} a^{\mathrm{l}} &= \left(\boldsymbol{B}(\boldsymbol{r}_{\mathrm{l}}) - \boldsymbol{B}^{\mathrm{pl}}(\boldsymbol{r}_{\mathrm{l}}) - \sum_{\mathrm{k}=1}^{N} J_{\mathrm{c}}^{\mathrm{k}} \boldsymbol{B}_{\mathrm{c}}^{\mathrm{k}}(\boldsymbol{r}_{\mathrm{l}}) \right)^2 \\ &= \left(\boldsymbol{B}^{\mathrm{ext}}(\boldsymbol{r}_{\mathrm{l}}) - \sum_{\mathrm{k}=1}^{N} J_{\mathrm{c}}^{\mathrm{k}} \boldsymbol{B}_{\mathrm{c}}^{\mathrm{k}}(\boldsymbol{r}_{\mathrm{l}}) \right)^2 . \end{aligned} \tag{B.5}$$

The summation of a^{l} can be written as,

$$A = \sum_{\mathrm{l}=1}^{n} a^{\mathrm{l}} = \sum_{\mathrm{l}=1}^{n} \left(\boldsymbol{B}^{\mathrm{ext}}(\boldsymbol{r}_{\mathrm{l}}) - \sum_{\mathrm{k}=1}^{N} J_{\mathrm{c}}^{\mathrm{k}} \boldsymbol{B}_{\mathrm{c}}^{\mathrm{k}}(\boldsymbol{r}_{\mathrm{l}}) \right)^2 . \tag{B.6}$$

To minimize A, the partial differentiation of A for $J_{\mathrm{c}}^{\mathrm{k}}$ should be zero,

$$\begin{aligned} \frac{\partial A}{\partial J_{\mathrm{c}}^{\mathrm{k}}} &= -2 \sum_{\mathrm{l}=1}^{n} \boldsymbol{B}_{\mathrm{c}}^{\mathrm{k}}(\boldsymbol{r}_{\mathrm{l}}) \left(\boldsymbol{B}^{\mathrm{ext}}(\boldsymbol{r}_{\mathrm{l}}) - \sum_{\mathrm{i}=1}^{N} J_{\mathrm{c}}^{\mathrm{i}} \boldsymbol{B}_{\mathrm{c}}^{\mathrm{i}}(\boldsymbol{r}_{\mathrm{l}}) \right) = 0 \\ \therefore \quad \sum_{\mathrm{i}=1}^{N} J_{\mathrm{c}}^{\mathrm{i}} \sum_{\mathrm{l}=1}^{n} \boldsymbol{B}_{\mathrm{c}}^{\mathrm{k}}(\boldsymbol{r}_{\mathrm{l}}) \boldsymbol{B}_{\mathrm{c}}^{\mathrm{i}}(\boldsymbol{r}_{\mathrm{l}}) &= \sum_{\mathrm{l}=1}^{n} \boldsymbol{B}_{\mathrm{c}}^{\mathrm{k}}(\boldsymbol{r}_{\mathrm{l}}) \boldsymbol{B}^{\mathrm{ext}}(\boldsymbol{r}_{\mathrm{l}}) \end{aligned} \tag{B.7}$$

If the equation (B.7) is described as the matrix,

$$\begin{aligned} G_{\mathrm{ki}} x_{\mathrm{i}} &= H_{\mathrm{k}} \\ \therefore \quad x_{\mathrm{i}} &= G_{\mathrm{ki}}^{-1} H_{\mathrm{k}}. \end{aligned} \tag{B.8}$$

Where,

$$
\begin{aligned}
x_{\mathrm{i}} = \boldsymbol{x} &= \begin{bmatrix} J_{\mathrm{c}}^{1} \\ J_{\mathrm{c}}^{2} \\ \vdots \\ J_{\mathrm{c}}^{N} \end{bmatrix} \\
G_{\mathrm{ki}} = \boldsymbol{G} &= \begin{bmatrix} \sum \boldsymbol{B}_{\mathrm{c}}^{1}(\boldsymbol{r}_{\mathrm{l}})\boldsymbol{B}_{\mathrm{c}}^{1}(\boldsymbol{r}_{\mathrm{l}}) & \sum \boldsymbol{B}_{\mathrm{c}}^{1}(\boldsymbol{r}_{\mathrm{l}})\boldsymbol{B}_{\mathrm{c}}^{2}(\boldsymbol{r}_{\mathrm{l}}) & \cdots & \sum \boldsymbol{B}_{\mathrm{c}}^{1}(\boldsymbol{r}_{\mathrm{l}})\boldsymbol{B}_{\mathrm{c}}^{N}(\boldsymbol{r}_{\mathrm{l}}) \\ \sum \boldsymbol{B}_{\mathrm{c}}^{2}(\boldsymbol{r}_{\mathrm{l}})\boldsymbol{B}_{\mathrm{c}}^{1}(\boldsymbol{r}_{\mathrm{l}}) & \sum \boldsymbol{B}_{\mathrm{c}}^{2}(\boldsymbol{r}_{\mathrm{l}})\boldsymbol{B}_{\mathrm{c}}^{2}(\boldsymbol{r}_{\mathrm{l}}) & \cdots & \sum \boldsymbol{B}_{\mathrm{c}}^{2}(\boldsymbol{r}_{\mathrm{l}})\boldsymbol{B}_{\mathrm{c}}^{N}(\boldsymbol{r}_{\mathrm{l}}) \\ \vdots & & \vdots & \\ \sum \boldsymbol{B}_{\mathrm{c}}^{N}(\boldsymbol{r}_{\mathrm{l}})\boldsymbol{B}_{\mathrm{c}}^{1}(\boldsymbol{r}_{\mathrm{l}}) & \sum \boldsymbol{B}_{\mathrm{c}}^{N}(\boldsymbol{r}_{\mathrm{l}})\boldsymbol{B}_{\mathrm{c}}^{2}(\boldsymbol{r}_{\mathrm{l}}) & \cdots & \sum \boldsymbol{B}_{\mathrm{c}}^{N}(\boldsymbol{r}_{\mathrm{l}})\boldsymbol{B}_{\mathrm{c}}^{N}(\boldsymbol{r}_{\mathrm{l}}) \end{bmatrix} \\
H_{\mathrm{k}} = \boldsymbol{H} &= \begin{bmatrix} \sum \boldsymbol{B}_{\mathrm{c}}^{1}(\boldsymbol{r}_{\mathrm{l}})\boldsymbol{B}^{\mathbf{ext}}(\boldsymbol{r}_{\mathrm{l}}) \\ \sum \boldsymbol{B}_{\mathrm{c}}^{2}(\boldsymbol{r}_{\mathrm{l}})\boldsymbol{B}^{\mathbf{ext}}(\boldsymbol{r}_{\mathrm{l}}) \\ \vdots \\ \sum \boldsymbol{B}_{\mathrm{c}}^{N}(\boldsymbol{r}_{\mathrm{l}})\boldsymbol{B}^{\mathbf{ext}}(\boldsymbol{r}_{\mathrm{l}}) \end{bmatrix}.
\end{aligned}
$$

By solving equation (B.8), the external coil currents can be obtained for the free boundary calculation in the VMEC.

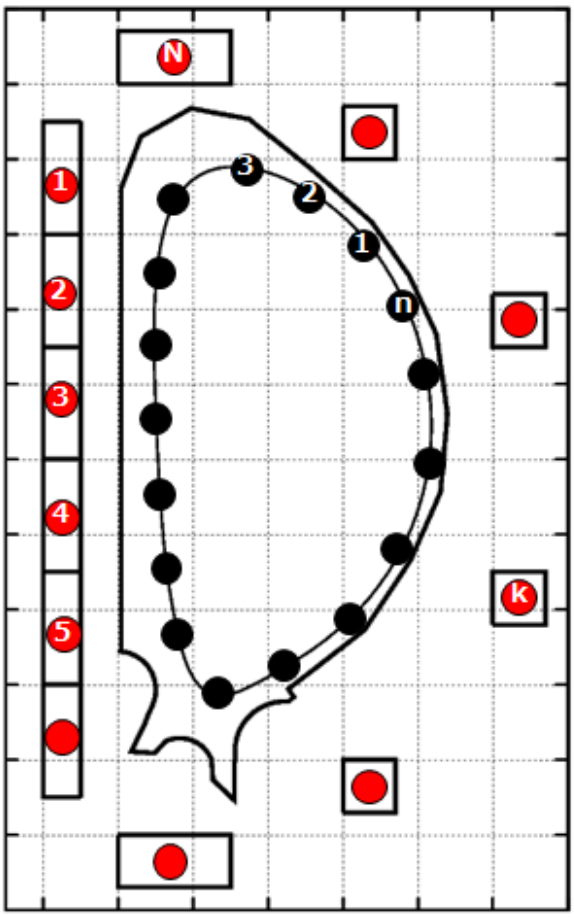

Figure B.1: An example of calculation model. The number of the external poloidal coils is N and the plasma boundary is divided in n.

Appendix C

Diamagnetic effect on the ripple induced losses of energetic ion in a non-axisymmetric tokamak plasma

In a tokamak plasma, the energetic ion losses are increased by the TF ripples, which are created by the finite number of the TFCs. The equilibrium plasma current alters the magnetic field structures and the energetic ion losses. The diamagnetic effect generated by the poloidal plasma current is one of the most important finite beta effects. It produces two kinds of effects on the energetic ion losses: 1) the reduction of the energetic ion losses due to the closed $|B|$ contour and 2) increase of these losses due to the $|B|$ contour line bending effect. These effects on the energetic ion losses should be evaluated using the MHD equilibrium calculation code VMEC and the orbit calculation code F3D-OFMC. In the result, it is found that the diamagnetic effect usually increases the energetic ion losses, while the quite strong diamagnetic effect reduces them. This paper was published in Zero-Carbon Energy Kyoto 2012 [37].

C.1 Introduction

The finite number of the TFCs breaks the symmetry of the tokamak plasma. Due to the TF ripples, the energetic ion losses are increased in a tokamak plasma. Especially, the fusion alpha particle losses induce several serious issues such as the deterioration of the plasma heating efficiency and the localized heat loads on the first wall. To confine the energetic ions successfully, the magnetic field structures have to be investigated. The plasma itself alters the magnetic field structures and the energetic ion losses. Especially the diamagnetic current significantly alters the $|B|$ contour curvature in a high-beta plasma [9]. The diamagnetic effect produces two kinds of effects on the energetic ion losses: 1) the reduction of the energetic ion losses due to the closed $|B|$ contour and 2) increase of these losses due to the $|B|$ contour line bending effect. In this study, the toroidal field generated

by the plasma current is obtained using the VMEC. In order to analyze the diamagnetic effect on the energetic ion losses, five cases of the 3D field structures are created by artificially changing the toroidal field component from the poloidal plasma current. The diamagnetic effect on the energetic ion losses is quantitatively evaluated by calculating the alpha particles orbits.

C.2 MHD equilibrium calculation

In this study, the calculation model is referred by the 9MA scenario of an ITER operation. The volume-averaged beta value is set to 2% which is same as the original ITER operation [8][13]. The reversed sher safety-factor profile is used as Fig. C.1(b). The 2D MHD equilibrium field is calculated using the VMEC code [10][11]. By superimposing the vacuum ripple component on the 2D MHD equilibrium field, the approximated 3D field structure can be created in this study.

Figure C.2(a) shows the vacuum and equilibrium toroidal field $B_{\rm tor}$ along the R direction. The vacuum toroidal field is approximately proportional to $1/R$. Therefore, the vacuum toroidal field has not same value along the R direction. Because of the diamagnetic effect, the vacuum toroidal field is reduced at the outer torus and the $|B|$ contour curvature becomes higher. To analyze the diamagnetic effect on the energetic ion losses, five cases of the 3D field structures are artificially created by changing the toroidal field component from the poloidal plasma current. In this study, each field case is called J0, J1, J2, J3 and J4, in which the diamagnetic effect on the toroidal field is artificially multiplied by the weight factor 0, 1, 2, 3 and 4, respectively. Figure C.3(b) shows the field strength $|B|$ along the R direction at $(Z, \phi) = (0.5\text{m}, 0)$ for each field case. By changing the diamagnetic effect, the field strength is reduced at outer torus and the $|B|$ contour is also changed. Figures C.3 show the $|B|$ contour line at $\phi = 0$ for each field model. As mentioned above, the $|B|$ contour line becomes higher and the closed contour region is extended with increasing the diamagnetic effect. In the next section, how the changes of $|B|$ contour affect on the energetic ion losses is clarified.

C.3 Diamagnetic effects on the energetic ion losses

The red color in Figures C.4 shows the tracing time of the alpha particles on the initial point. They are started from the inner plasma with the pitch angle $\lambda = 0.5$. These figures clearly show that there are two opposing effects due to the diamagnetic effect.

The black dots in Fig. C.4 show the first trapped points of 10,000 fusion alpha particles, where the untrapped particles are ignored. For these birth profiles, the energetic ion orbits are calculated using the F3D-OFMC code [27]. Figure C.5 shows the loss power fraction ϵ. The final ϵ for J0, J1, J2, J3 and J4 models are 0.050, 0.086, 0.101, 0.104 and 0.089, respectively. The diamagnetic effect usually increases the energetic ion losses,

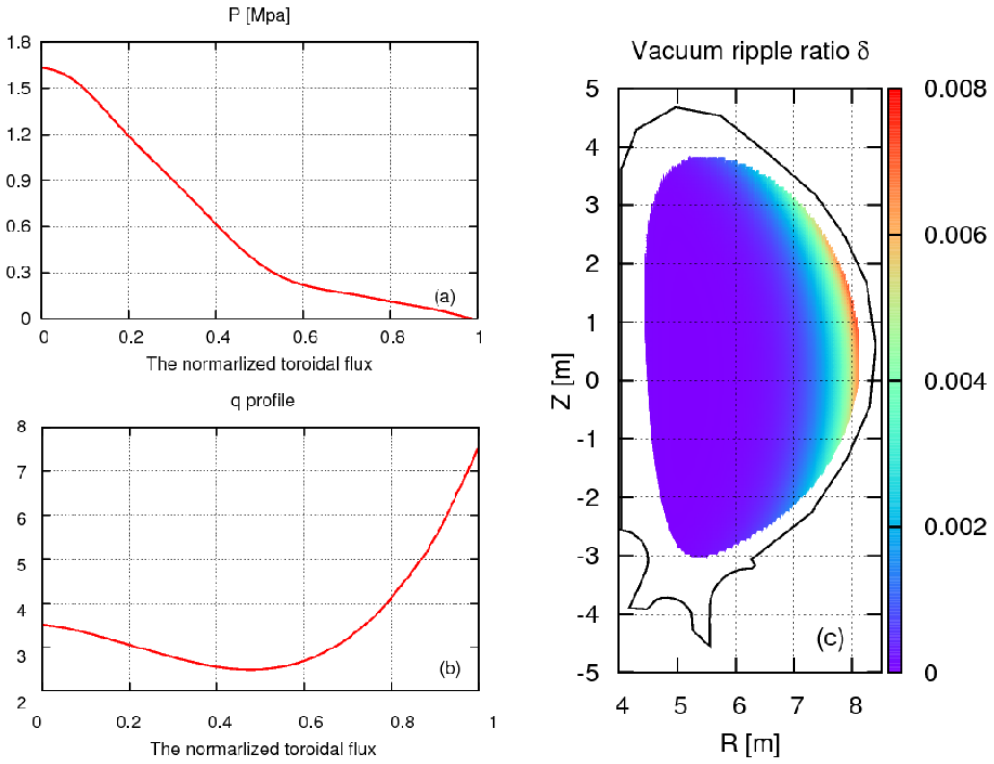

Figure C.1: (a) The pressure profile, (b) the safety-factor profile and (c) the vacuum ripple ratio

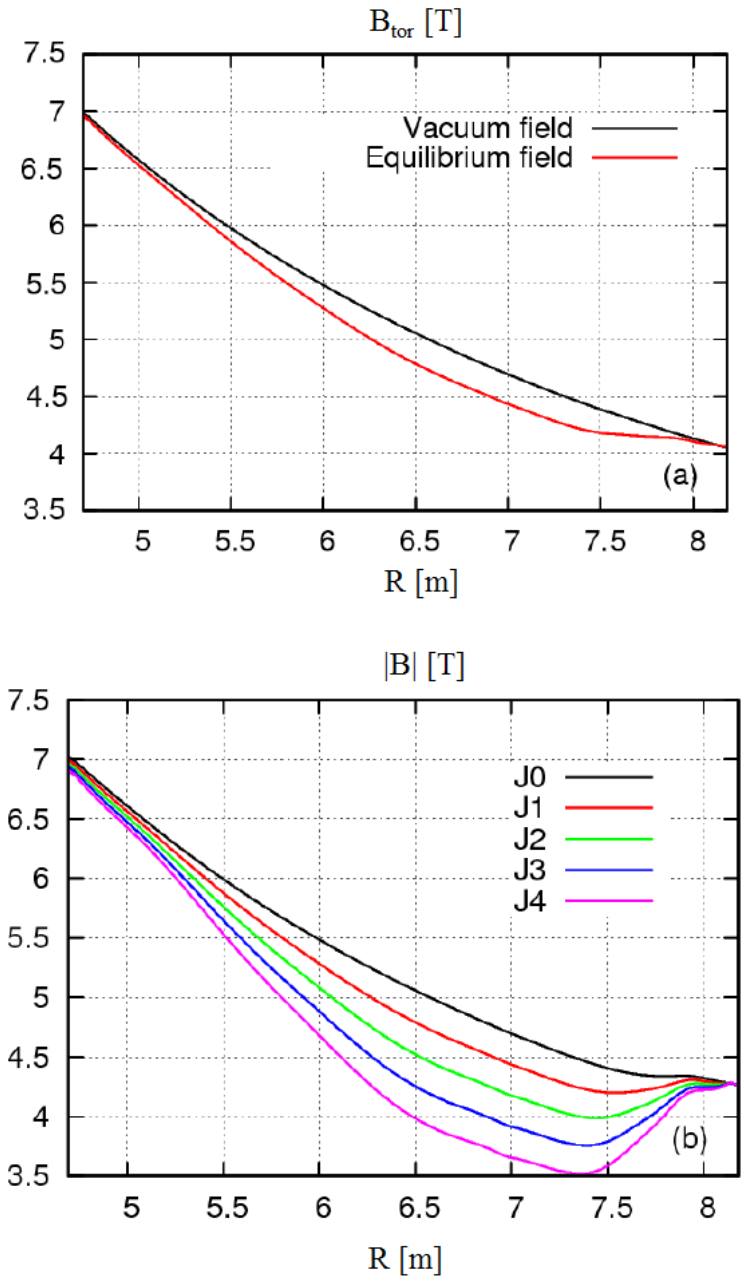

Figure C.2: (a) The vacuum and equilibrium toroidal field strength and (b) the field strength $|B|$ for each field model along the R direction at $(Z, \phi) = (0.5\text{m}, 0)$

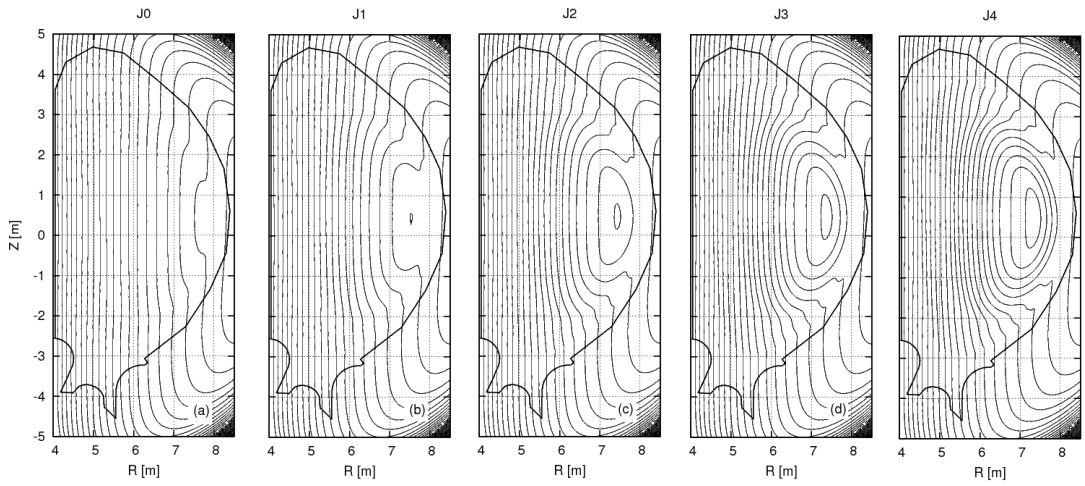

Figure C.3: The contour of the field strength $|B|$ at $\phi = 0$ for each field model

while the quite strong diamagnetic effect reduces them. It suggests that there are good conditions to confine the energetic ions by the strong diamagnetic effect, such as the high pressure, the high aspect ratio and the high safety-factor.

C.4 Summary

In this study, the diamagnetic effect on the fusion alpha particle losses is investigated using the VMEC code and the F3D-OFMC code. By artificially multiplying the toroidal field component from the poloidal plasma current by weight factor 0, 1, 2, 3 and 4, five cases of the 3D field structures are created. With increasing the weight factor, the $|B|$ contour curvature becomes higher at the outer torus. For fusion alpha particles, the diamagnetic effect usually increases the energetic ion losses, while the quite strong diamagnetic effect reduces them. In a future work, the diamagnetic effect on the energetic ion losses should be evaluated by changing the aspect ratio and the safety factor.

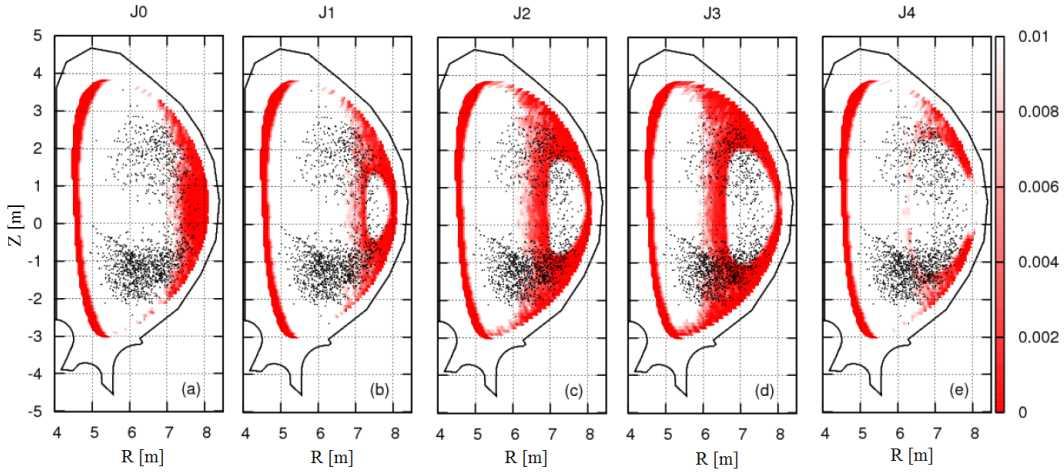

Figure C.4: The tracing time [s] for the alpha particles with the pitch angle $\lambda = 0.5$ on the initial point (the red color) and the first trapped points of the 10,000 fusion alpha particles (the black dots)

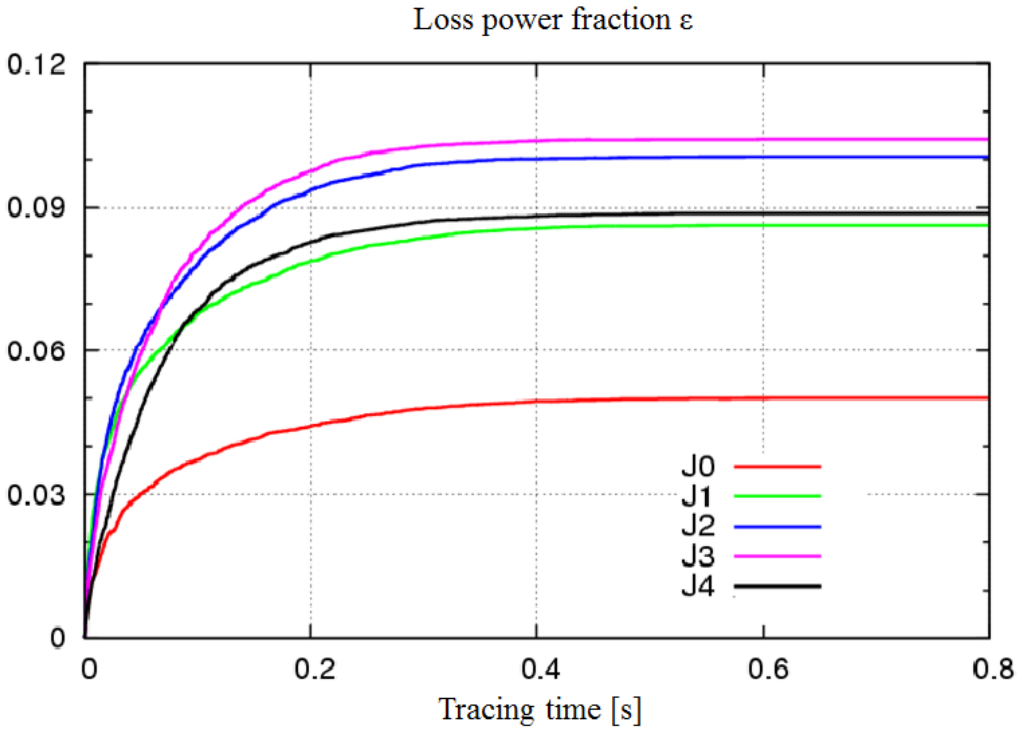

Figure C.5: The tracing time dependence of the loss power fraction ϵ for each field model, J0, J1, J2, J3 and J4

References

[1] 松田 慎三郎, 電気学会誌, 128 (2008) 2 74-77

[2] 高速イオン及びアルファ粒子の物理研究調査報告書, 社団法人 プラズマ・核融合学会 (1991).

[3] Goldstone R.J., White R.B. and Boozer A.H. Phys. Rev. Lett. 47 (1981) 647

[4] K. Tani et. al., J. Phys. Soc. Jpn. 50 (1981) 1726

[5] K. Tobita et. al., Nucl. Fusion 37 (1994) 1097

[6] K.Shinohara et al. Fusion Engineering and Design 84 (2009) 24

[7] 佐藤 正泰 et. al., プラズマ核融合学会誌 74 (1998) 448

[8] E.Strumberger, S.Gunter, P.Merkel, E.Schwarz and C.Tichmann, Nucl. Fusion 50 (2010) 025008.

[9] Y.Suzuki, Y.Nakamura and K.Kondo, Nucl. Fusion 43 (2003) 406415.

[10] S.P.Hirshman and H.K.Meier Phys. Fluids 28 (1985) 1387.

[11] S.P.Hirshman, W.I.van Rij and P.Merkel, Comput. Phys. Comm. 43 (1986) 143.

[12] J.M. Greene and M.S. Chance, Nucl. Fusion 21 (1981) 453

[13] K.Shinohara, T.Kurki-Suonio, D.Spong, et.al., Nucl. Fusion 51 (2011) 063028.

[14] Y.Nakamura, Fundamental Energy Science II

[15] Gioietta Kuo-Petravic, A.H.Boozer, J.A.Rome and R.H.Fowler, J.comp.Phys. vol.51 (1983) 261.

[16] Allen H.Boozer, Phys.Fluids vol.23 (1980) 904.

[17] D. R. Mikkelsen, R. B. White, R. J. Akers, S. M. Kaye, D. C. McCune, and J. E. Menard, Phys. Plasmas 4, 3667 (1997).

[18] M.Yokoyama, Y.Nakamura et al. Nucl. Fusion 40 (2000) 261

[19] Y.Nakamura et al. AIP Conf. Proc. 311 (1994) 114123

[20] M.Bunno et al. Nucl. Fusion 52 (2012) 083009

[21] K.Tani et al. Nucl. Fusion 33 (1993) 903

[22] S.J. Zweben et al Nucl. Fusion 35 (1995) 1445

[23] R.H.Fowler, J.A.Rome and J.F.Lyon, Phys. Fluids 28 (1981) 338

[24] H.Urano et al. Nucl. Fusion 47 (2007) 706

[25] O.A.Anderson and H.P.Furth, Nucl. Fusion 12 207 (1972)

[26] K.Tobita et al. J. Plasma Fusion Res. 75 582 (1999)

[27] K.Tani, M.Azumi, H.Kishimito and S.Tamura, J. Phys. Soc. Japan. 50 (1981) 1726

[28] M. Bunno, Y. Nakamura, Y. Suzuki, K. Shinohara, G. Matsunaga and K. Tani, Plasma Sci. and Technol. 15 115 (2013).

[29] D.A.Spong, Physics of Plasmas 18 (2011) 056109.

[30] S.E.Attenberger, w.A.Houlberg and S.P.Hirshman, Tech. Rep. ORNL/TM-10412 (1987)

[31] M. Bunno et.al., Physics of Plasmas 20 (2013) 082511

[32] J. W. Connor, R. J. Hastie and T. J. Martin, Nucl. Fusion 23 170 (1983).

[33] Y.Suzuki, Kyoto University, Doctor thesis (2003)

[34] H.Grad Phys. Fluids 7 (1964) 1283

[35] R.Kanno et.al., J. Plasma Phys. 61 (1999) 213

[36] R.Kanno et.al., J. Plasma Fusion Res. SERIES 2 (1999) 291

[37] M. Bunno, Zero-Carbon Energy Kyoto 2012, Green Energy and Technology 217-222 (2013).

Achievements

Referred papers

1. M. Bunno, Y. Nakamura, Y. Suzuki, K. Shinohara, and G. Matsunaga, "Finite beta effects on MHD equilibria and energetic ion losses in a rippled tokamak," Nucl. Fusion 52 083009 (2012).

2. M. Bunno, Y. Nakamura, Y. Suzuki, K. Shinohara, G. Matsunaga and K. Tani, "The Finite Beta Effects on the Toroidal Field Ripple in a Tokamak Plasma," Plasma Sci. and Technol. 15 115 (2013).

3. M. Bunno, Y. Nakamura, Y. Suzuki, K. Shinohara, G. Matsunaga, and K. Tani, "Fusion alpha-particle losses in a high-beta rippled tokamak," Physics of Plasmas 20 082511 (2013).

4. M. Bunno, "Diamagnetic Effect on the Ripple-Induced Losses of Energetic Ions in a Non-Axisymmetric Tokamak Plasma," Zero-Carbon Energy Kyoto 2012, Green Energy and Technology 217-222 (2013).

International conferences

1. M. Bunno, Y. Nakamura, Y. Suzuki, K. Shinohara, and G. Matsunaga, "Three-dimensional MHD equilibria of ITER plasma," 20th International Toki Conference, Gifu, Japan, 08.12.2010

2. M. Bunno, Y. Nakamura, Y. Suzuki, K. Shinohara, and G. Matsunaga, "The finite beta and nonaxisymmetric effect on the ripple trapped particle in the ripple tokamak plasma," Zero-Carbon Energy 2011, Korea, 19.08.2011

3. M. Bunno, Y. Nakamura, Y. Suzuki, K. Shinohara, and G. Matsunaga, "Beta value dependence on the ripple induced losses and the heat loads," APFA 2011, China, 02.11.2011

4. M. Bunno, Y. Nakamura, Y. Suzuki, K. Shinohara, and G. Matsunaga, "Finite beta effects on alpha particle heat loads in high-beta ripple tokamak plasmas," Plasma Conference 2011, Ishikawa, Japan, 23.11.2011

5. M. Bunno, Y. Nakamura, Y. Suzuki, K. Shinohara, and G. Matsunaga, "Finite beta effects on alpha particle losses in a high beta ripple tokamak," NIFS Scientific Workshop Physics issues on energetic particle confinement in toroidal plasmas, 08.12.2011

6. M. Bunno, Y. Nakamura, Y. Suzuki, K. Shinohara, and G. Matsunaga, "Finite beta effects on the energetic ion losses in a high beta ripple tokamak," Joint ITPA/US-Japan workshop, Gifu, Japan, 06.03.2012

7. M. Bunno, Y. Nakamura, Y. Suzuki, K. Shinohara, and G. Matsunaga, "Diamagnetic effect on the ripple induced losses of energetic ion in a non-axisymmetric tokamak plasma," Zero-Carbon Energy 2012, Thailand, 22.05.2012

8. M. Bunno, Y. Nakamura, Y. Suzuki, K. Shinohara, and G. Matsunaga, "Diamagnetic effect on the energetic ion losses in a ripple tokamak," 39th EPS Conference and 16th Int. Congress on Plasma Physics, Sweden, 02.07.2012

9. M. Bunno, Y. Nakamura, Y. Suzuki, K. Shinohara, G. Matsunaga, and K. Tani, "Safety-factor profile dependence of the diamagnetic effect on fusion alpha particle losses in a rippled tokamak," 54th Annual Meeting of the APS Division of Plasma Physics, 29.10.2012

10. M. Bunno, Y. Nakamura, and Y. Suzuki, "Non-axisymmetric perturbations for bifurcated magnetohydrodynamic equilibria in Tokamak," The 12th Asia Pacific Physics Conference and the third Asia-Europe Physics Summit, 14.07.2013

National conferences

1. 文野通尚、中村祐司、鈴木康浩、篠原孝司、松永剛、 “非軸対称トカマクの 3 次元平衡計算”、第 27 回プラズマ・核融合学会年会、北海道大学、2010 年 12 月 2 日

2. 文野通尚、中村祐司、鈴木康浩、篠原孝司、松永剛、 “ITER での 3 次元 MHD 平衡計算と α 粒子の軌道に与える有限ベータ効果”、第 66 回物理学会年会、新潟大学、2011 年 3 月 25 日

3. 文野通尚、中村祐司、鈴木康浩、篠原孝司、松永剛 谷啓二、 “リップル軌道損失に対する有限ベータ効果の定量的評価”、第 67 回物理学会年会、関西学院大学、2012 年 3 月 25 日

4. 文野通尚、中村祐司、鈴木康浩、篠原孝司、松永剛 谷啓二、 “高 β リップルトカマクにおける α 粒子のエネルギー損失に関する研究”、第 29 回プラズマ・核融合学会年会、福岡県春日市、2012 年 11 月 27 日

5. 文野通尚、中村祐司、鈴木康浩、篠原孝司、松永剛 谷啓二、 “高ベータリップルトカマクにおける α 粒子損失”、マルチスケール MHD 現象の理論・シミュレーション研究会、NIFS、2012 年 12 月 13 日

6. 文野通尚、中村祐司、鈴木康浩、 “トカマクの分岐平衡における非軸対称磁場構造に関する研究”、第 30 回プラズマ・核融合学会年会、東京工業大学、2013 年 12 月 3 日

Acknowledgment

First, I would like to thank Professor Yuji Nakamura. He is my supervisor and I always consulted and discussed with him. He gave me sound advices when I was at a loss. I also thanks to Assistant Professor Yasuhiro Suzuki at National Institute for Fusion Science (NIFS). Since there is no assistant professor in our laboratory, he is like my second boss. I met him in the international conference for several times and he treat me something good to eat.

I am also deeply grateful to my collaborator, Dr. Koji Shinohara, Dr. Go Matsunaga at Japan Atomic Energy Agency (JAEA), and Dr. Keiji Tani at Nippon Advanced Technology (NAT). Dr. Shinohara is specialist for the energetic ion losses and he always gave me a lot of advices and checked my paper as soon as possible. Dr. Matsunaga arranged the opportunities of the research presentation and helped me for the procedures of the business trips.

I also thank S.P. Hirshman and D.A. Spong for providing the VMEC code and the equilibrium data. Thanks for VMEC, I could get results and take a degree.

Finaly, I wish to express my gratitude to all members of the Laboratory for Complex Energy Process and Department of Fundamental Energy Science, Graduate School of Energy Science, Kyoto University.